NATIONAL AERONAUTICS AND SPACE ADMINISTRATION

Technical Report 32-1579

Solar Electric Propulsion Thrust Subsystem Development

T. D. Masek

CASE FILE COPY

JET PROPULSION LABORATORY
CALIFORNIA INSTITUTE OF TECHNOLOGY
PASADENA, CALIFORNIA

March 15, 1973

NATIONAL AERONAUTICS AND SPACE ADMINISTRATION

Technical Report 32-1579

Solar Electric Propulsion Thrust Subsystem Development

T. D. Masek

JET PROPULSION LABORATORY
CALIFORNIA INSTITUTE OF TECHNOLOGY
PASADENA, CALIFORNIA

March 15, 1973

Preface

The work described in this report was performed by the Propulsion Division of the Jet Propulsion Laboratory.

Acknowledgment

Contents

Contents (contd)

Contents (contd)

Tables

Figures

Contents (contd)

Figures (contd)

Contents (contd)

Figures (contd)

Contents (contd)

Tables (contd)

Abstract

This report presents the results of the third phase of the JPL Solar Electric Propulsion System Technology (SEPST III) Program. This phase of the program included about three years of preparation and testing. Of this time, approximately six months were spent in testing a complete automated thrust subsystem.

The system developed under this program was designed to demonstrate all the thrust subsystem functions anticipated to be needed on an unmanned planetary vehicle. The demonstration included operation of the basic elements, power matching, input and output voltage regulation, three-axis thrust vector control (TVC), subsystem automatic control including failure detection and correction capability (using a PDP-11 computer), operation of critical elements in thermal-vacuum-, zero-gravity-type propellant storage, and data outputs from all subsystem elements. The subsystem elements, functions, unique features, and test setup are described. General features and capabilities of the test-support data system are also presented.

The test program culminated in a 1500-h, computer-controlled, system-functional demonstration. This included simultaneous operation of two thruster/power conditioner sets. The results of this testing phase satisfied all the program goals. In particular, the subsystem performed all the expected functions, subsystem efficiency appears to be compatible with vehicle requirements, projected specific mass is about 17 kg/kW of input power, and the major TSS integration problems are understood. This work provides a base for the next phase of subsystem development (i.e., an engineering model).

Solar Electric Propulsion Thrust Subsystem Development

I. Introduction

The functional demonstration of a Solar Electric Propulsion (SEP) Thrust Subsystem (TSS) has been the primary goal of the JPL Solar Electric Propulsion System Technology (SEPST) Program since 1966 (Refs. 1 through 6). The TSS concept, upon which the SEPST experimental program is based, has been described in the referenced papers and has remained essentially unchanged during the last five years. The resulting TSS, including hardware, software, control techniques, and general operation philosophy can be considered a baseline for constructing and evaluating other TSS designs. The present TSS is a breadboard-type design and is not intended to represent a flight unit. However, all functions anticipated to be required for TSS operation on a planetary vehicle have been included.

Other reports have described the general nature of SEP missions and general TSS requirements (Refs. 7 through 12). This report summarizes the results of the third phase of the SEPST program (i.e., SEPST III). The first (Ref. 13) and second (Ref. 5) phases of the program dealt with element and initial system testing problems respectively. Detailed element descriptions are presented here, although much additional information is contained in the references. Emphasis is placed on system integration, testing, interactions, and the implications of certain interactions or problems on the subsystem operation. Finally, problem areas requiring further detailed investigation for proving TSS compatibility with other anticipated vehicle subsystems are outlined.

Subsystem testing, including element final integration and a 1500-h functional test, was performed over a period of six months. The tests were directed primarily toward demonstrating the basic TSS functions: (1) power matching, with variable solar-array (simulator) output voltage, (2) thrust vector control, and (3) TSS automatic control. In addition, individual element tests were performed to evaluate specific problems and to check performance not demonstrated by subsystem operation.

II. Thrust Subsystem Description

A. General Functions

The elements used in the SEPST III test and the functional relationship of these in the TSS are presented in Fig. 1. Four basic functions are illustrated: (1) conversion of electrical power to thrust, (2) thrust vector control, (3) TSS command and control, and (4) propellant supply.

The first function is the underlying basis for electric propulsion. Solar power, simulated in this test by dc power supplies, passes through an interface box and enters the power conditioners (PC). Each PC has ten power outputs that are connected through switches to thrusters. The thruster is an electron bombardment type (Ref. 14) that uses the power to produce and accelerate mercury ions.

The second function, thrust vector control (TVC), is required to maintain vehicle three-axis attitude control. The use of multiple thrusters, to provide efficient power

Fig. 1. SEPST III block diagram
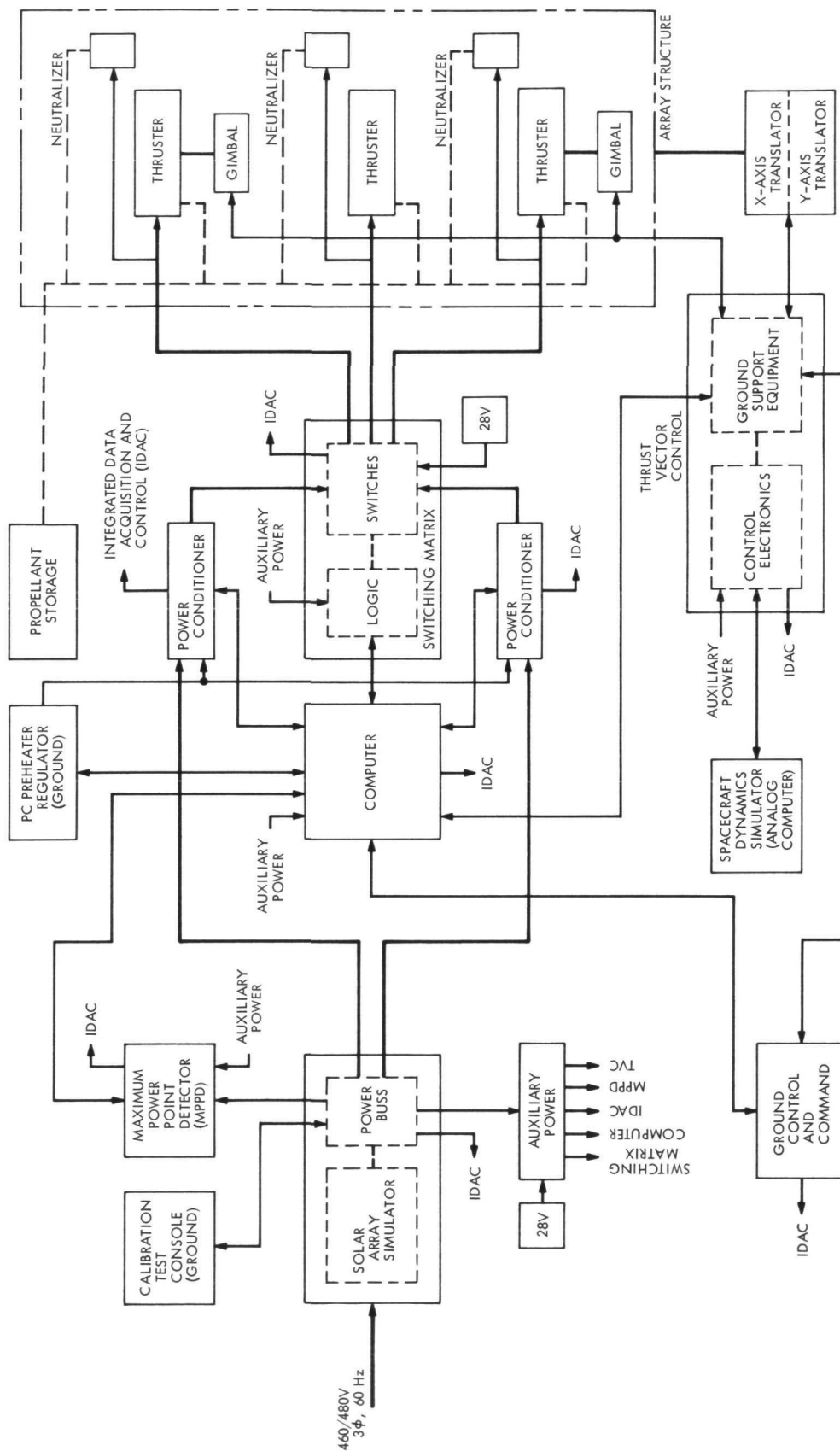
throttling and redundancy, results in relatively large thrust vector movements when thrusters are turned on and off. The present TVC technique translates the thruster array in two orthogonal directions for control about two axes, and gimbals pairs of thrusters around the thruster array diagonals for third-axis control. The TVC drive electronics, including a closed-loop control system, is shown (Fig. 1) connected to an analog computer. The computer, programmed to simulate typical vehicle dynamic response to thrust vector and other vehicle errors, is used to demonstrate the TVC system response and stability.

The third function illustrated in Fig. 1, TSS command control, is required to varying degrees of complexity depending upon mission requirements. The tradeoff of ground commands against automatic onboard control will depend upon communication capabilities and upon allowable inflight performance variations. The present subsystem provides automatic functions such as PC-thruster set selection, startup, power matching, failure detection, and failure evaluation by means of a PDP-11 digital computer. In addition, it provides for manual operation of the PCs (and therefore the thrusters) and the switching matrix.

The fourth function, propellant supply, provides the transfer of liquid mercury from a zero-gravity propellant tank across the TVC mechanism to the thrusters. This includes tank pressurization (using Freon 113) of a neoprene bladder and mercury transfer through flexible feedlines.

B. Thruster

An SEP system is basically designed around the thruster and the thruster operating characteristics. In the last few years, the mercury electron-bombardment ion thruster has become highly developed and is presently ready for flight development. However, for SEPST III this thruster type had several possible cathode neutralizer, isolator, and ion-optics configurations to be considered and evaluated. These configuration possibilities will be discussed to show the basis for the configuration used in the SEPST III system.

1. Cathode. Three types of cathode were considered: oxide-coated, mercury plasma (hollow), and liquid mercury. The cathode choice had to consider development status, reliability/life, power requirements, testing convenience, and system integration (Ref. 15).

The oxide-coated cathode, which depends on thermionic emission from a coated metal surface, has been used extensively, is highly convenient, and presents the least integration difficulty. However, the life expectancy is rather low (500 to 1000 h) and the power requirement is high (100 to 200 W).

The hollow cathode, which also appears to utilize the thermionic emission process (Ref. 16), has been tested in many laboratories and was used on SERT (space electric rocket test) II (Ref. 17). Mercury-vapor flow through the cathode is required for normal operation. This flow apparently produces an intense discharge within the cathode and provides radiant and bombardment heating. After the cathode emission reaches a few amperes, external heating is not required. In addition, the hollow cathode is relatively small and requires only 20 to 30 W of heating power for starting. In comparison with the oxide cathode, the hollow cathode has improved life (5,000 to 10,000 h) (Ref. 17) and lower power, but has more difficult testing and system integration requirements due to the additional feed system.

A liquid-mercury cathode (LMC) for ion thrusters was developed at the Hughes Research Laboratories (Ref. 18). For this cathode, electron emission originates at an arc spot in the liquid-mercury pool. The LMC has demonstrated long life, requires no heating power, and requires only one main feedline. However, high-voltage isolation of the propellant and thruster is more complicated because liquid flow rather than vapor must be isolated and the flow control is rather pressure sensitive. LMC development was terminated after the hollow cathode gained wide acceptance as the best cathode choice.

The hollow cathode was chosen for the final SEPST III system testing. However, initial testing was performed with an oxide cathode. The oxide cathode thruster was integrated with the Model BB-1 power conditioner (Ref. 19).

2. Ion optics. Two ion-optics system types were considered for use with the thruster. The first was the conventional two-grid system (screen and accelerator). With proper design, the two-grid type will operate with a specific impulse from 25 km/s (2500 s) up to any value required for expected missions (up to 50 km/s). Grid life is determined only by accelerator thickness.

Two-grid optics systems are presently under development at NASA LeRC (Ref. 20) and Hughes Research Laboratories (Ref. 21). The concepts being investigated include the use of screen-accelerator interelectrode spacers

(Ref. 21) and grid "dishing" (Ref. 20). Both concepts are intended to maintain a constant interelectrode gap for proper ion focusing.

The second ion-optics type was the insulated or coated grid concept (Refs. 22 and 23). This scheme eliminates the screen grid that ordinarily provides the discharge plasma boundary. The plasma boundary is provided by an insulated coating on the accelerator. Present designs utilize a glass coating, although ceramic coatings have been proposed. The coated grid concept operates over the specific impulse range of 2100 to 3300 s and would extend the specific impulse range of the two-grid system. The principal difficulties are the fabrication of high-purity coatings, the frailty of the coating after fabrication, and the testing ground facilities where sputter contamination is significant. Lifetimes up to about 500 h have been achieved with the coated grid (Refs. 22 and 23).

A two-grid ion-optics system was adopted for the present system. For the SEPST III design the interelectrode spacing is controlled by three internal rods supporting the screen grid (Ref. 24). This design provided the required specific impulse, life, and mechanical strength without special fabrication processes.

The 20-cm (anode diameter), 2.5-kW thruster used in the SEPST III program is shown in Fig. 2. This size thruster was selected early in the program as a likely choice for 5- to 15-kW systems with specific impulse on the order of 40 km/s (4000 s). More recent studies show that larger (30-cm) thrusters with lower (30-km/s) specific impulse are desirable. However, the 20-cm thruster system adequately demonstrates the TSS functional performance requirements.

3. **Neutralizer.** Initially, a cesium plasma-bridge neutralizer was used in the present program (Refs. 3 and 25). Cesium, which produces a low-work-function cathode, resulted in relatively low-starting-power requirements, low beam-neutralizer coupling voltage, and a low cesium flowrate. However, cesium is rather inconvenient for laboratory testing because of its reactive nature. Problems were encountered in evacuating the cesium reservoir (to avoid pushing liquid cesium out of the cathode) during vacuum chamber pumpdown, and in avoiding contamination during chamber venting. In addition, the individual cesium reservoirs with an integral cathode assembly made neutralizer packaging and integration difficult.

With the alternate neutralizer, the mercury hollow-cathode plasma bridge, the considerations were cathode power, coupling voltage, flowrate, integration, and propellant tankage mass, which was 3% of the propellant mass for mercury against 50% for cesium. The extra cesium required because of individual reservoirs-per-thruster also had to be included. A mercury neutralizer requiring approximately double the flowrate of a cesium neutralizer is equivalent in the total propellant-plus-tankage mass required. For coupling similar to that with cesium, the flowrates with the mercury neutralizer are on the order of 5% of the main flow at full power. Including the testing factor, the flexibility in packaging, and low starting power, the mercury neutralizer using the main mercury supply appears to be the better choice.

The present neutralizer assembly is shown in Fig. 2 (Ref. 26). The cathode is a conventional mercury hollow-cathode type, similar to that used on SERT II, and has a 0.02-cm-diam-tip orifice. The keeper electrode is mounted directly to the cathode and is insulated from the ground screen by the insulators shown. This configuration provided convenient assembly, alignment accuracy, and a cathode radiation shield. A coupling voltage of 12 to 15 V was obtained with neutralizer flowrates of about 0.4 g/h.

4. **Isolators.** The neutralizer isolator requires only low-voltage insulation (typically less than 50 V). Since this value is less than the minimum breakdown voltage in mercury vapor (400 V), almost any insulating method is satisfactory. The device shown in Fig. 2 is an alumina tube bonded to tantalum end caps. Substantial neutralizer testing was performed with thrusters and in a bell jar to study neutralizer performance and operating characteristics. Details of these measurements are presented in Ref. 26.

The hollow-cathode isolator, as with the main isolator, must insulate 2 kV. However, the vapor in the hollow-cathode feedline is at higher pressure (a few tens of torr) than the main feedline (0.05 torr). The pressure in the main isolator is low enough to prevent voltage breakdown. The pressure in the hollow cathode requires additional consideration. The cathode isolator shown in Fig. 2 uses a series of insulating spacers and solid disks (using alternating holes covered with screen material) to form compartments of short length. If a small amount of leakage occurs through the isolator, the voltage gradient will be relatively linear along the isolator. Thus, each of the compartments is required to support only a fraction of the total voltage. If this fraction is less than the minimum breakdown voltage, isolation is obtained for all pressures. This technique has been used successfully by researchers
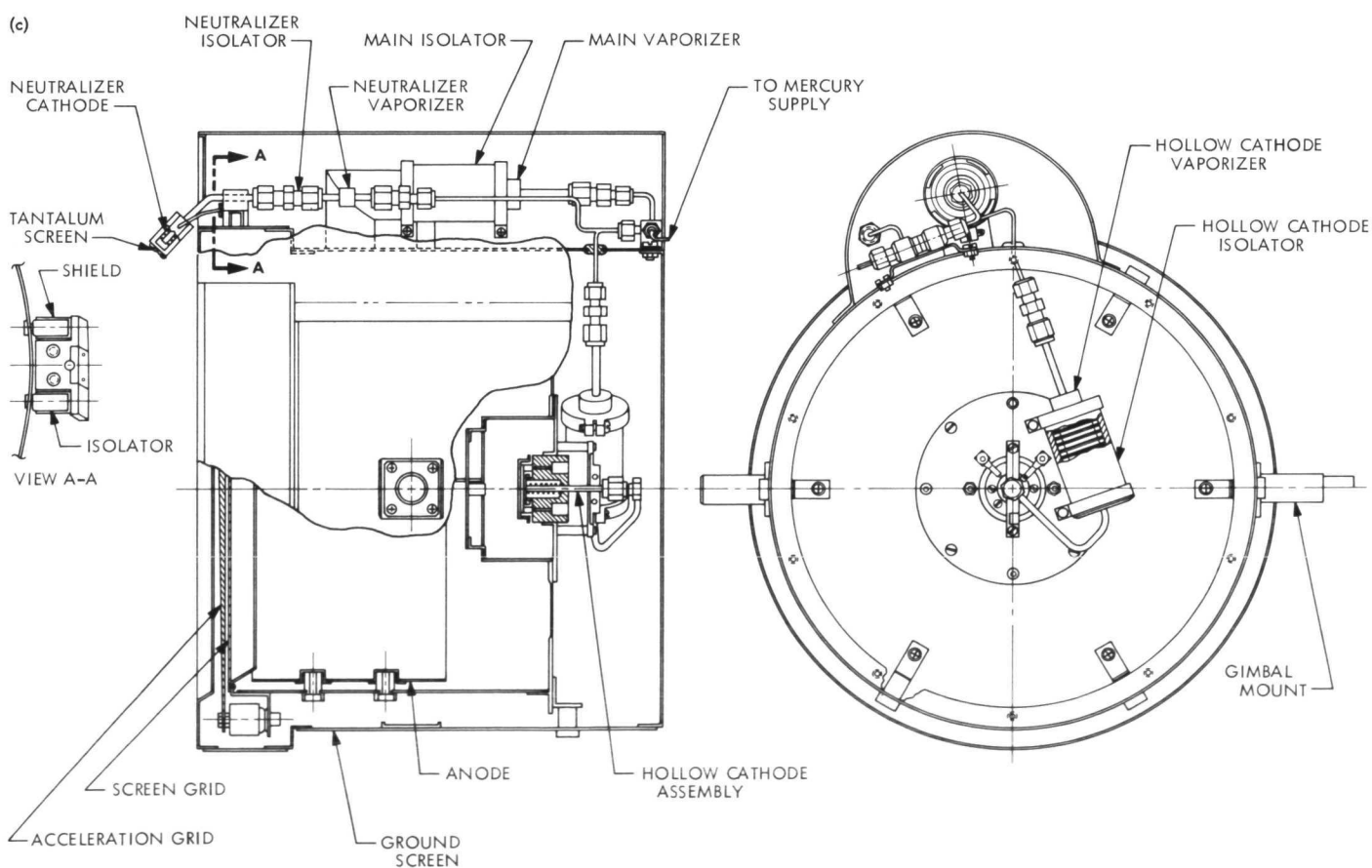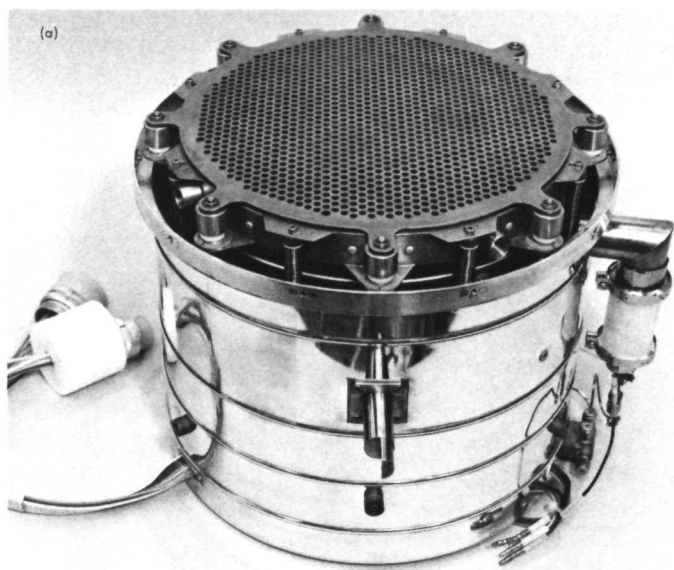
Fig. 2. Thruster configuration: (a) grid side view; (b) back side view; (c) line drawing

at Electro-Optical Systems, Inc. (Ref. 27), and at Hughes Research Laboratories (Ref. 23).

5. Packaging and thermal control. The packaging illustrated in Fig. 2 was intended to provide the minimum thruster length, including a ground shield. The cathode assembly, at high voltage, required a feedline connection and was used as a basis for determining the package length. The hollow-cathode isolator and vaporizer conveniently lay across the back. The three feedlines were then located in mutual proximity and joined in a common manifold. The main feedline and neutralizer were covered with a common ground screen. All wiring, except the magnet wire, was insulated with TFE-type Teflon. The wiring, in the form of ribbon cable, had to be flexible to accommodate thruster gimballing. This feature will be discussed further in conjunction with the TVC mechanism.

The use of the hollow cathode creates a packaging problem that has a major effect on thruster design and is basically a two-part problem. First, the high-pressure hollow-cathode vapor feedline is subject to condensation, particularly during startup. Since the vaporizer and cathode heaters are designed for efficient operation without providing for auxiliary preheating of the line and isolator, the heaters require up to several hours to raise the feedline temperature above the condensation point (about 150°C). By the time the feedline is up to temperature allowing the thruster to start, a substantial amount of mercury has condensed. As the thruster and feedline warm up further from heating by the discharge, the temperature of the feedline controls the hollow-cathode flow. Until all the condensed propellant is used, the hollow-cathode vaporizer has no control over thruster operation.

The second part of the problem concerns steady-state operation. When operating at full power, the thruster housing temperature is about 250°C. If the hollow-cathode feedline is fully enclosed within the ground screen, the vaporizer also reaches this temperature. This level is the vaporizer normal operating temperature and is no longer controlled by the heater element. Thus, there are two opposing requirements: (1) adequate heat transfer to the feedline with low transfer away for startup, and (2) low heat transfer to and/or high heat transfer away during steady-state operation. Two approaches are apparent. First, the feedline can be well insulated from the thruster to reduce heat input during steady state. The long starting time must be acceptable. Second, sufficient cooling paths can be provided for steady-state

operation with additional preheating power provided during startup. This second approach has the advantage in that it solves both the thermal balance and condensation problems.

Prior to the initiation of the thruster discharge, the discharge power supply, ordinarily with several-hundred-watt capability, is available for preheating. A series of heating elements on the thruster and cathode feedline has been used in conjunction with a Klixon thermal switch. The thermal switch, mounted to the rear surface of the thruster (switch in the open or hot position), removed the heaters from the circuit.

The 20-cm-diam thruster as described in this section provided a reference point for further analysis. Units of this type (Fig. 2) presently weigh about 4.5 kg. Lighter gauge materials are expected to reduce this weight to about 4.1 kg.

Thruster power efficiency (η_p) and total efficiency (η_t), for the present technology, are presented in Fig. 3 as a function of true specifce impulse. As shown, propellant utilization efficiencies near 90% produce optimum total efficiency.

The throttling characteristic of present thrusters is shown in Fig. 4. Throttling ratios up to 3 can be achieved, but a total efficiency loss of about 7% is incurred. The efficiency loss is about 3% for a throttling ratio of 2.

C. Power Conditioning

1. PC alternatives. In general, two basic approaches to power conditioning are being considered for SEP systems. With the first approach, a portion or all of the PC/thruster power is conditioned on the solar array before transferring the power to the TSS. This is termed "integral" power conditioning. The second approach is the conventional "separate" power conditioning. The "integral" PC approach (in conjunction with high-voltage arrays) has been proposed most recently, while the "separate unit" PC approach is more conventional and was used in the JPL program.

The integral approach, carried only through feasibility studies at this time, is an attempt to reduce weight and possibly improve conditioning efficiency by producing the required power supplies, including the high-voltage supplies, from digitally controlled solar-cell arrays. A hardware feasibility study is presently in progress at Hughes Research Laboratories (Ref. 28). However, con-

Fig. 4. Thruster throttling characteristics
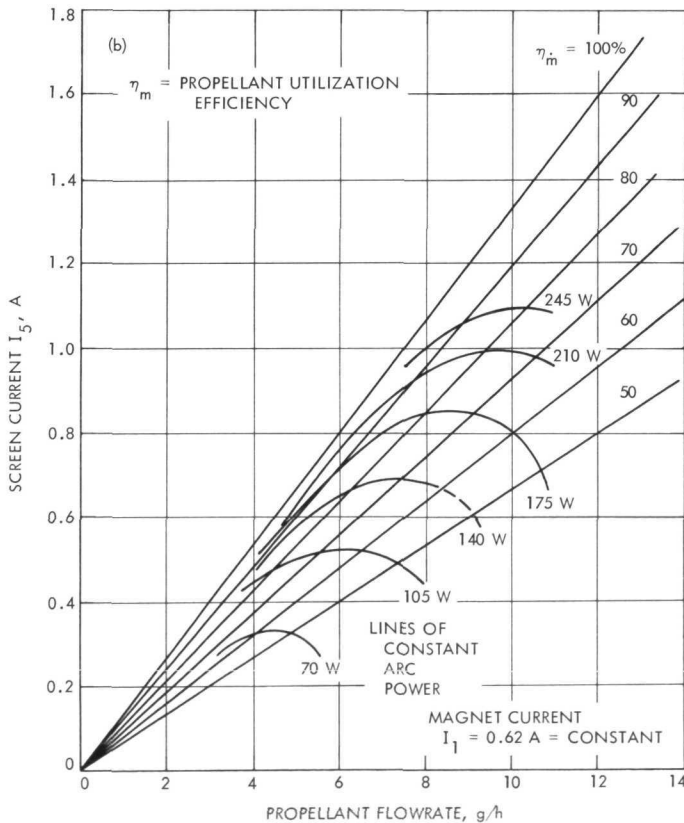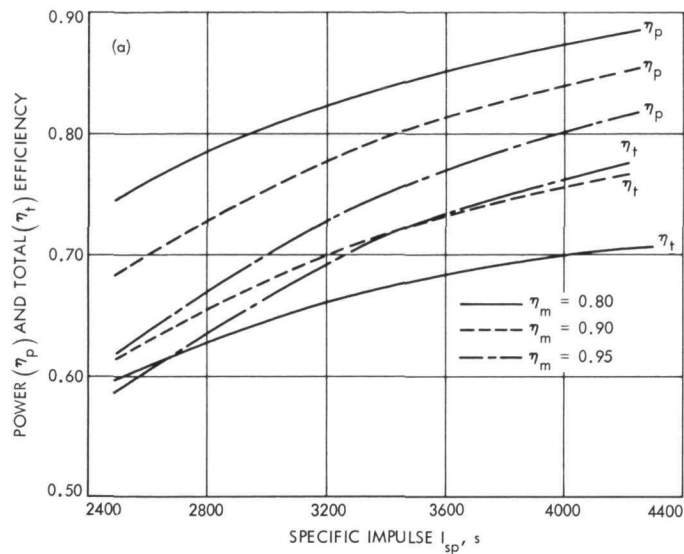
Fig. 3. Thruster performance: (a) power efficiency and total efficiency as a function of specific impulse; (b) performance map for hollow-cathode configuration

sidering the complexity, integration, reliability, and manufacturing problems of such a system, the integral PC technology will probably require several years of development before reaching the status of conventional power conditioning.

Conventional or separate unit conditioning, using either transistors or thyristors as switching elements, can be approached in two ways. First, since input line regulation is required by array-voltage changes, the regulation could be performed on the total power in a modularized unit separate from the thruster PC. The positive feature of this two-unit technique is that the solar array could be standardized for a multimission vehicle (inbound or outbound). Only the basic line regulator would need modification for different missions. However, this multimission convenience is offset by an expected total PC-weight increase of about 30% over the one-unit approach.

The second method of separate unit PC design performs the line regulation within the individual power supplies, using pulse-width or frequency modulation. Although this method provides a simple and efficient regulation scheme, the design depends strongly on the range of input voltage variation. The switching elements' (transistor or thyristor) current capability at the low line voltage determines the maximum power rating of each inverter. To maintain high efficiency with transistors, switching times must be fast (on the order of 5×10^{-7} s). This speed can be obtained presently with several applicable power transistors (Ref. 29). However, to meet the efficiency and power requirements, the high-power portion of the transistor system is constructed in modular form with each module producing 250- to 400-W nominal power. This modular approach is basically lighter for a given reliability than a single inverter (which could be built only with slow transistors) because partial redundancy can be used.

The situation with thyristor switching elements is rather different from that for transistors. The present units can switch up to 500 A at 1200 V. However, this device has a slow switching speed (milliseconds) and must be used carefully to avoid large switching losses. A program to demonstrate efficiency and weight capabilities of a thyristor PC is being conducted at TRW (Ref. 30), managed by NASA-LeRC.

The present thyristor design approach uses a series inverter producing a sinusoidal ac output (Ref. 31). This design is in contrast with the parallel inverter technique, which produces a square-wave output. The sinusoidal wave form results in low switching losses, even though the switching speed is low, since voltage is switched with near-zero current. However, the low switching losses may be offset by the saturation, or resistive, losses that are high relative to transistors. In addition, since a single inverter is used to produce the screen power, or high power, a large input filter is required to suppress ripple induced on the input line. Line regulation is achieved by pulse-width modulation. This technology appears to be a year or more behind that of transistor power conditioning.

As implied throughout the previous discussion, the SEPST III system used modularized transistor inverters. The modular design has benefits in addition to reliability. All modules can be mounted on a single panel allowing direct radiation to space. The panel structure is not required for heat transfer and is constrained only to meet launch loads. The weight is well distributed on the panel allowing a light structure design.

2. **Breadboard Model BB-0.** Transistor power conditioner development, using self-radiation cooling and modular screen-supply design, has been in progress since 1964 at Hughes Aircraft Company (HAC). The original unit (termed Model BB-0) was designed for the oxide-cathode thruster and did not include precise regulation (Ref. 32) (±5% regulation with ±20% line voltage change). Regulation of the screen supply (about 80% of the PC power) was obtained by switching inverter modules in or out of the circuit. A 500-h thermal vacuum test was performed with a SERT II thruster (at about 1.5 kW). This PC was then modified to operate a 2.5-kW JPL thruster (Ref. 5). This work established control-loop operation and techniques for PC recycle during thruster arcing. The original unit was further modified (Model BB-0M) at JPL to operate the hollow-cathode thruster (Ref. 33). This PC was the unit used in the SEPST II testing phase (Ref. 5).

3. **Breadboard Model BB-1.** In view of the requirements for light weight, high efficiency, low induced-input line ripple, and line regulation, the development of a second power conditioner was started in 1968. Designed for an oxide cathode, this unit incorporated control and recycle procedures previously established, and utilized the more advanced electronic components then available. The first unit (Model BB-1) was delivered in June 1969 for evaluation and is shown in Fig. 5. Integration and evaluation occurred over a period of 5 months, including two long-term tests of 800 and 500 h, respectively (Ref. 19).

The requirements for light weight, line regulation, high efficiency, low ripple, and reliability have resulted in a design that is characterized by the following features (Ref. 34):

(1) A synchronized, pulse-width-modulated, staggered-phase drive for multiple inverter modules to reduce input and output filter weight and electromagnetic interference (EMI).

(2) The use of 400-V, high-current (20-A), high-speed silicon transistors (Solitron No. SDT-8805 on Model
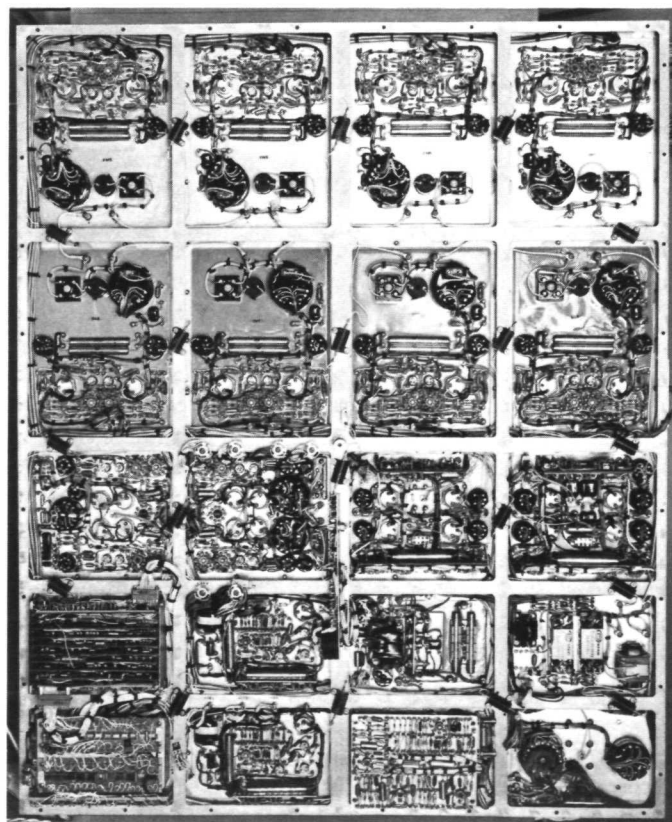
Fig. 5. Hughes Aircraft Co. power conditioner (Model BB-1, 2.75-kW input)

BB-1, Transitron No. ST-18037 on experimental models 1 and 2 (EX-1, EX-2)) stressed up to one-half the maximum rating both in current and in voltage.

(3) An extension of converter frequency to 10 kHz for dc-dc converters. The frequency of 10 kHz was chosen to minimize the combined transistor and transformer losses. (Transistor losses increase while transformer losses decrease with frequency.)

(4) The extensive use of high-Curie-point ferrites for power transformer cores.

(5) A thermally self-sufficient design, requiring no supplementary radiator, resulting in a large-area, low-height geometry.

(6) Use of thermally self-sufficient functional modules, eliminating low thermal impedance, permitting high-weight transfer of heat before direct radiation to space. (A low thermal surface density of 0.04 W/cm^2 is used for 25°C radiator temperatures.)

(7) Mounting of dissipative components directly on the radiator, reducing the weight of component mounting.

(8) A high-strength, low-weight, dip-brazed aluminum, "egg-crate" structure to support functional modules, permitting edge mounting of the PC structure to the spacecraft, with minimum weight in the vehicle structure.

(9) A low-voltage stress, both dielectric and surface, for high-voltage circuitry, made possible by large-area, low-density packaging.

(10) A high level of functional circuit redundancy, made possible by use of low-power (250-W) inverter modules with a total maximum power output capability of approximately 3 kW.

(11) Use of redundant, standby inverters for high system reliability.

(12) Extensive use of integrated circuit digital and analog components.

These features apply to all the PCs discussed in the following subparagraphs.

a. BB-1 configuration. The power-conditioning unit (Ref. 34) is shown schematically in Fig. 6 and its power-supply requirements are listed in Table 1. The screen power is produced by means of eight series-connected converters; each converter consists of a 10-kHz inverter
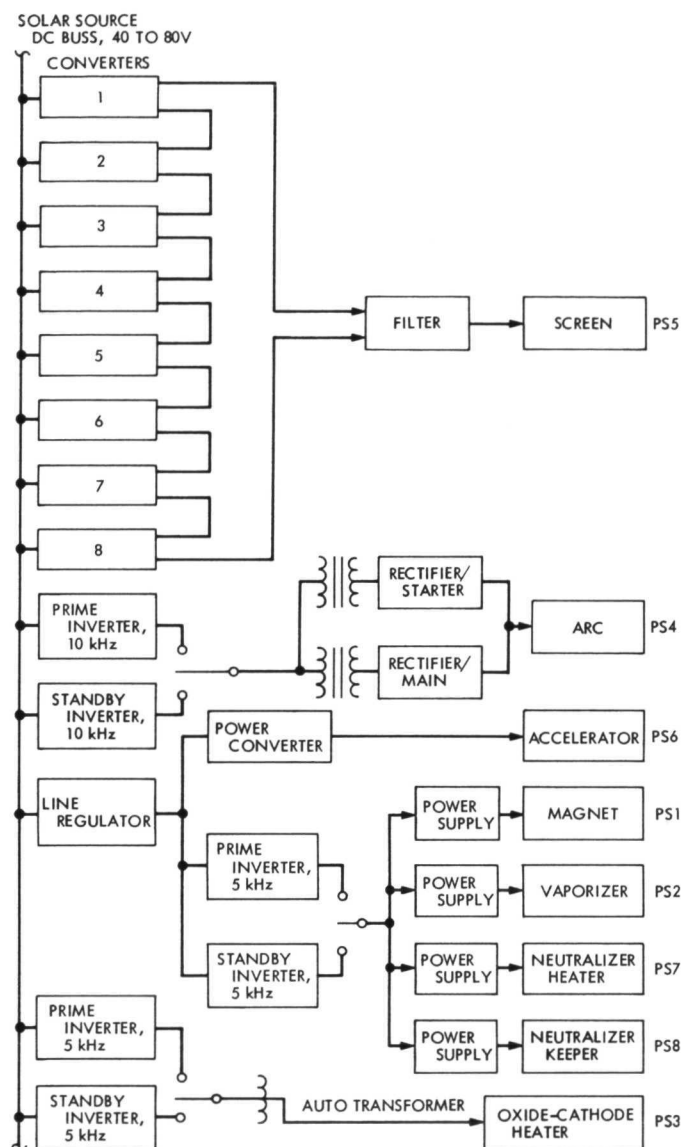
Fig. 6. Oxide-cathode power conditioning unit

and one transformer-rectifier set. An output filter is provided for attenuation of the ripple.

The arc power is derived by means of a converter using one 10-kHz inverter feeding two transformer-rectifier units that are connected in parallel; one serves as the arc starter, the other feeds the main arc. A redundant, standby 10-kHz inverter is provided for emergency and automatically replaces the prime inverter in case of failure.

The accelerator power and the power used for the magnet, vaporizer, and neutralizer are derived from a constant 35-Vdc source, obtained from the line regulator. Two 5-kHz inverters supply the power to the magnet,

Table 1. Model BB-1 power supply ratings (oxide cathode 20-cm-diam thruster)

Group	Power supply No.	Power supply name	Type	Output[a]	Maximum ratings[b]			Nominal range					
					Voltage, V	Current, A	Limiting current, A	Voltage, V	Current, A	Power, W	Peak ripple, %	Load regulation of output voltage, %	Range of control
I	1	Magnet manifold heater	dc	F	19	0.85	0.90	15	0.67	10.5	3.5	–	–
	3	Cathode heater	ac	V	5	40	45	4.5	35	160	–	–	10 to 40 A
	7	Neutralizer heater	ac	V	12	3.4	4	12	2.8	35	–	–	0.3 to 3.4 A
	8	Neutralizer keeper	dc	F	300 at 5 mA	20 mA at 95 V	0.55	10	0.50	5	5 at 10 V	1.0	0.02 to 0.5 A
II	2	Vaporizer	ac	V	10	2	2.05	5.5	1.1	6	–	–	0.5 to 1.2 A
	4	Arc	dc	V	150	7 at 35 V	8	34.5	6	207	1.25	2.2	2 to 7 V
	5	Screen	dc	V	2260[c]	1.0	1.05	1980	1.0	2000	3.8	4.4	0.5 to 1.0 A
	6	Accelerator	dc	F	2710[c]	0.11	0.115	2170	0.005	11	2	5.8	–

[a]Output: V = variable, F = fixed.

[b]At an input voltage of 80 V.

[c]At no load.

vaporizer, and neutralizer; one inverter is redundant. As in the case of arc inverters, the changeover from prime to standby inverter occurs automatically upon the failure of the prime unit. The same 5-kHz inverters also provide the housekeeping power for the electronic control circuits of the PC.

The ac power for the oxide cathode is supplied by a separate 5-kHz inverter. This power is transmitted at relatively high-voltage level from the power conditioner to a stepdown transformer located near the thruster. This reduces the line losses. A standby inverter is available for redundancy. Commands for turning the Model BB-1 on and off are shown in Table 2. This sequence was modified slightly later for the Model BB-1M and experimental PC units.

Table 2. PC commands for Model BB-1

Command	Result[a]
OFF-1	PS2 turned off
OFF-2	All supplies turned off
ON-1	PS1, 3, 7, 8 turned on
ON-2	PS2, 4, 5, 6 turned on

[a]See Table 1 for power supply (PS) designation.

The BB-1 and BB-1M models are designed for mounting from four edges of the assembly, with one support point in the center of the rear face. The cover is removable from the back without dismounting the assembly, making accessible the components and circuit connections, which are located on the rear face of the individual module plates. The outside dimensions are 92 × 76 × 7 cm (Fig. 5). The system consists of an assembly of 20 modules, mounted on an "egg-crate" structure. Individual modules are removable from the front after disconnecting them from harness connectors on the rear face. All external connections are made at connectors located at one end of the assembly, with all low-voltage connections, which are in one corner, made with space-approved subminiature, rectangular connectors. All high-voltage connections are made at the other corner to high-voltage standoffs, with screw terminals. These connections are made behind a small removable connection cover.

The radiating surface of the assembly is electrically "dead" with protruding power transistor studs and nuts covered by epoxy conformal coating. All other components and connections are behind module plates. Thus, the assembly, with its cover, is totally enclosed to provide

EMI shielding and freedom from high-voltage hazard during testing. The clear front surface, unobstructed in a vehicle, provides shielding from incident radiation. Since in a typical vehicle installation, the rear of the assembly would be shielded from radiation by the vehicle structure and other power-conditioning assemblies, the back cover is perforated to reduce weight and permit free outgassing, thereby preventing pressure buildup and transition to regions of voltage breakdown. All materials were selected for low outgassing.

The various modules used in the system are sized in frontal radiator area, for a worst case thermal radiation of 0.45 W/cm² from the front face, assuming no radiation from the rear face. At this level of radiation, with no solar incidence, a worst-case plate temperature of 35°C may be expected. This provides high-reliability operation of components, which, with few exceptions, are mounted on the module plates. With the design philosophy of low surface thermal density, each module is thermally self-sufficient and will not require conduction to the structure and sharing of the radiation area between modules. Thus, hot spots are minimized. Since high reliability is obtained by extensive use of redundant, or standby, circuits, the thermal design philosophy has resulted in packaging of redundant circuits on the same module plate with operating circuits, intermixing the components on the plate to obtain uniform thermal density regardless of which circuit is operating.

The supporting frame forms an egg-crate structure with a web, or I-beam, running between all modules, and a channel section forming the edges. Holes, located in I-beam webs reduce weight, without significantly reducing the section modules. To provide a flat surface for module mounting, the structure is formed by assembling front and back plates, with module cutouts and with webs interlaced in egg-crate fashion, the whole being dip-brazed. The material is 0.040-in. aluminum, 6061-T4, chosen rather than lighter magnesium, to permit dip brazing of thin sections. A riveted magnesium structure of the same strength would be heavier.

b. BB-1 test setup. A diagram of the test setup is shown in Fig. 7. The power-conditioning unit power outputs were connected through manual switches and instrumentation to the thruster. The switches allowed thruster operation with either the PC or laboratory power supplies. Magnetic-amplifier-type current transducers were used to monitor important parameters. The PC telemetry outputs were connected to a patch board and through buffer amplifiers to a magnetic tape recording
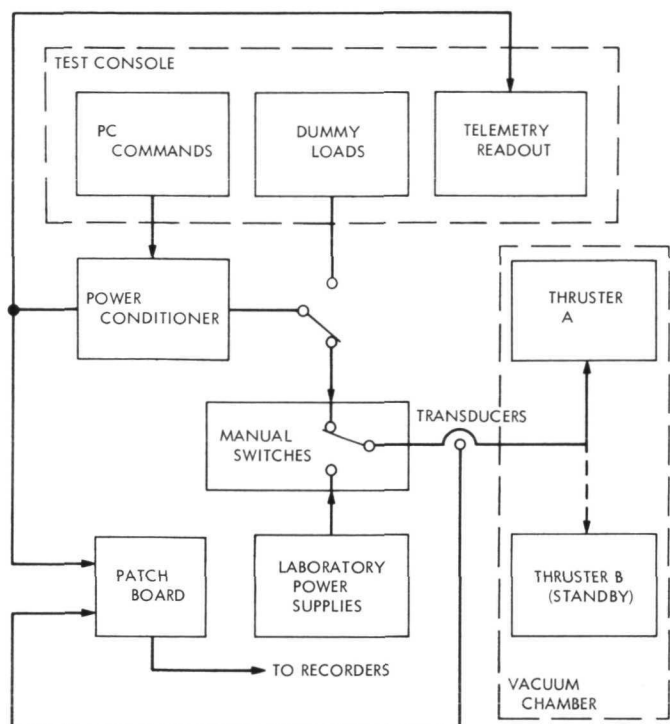
Fig. 7. Laboratory test setup for Models BB-1 and BB-1M

system, used in evaluating the PC recycling program. Commands were generated at a control panel in the test console, which also provided dummy loads for initial checkout and subsequent trouble shooting.

The thruster setup used in testing BB-1 is shown in Fig. 8. Note the use of "local" transformers for reducing transmission of high cathode heater current. Wiring between the transformer and the high-temperature cathode terminals was cooled with boron nitride heat sinks to prevent transformer overheating while maintaining low-voltage drop in the wire.

c. BB-1 integration results. Arcing of the thruster, principally due to contamination by material sputtered from the vacuum chamber walls, is known to cause disturbances that can interfere with the proper functioning of the electronic controls of the PC. The arcing of the thruster caused rapid changes in current levels that, through the ground loops, were crossfed into the micrologic of the PC. The major results of this interaction were:

(1) Erroneous changeover from prime to standby 5-kHz inverter.

(2) "Latch-up" of an RA-909 amplifier used to feed back the arc current signal that controls cathode

power. (It was later determined that latch-up occurred because of a defectively manufactured device.)

(3) Noise-triggered shutdown of PC.

(4) Noise contamination of telemetry lines. More detail related to these experiences is contained in Ref. 19.

Initially, it was thought that the penetration of noise into the digitally integrated circuits occurred only through the input lines and housekeeping dc-supply lines. Later, another path for noise penetration into the digitally integrated circuits was found to exist; i.e., capacitance between the integrated circuit unit and the mounting board and panel of the power conditioner. When thruster arcing occurred, the high (300-V) potential between the signal ground used by the integrated circuits and the ground plane of the mounting board allowed substantial amounts of energy generated during the arcing to be stored electrostatically and, subsequently, to penetrate into the digital circuits.

To make the PC immune to this transient interference, two steps were taken. First, additional noise-suppression filters were added on all the critical inputs and housekeeping dc-supply lines within the micrologic. Second, the grounding scheme of the screen power supply was modified from that of Fig. 9a to that of Fig. 9b. With this change, the screen current (I_s) no longer flowed through the signal ground ring (Fig. 9b) and the transient on the signal grounds was reduced to an acceptable level.

As indicated in Ref. 19, other minor problems were experienced with the magnet power supply (due to back-voltages induced by thruster arcing), with screen-supply ripple, and with smooth recovery from recycle. After all the modifications were introduced, the closed-loop system was operated for 500 h. During this period, the system performed satisfactorily with no manual intervention required. This demonstrated that the cures introduced were satisfactory. The 500-h run was terminated voluntarily after it was felt that sufficient confidence had been gained in the performance and reliability of the improved circuits to warrant their acceptance.

The BB-1 integration and testing were directed toward development of the circuit and servo-loop design. Efficiency, weight, ripple, regulation, and reliability were not specifically evaluated. However, substantial effort was expended in evaluating these quantities in the hollow-cathode version of BB-1 (i.e., BB-1M).
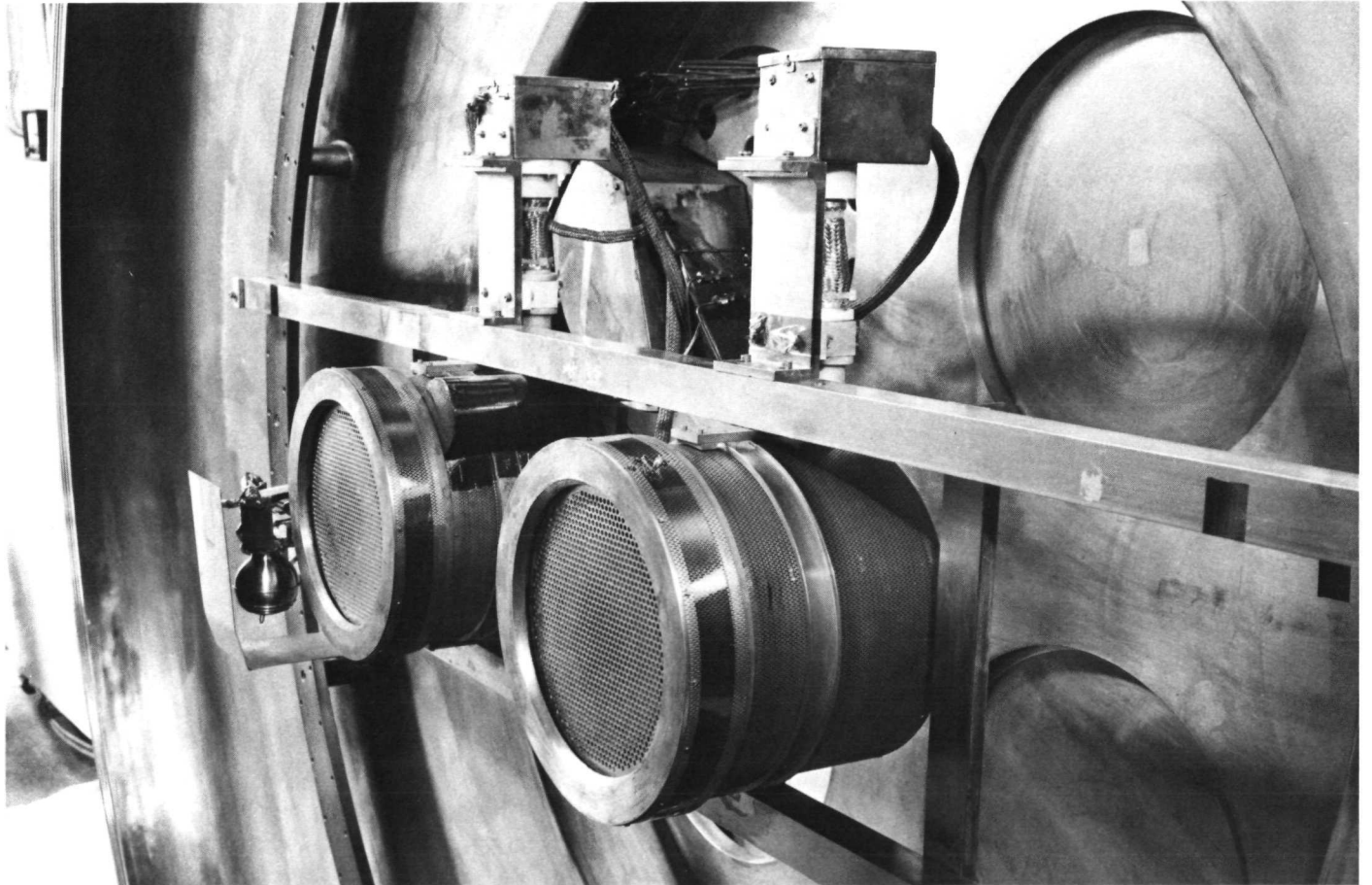
Fig. 8. Thruster setup for Model BB-1 power conditioner testing

(a) OLD CONFIGURATION
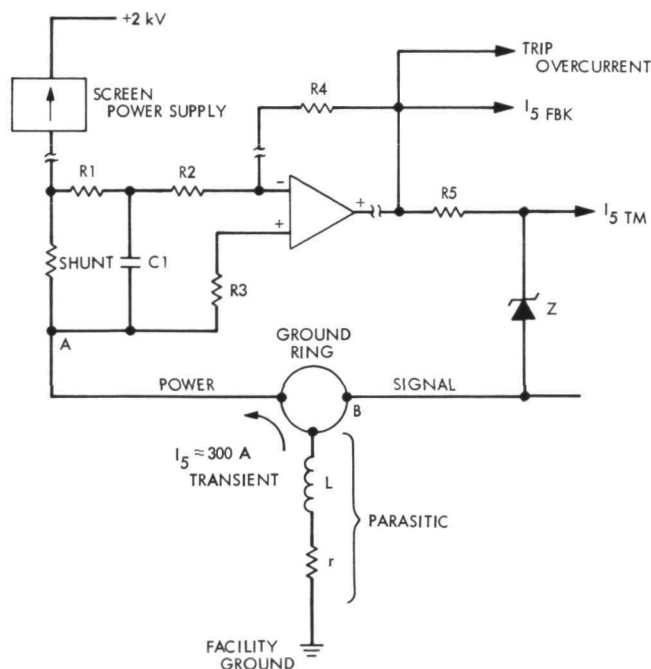
(b) NEW CONFIGURATION (C2, R6, AND R7 ADDED,
OTHER COMPONENTS UNCHANGED)
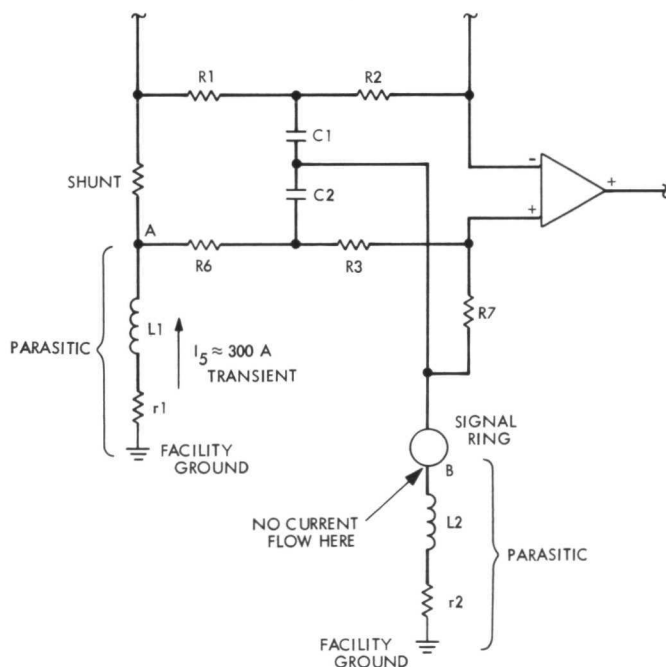
Fig. 9. Grounding scheme of screen power supply

Fig. 10. Hollow-cathode power conditioning unit BB-1M
and experimental model

Table 3. The supplies modified or added to accommodate the hollow cathode are PS3, 4, 9, and 10 (Fig. 10). To accommodate hollow-cathode thruster requirements, the arc supply was increased in output power capacity at low line. To avoid having to completely reconfigure the system while maintaining standby redundancy, an increase in the low-line voltage from 40 to 53 V was accepted. The reduced input voltage range resulted in a somewhat higher PC efficiency and did not substantially affect the design.

a. BB-1M configuration. A block diagram of the BB-1M unit is shown in Fig. 10 and the PC-thruster servo-loop

4. Breadboard Model BB-1M. Oxide-cathode life limitations required the thruster and PC to be modified to a hollow-cathode (HC) configuration. The requirements to which the BB-1M unit was designed are shown in

Table 3. PC power requirements (hollow cathode, 20-cm-diam thruster)

Power supply No.[a]	Power supply name	Type	Maximum rating			Nominal rating			Regulation, ±%	Peak ripple, %	Range of control, A	Remarks
			Voltage, V	Current, A	Power, W	Voltage, V	Current, A	Power, W				
1	Magnet manifold	dc	19	0.85	16	13	0.6	8	1 (current)	5	Constant current	Preset within 0.5 to 0.85 A
7	Neutralizer heaters	ac	12	3.4	40	5.2	1.5	8	Loop or 5 (current)	—	0.3 to 3.4	Set I_7 reference within 2.8 to 3.4 A
8	Neutralizer keeper	dc	300 at 5 mA[b]	0.6 at 0 V	5	10	0.5	5	Loop or Fig. 5	2	0.1 to 0.5	Set E_8 reference within 10 to 20 V
9	Cathode heater	ac	8.5	4.8	40	8.5	4.8	40	5 (current)	—	On/off	Manual control only
10	Cathode keeper	dc	300 at 5 mA[b]	0.6 at 0 V	5	10	0.5	5	Fig. 5	2	—	Operates in open loop only
2	Vaporizer, main	ac	10	2	20	5.5	1.1	6	Loop or 5 (current) (I)	—	0 to 2	Set I_2 reference within 1.6 to 2 A
3	Cathode vaporizer	ac	10	2	20	5.5	1.1	6	Loop or 5 (current) (I)	—	0 to 2	Set I_3 reference within 1.6 to 2 A
4	Arc	dc	60 at no load	37.5 at (9+1) A	375	37	(8+1)	333	1 (current)	2	2 to 10	Set I_4 reference within 2 to 9 A
5	Beam	dc	2200[c]	1.05	2100	2000	1.0	2000	1 (voltage) (E)	5	0.5 to 1.0	—
6	Accelerator	dc	1100[c]	0.05	50	1000	0.01	10	1 (voltage)	5	—	—

[a] Group I: PS1, 7, 8, 9, 10; Group II: PS2, 3, 4, 5, 6.

[b] 30 V at 20 mA.

[c] No load voltage.

configuration is shown in Fig. 11. The supply modifications will be reviewed briefly.

The increased minimum input voltage allowed a single arc supply to produce 375 W (10-A maximum, including screen current), while maintaining a standby inverter. On BB-1 at a 40-V input, only 300 W were available. As shown in Fig. 11, the BB-1M arc supply is current-limited with arc-voltage control from the HC vaporizer.

The accelerator supply was a single inverter delivering 1000 Vdc at a nominal current of 5 mA. The nominal steady-state power level of 5 W gave this supply a very

high calculated reliability. For this reason, a redundant inverter was not considered necessary. No output regulation was necessary because power was delivered from the line-regulator source and the output voltage was affected only slightly by the load variation.

The 5-kHz inverter output power was increased to accommodate the new HC supplies (cathode heater, cathode keeper, and cathode vaporizer). This was accomplished by the increased minimum input voltage, which allowed a higher output voltage from the line regulator. The 5-kHz inverter was modified to provide two outputs. One output supplied the original modules (magnet, main
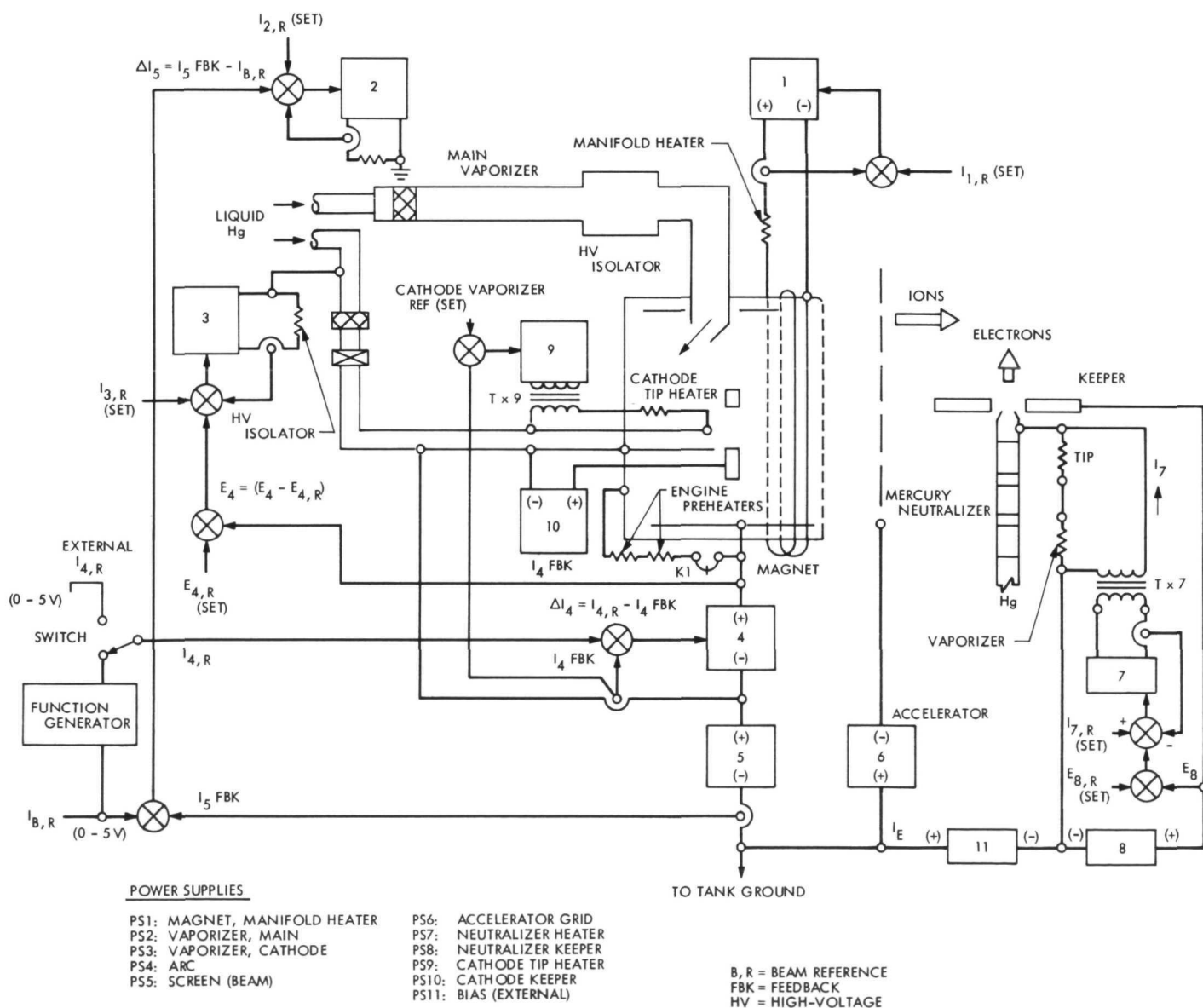
Fig. 11. HC thruster PC control loops

POWER SUPPLIES

PS1: MAGNET, MANIFOLD HEATER	PS6: ACCELERATOR GRID
PS2: VAPORIZER, MAIN	PS7: NEUTRALIZER HEATER
PS3: VAPORIZER, CATHODE	PS8: NEUTRALIZER KEEPER
PS4: ARC	PS9: CATHODE TIP HEATER
PS5: SCREEN (BEAM)	PS10: CATHODE KEEPER
	PS11: BIAS (EXTERNAL)

B, R = BEAM REFERENCE
FBK = FEEDBACK
HV = HIGH–VOLTAGE

vaporizer, neutralizer keeper, and neutralizer heater) at 70 V peak. The second output, at 96 V peak, supplied the hollow-cathode modules.

The BB-1 control module was modified to provide for the arc-voltage-cathode vaporizer control loop, thruster on/off commands, and recycle procedure changes. The on-off commands implemented in the BB-1M and the experimental units are listed in Table 4.

b. BB-1M test setup. The BB-1M test setup was similar to that used for BB-1 (Fig. 7) except for the thruster-array configuration. The BB-1M thruster setup is shown in Fig. 12 with two thrusters mounted in the SEPST III thruster-array structure. This configuration, eventually with three thrusters, was used throughout the test program. The thrust-vector-control mechanism is discussed in Subsection E.

c. BB-1M integration results. In this phase of the SEPST III program, many of the details required to specify the experimental models (EX-1 and EX-2) were investigated. Thus, most of this information and the related analyses are recorded in this section.

Neutralizer. To achieve steady operation for most tests, an electron source outside the thruster was required. Without such a source, the PC operation was erratic with relatively noisy power outputs. This resulted in frequent accelerator spikes and recycles. The neutralizer effect upon the accelerator is shown in Fig. 13. Similar effects were observed in previous work.

Recycle. The screen and accelerator power supplies were protected by a "trip" circuit against overloads. The current transient required to trip these supplies is plotted in Fig. 14 as a function of the transient duration. These

Table 4. PC commands for Model BB-1M and experimental models

Command	Result[a]
OFF-1	PS2 turned off
OFF-2	All supplies turned off
ON-1	PS1, 4, 8, 9, 10 turned on
ON-2	PS2, 3, 7 turned on
ON-3	PS5, 6 turned on

[a]For PS designation see Table 3.
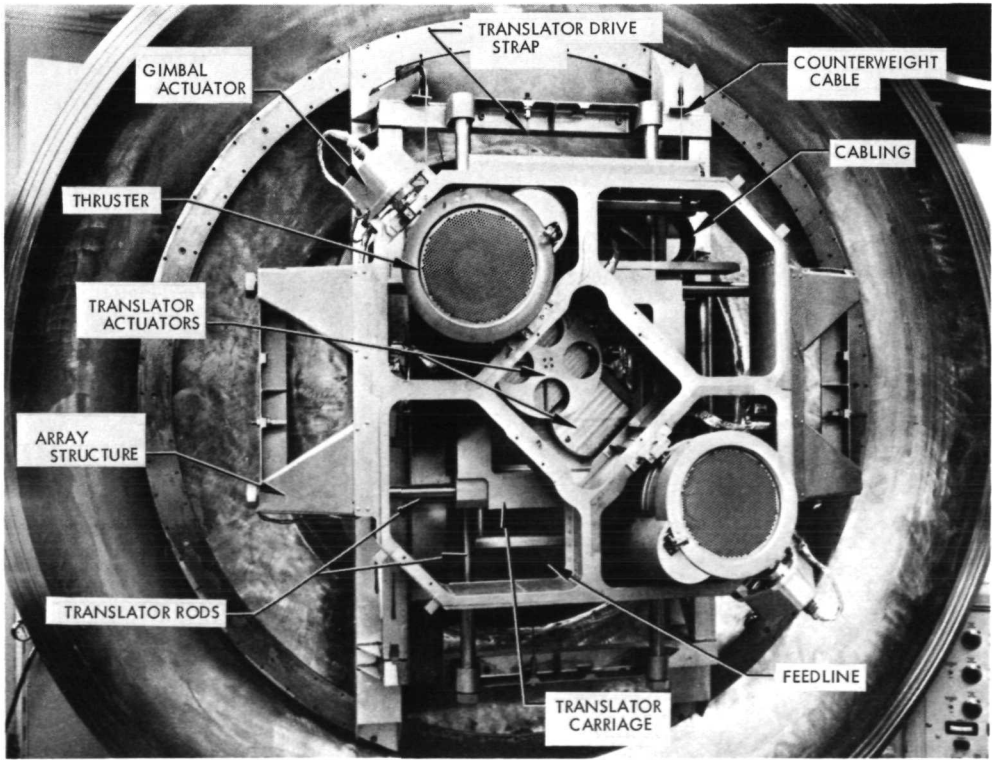
Fig. 12. Model BB-1M test setup showing TVC mechanism
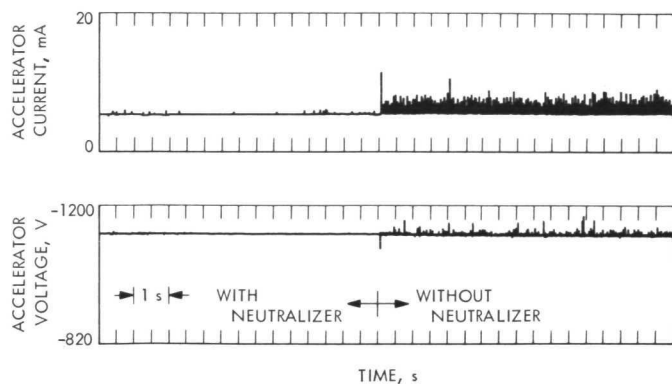
Fig. 13. Effect of neutralizer operation upon accelerator
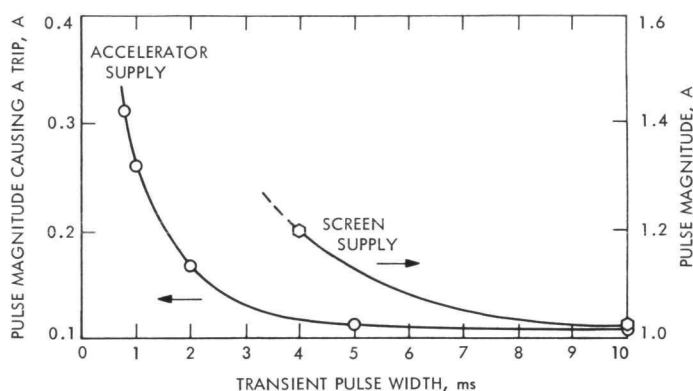
Fig. 14. Current pulse magnitude and duration causing a trip

characteristics also existed on BB-1. The procedures studied for reinitiating high voltage, without causing overshoots that could trip the system again, will be presented here.

The major factor in "soft" recovery from a trip is the magnetic field strength. During a recycle, the magnet current is reduced to a minimum level and then ramped up to the original value. A typical recycle is illustrated in Fig. 15. Both the minimum level during off time and the ramp are important for recovery.

A minimum level of magnet current during the off portion of a recycle greater than 0.10 A caused continuous recycling without recovery. For levels below 0.10 A, the recovery was satisfactory.

Ramp times, measured from the instant of the trip (from 0.5 to 9 s), were evaluated. Long times resulted in slow recovery and large system perturbations. The shorter ramps increased the arc intensity at a rate exceeding the ion-optics perveance limit. That is, the high voltage was too low to focus the ion beam. The ramp rate found to
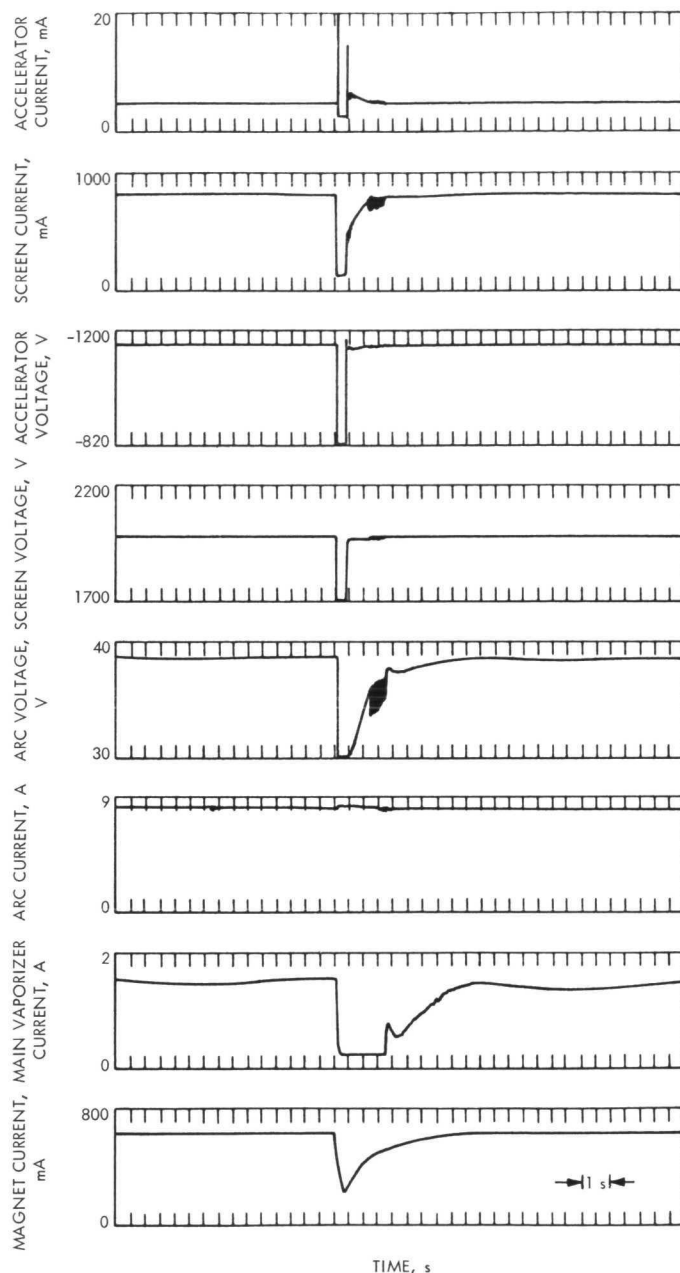
Fig. 15. Typical recycle characteristics

cause continuous recycling was 0.5 s. A ramp time of about 4 s was used in all other tests.

The influence of arc-current level during recycle was investigated with the thruster operating from half to full power. In contrast with the oxide cathode (BB-1), the arc must remain on during recycle for the thruster using the hollow cathode. Initially, it was feared that during recycle at low thrust levels the arc might extinguish. Recycles with the arc current at its normal value and with com-

mand maximum (9-A) level were performed at half and full power. Recovery was found to be satisfactory for both conditions although the recovery at minimum thrust level of beam current of 0.5 A was found to be oscillatory.

The time sequence of bringing the screen and accelerator voltages back on after a trip, is also important. The time between screen and accelerator turn-on was varied by delaying the accelerator turn-on command signal. Since the screen-supply staggered-phase system requires a rather slow turn-on (about 80 ms), the point of reference for turn-on comparisons was the point where full voltage was reached.

Initially, the accelerator reached full voltage approximately 70 ms before the screen. This time difference could not be increased conveniently because of the screen system design. Low accelerator current overshoot on recovery is an indication of the correct turn-on sequence. This overshoot as a function of the turn-on time difference is shown in Fig. 16. The data show that smoother recovery occurs when the accelerator reaches full voltage at least 30 ms faster than the screen. The overshoot increase with smaller and negative time differences is probably due to neutralizer-screen coupling that defocuses the ion beam. The overshoot could be expected to increase for a positive time difference greater than those shown in Fig. 16. Starting the accelerator too quickly would then cause beam defocusing by improper perveance matching.
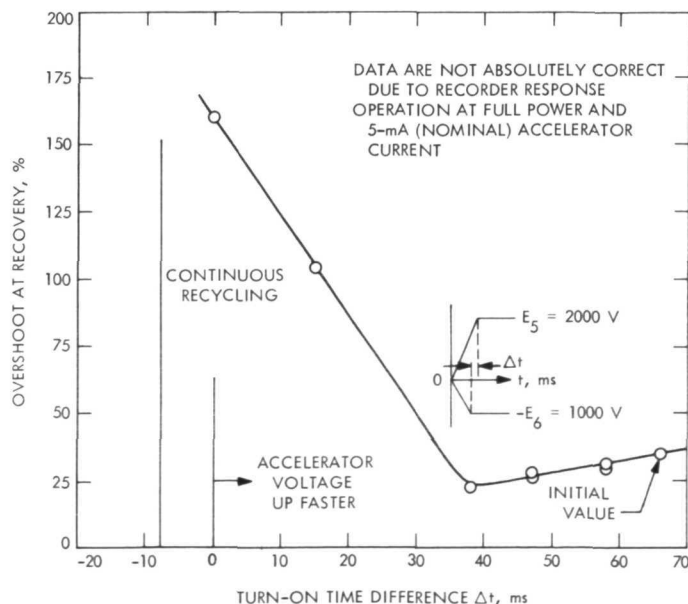
In evaluating general circuit requirements, the behavior of the power conditioner at various levels of the "housekeeping" supplies was studied. These supplies principally drive integrated circuits. The "+12 V" buss was investigated. The power to this buss was provided from an external supply and was varied from 10.0 to 12.3 V. At voltages below 10.0 V and above 12.2 V, continuous recycling occurred. At the lower voltages, the screen power-supply modulator was erratic in operation. At the higher voltages, the minimum magnet current during the recycle increased and was above the 0.10-A level acceptable for a satisfactory recycling.

Cathode keeper current. The HC keeper current was varied in 0.2-A steps from 0.4 to 1.0 A to evaluate arc startup and recycle. Operation at 0.4 A was possible although the starting of the arc was somewhat delayed. Operation between 0.6 and 0.8 A was satisfactory. At 1.0 A, the thruster operation was "noisy" for some power ranges. A keeper current of 0.8 A was selected.

Servo loops. Three basic PC-thruster servo loops are used (Fig. 11) to maintain (1) the thrust level, (2) propellant utilization efficiency, and (3) vehicle potential. These are the screen-current main-vaporizer current, arc-voltage cathode-vaporizer current, and neutralizer-keeper-voltage neutralizer-vaporizer-current servo loops, respectively. The servo-loop characteristics are shown in Fig. 17. These characteristics were derived by adjusting the loop gains to the maximum values not producing oscillations.

Thrust depends directly upon screen current (I_s) and the square root of screen voltage ($E_s^{1/2}$). Figure 17a shows the closed-loop characteristics of the screen-current main-vaporizer servo system. When the beam current exceeds the reference $I_{B,R}$ value, the loop closes and the vaporizer is controlled along the S_2-slope. The exact location of the steady-state operating point on this slope depends upon a number of factors, including the beam-current level, the temperature of the thruster, the condition of the vaporizer, and the overall thermal environment. As the steady-state operating point shifts along the S_2-slope, the value of the error signal, ΔI_s, changes and can become as large as 16 mA at the bottom of the curve. This means that the actual beam current can be as much as 16 mA higher than that specified by the reference $I_{B,R}$. This current variation represents a total thruster variation of ± 0.8 to $\pm 1.6\%$ at full and half power, respectively, provided that $I_{B,R}$ has been properly adjusted to have the steady-state operating point at the level of the desired screen current. Assuming that the average value of the vaporizer current

Fig. 16. Beam current overshoot as a function of the turn-on time difference between screen and accelerator power supplies

Fig. 17. Transfer characteristics

tion results in an opposite propellant utilization variation since the arc power as defined by the arc-current reference remains constant. This can be seen in Fig. 3. Thus, the finite gain of the screen-current servo loop can result in a propellant utilization variation of about ±0.2 to $\pm0.4\%$ when operating at maximum power and along the $\eta_m = 90\%$ (Fig. 3b).

Associated with the thrust variation is a power variation. For constant screen voltage, the change in screen current over the control range represents a ±0.8 to $\pm1.6\%$ screen-power change. Thus, from the nominal operating point power, an additional power margin of about 15 W (at 2 kV) must be provided in both the screen supply and the solar array. This amounts to about ±0.64 to $\pm1.28\%$ of the PC output power at full and half power, respectively.

The arc-voltage cathode-vaporizer loop has the function of maintaining a reference arc voltage. The arc supply current is controlled by an adjustable arc-current reference $I_{4,R}$. The reference may be adjusted internally as a function of the beam-current reference signal $I_{5,R}$ or by an external command. The servo-loop and arc power-supply characteristics are shown in Fig. 17b. Since both the arc current and arc voltage vary as the loop controls, the evaluation of utilization variation must be made on the basis of discharge power.

A plot of arc-current-voltage characteristics over the control range is shown in Fig. 17b. The solid line ($S_4 = 50$ V/A) represents the initial system characteristic and shows a total power change of about 15 W over the normal control range. The arc power can be represented approximately in the form (Ref. 35)

$$P_A = I_5\left[A_1\left(\frac{p}{p_t}\right)^{\beta_1} + A_2\left(\frac{1}{1-\eta_m}\right)\right] \tag{1}$$

where I_5 is screen current, A_1, A_2, and β_1 are constants, and p/p_t is the ratio of any thruster power to full-rated power. The constant β_1 is small (about -0.1) for the hollow cathode thruster. Differentiating Eq. (1),

$$dP_A = I_5 A_2 \frac{d\eta_m}{(1-\eta_m)^2} \tag{2}$$

Evaluating Eq. (2) for a nominal $\eta_m = 0.9$,

$$d\eta_m = \frac{10^{-2} dP_A}{A_2 I_5} \tag{3}$$

I_2 in steady state does not change from the nominal value by more than $\pm25\%$, the thrust variation caused by the screen-current variation will be less than ±0.2 to $+0.4\%$ of the nominal value. However, the screen-current varia-

A typical value of A_2 is 6 eV/ion, giving

$$d\eta_m = 1.66 \times 10^{-3} \frac{dP_A}{I_5}$$

or approximately

$$\Delta\eta_m = 1.66 \times 10^{-3} \frac{\Delta P_A}{I_5} \qquad (4)$$

For the present conditions, $\Delta P_A = 15$ W, so that $\Delta\eta_m = 2.5\%$ at full and half power, respectively.

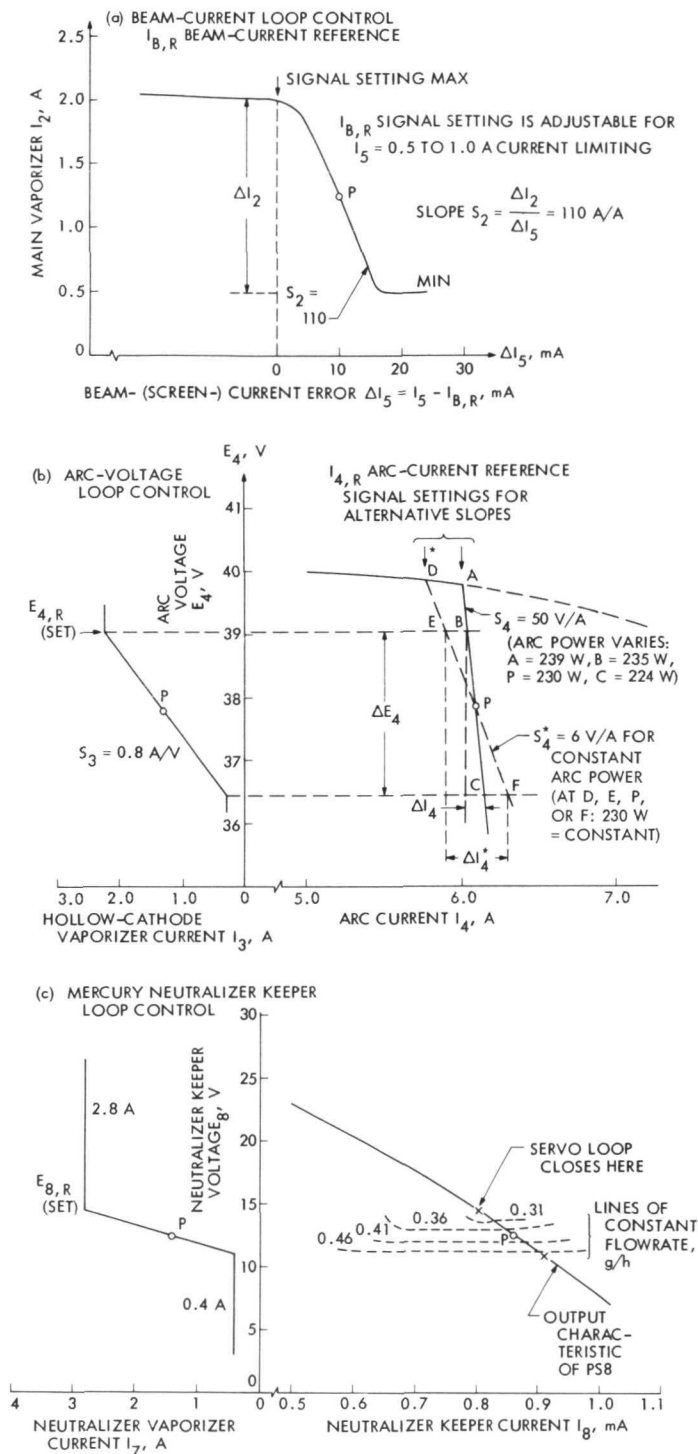Three points are to be noted. First, assuming a $\pm25\%$ variation in cathode vaporizer current I_3 due to warmup or deterioration, causing a steady-state change in arc voltage, a utilization variation of about ±0.35 to $\pm0.7\%$ could be expected.

Second, dynamically the change in arc power (for $S_4 = 50$) in Fig. 17b results in a perturbation of the screen-current main-vaporizer loop. This happens because the arc power supplies the screen-current ions. In addition, coupling occurs in the reverse direction because the main flow affects the required cathode flow.

These control loops were originally "stabilized" by adjusting the arc-voltage loop gain without the above analysis. Although this produced relatively well-behaved thruster operation, the system remained slightly oscillatory. A more desirable arc-supply characteristic is shown as a dashed line ($S_4 = 6$) in Fig. 17b, corresponding with the constant arc-power line. For this slope, the arc-current level adjustment effectively becomes an arc-power level adjustment. Although this does not totally eliminate loop coupling, it eliminates direct coupling. This approach also tends to reduce the utilization variation.

The third point is that with the present arc-supply characteristic, the steady-state operating point may be approached from both the high- and low-propellant-utilization region during the steady-state oscillations. Oscillations, particularly at high screen current for which the stability margin is small (Fig. 3), are prone to cause "runaway." The constant arc-power slope was found to reduce this problem.

The neutralizer maintains a given vehicle potential, with respect to the local space plasma, by injecting electrons into the ion beam. The electrons originate at a hollow cathode, similar to the main arc cathode, and pass through a plasma column or bridge connecting the neutralizer and ion beam. The voltage drop down this column is the "coupling voltage." This coupling voltage is generally proportional to the neutralizer keeper voltage. By maintaining a given keeper voltage, an adequate electron current is available for neutralization.

The present neutralizer servo-loop characteristics are shown in Fig. 17c. The nominal operating point is at $E_8 = 12.5$ V and $I_8 = 0.9$ A. The flowrate for this point, the neutralizer configuration of Fig. 2, is about 0.4 g/h. This represents about 4 to 8% of the total propellant flow at full- and half-beam power, respectively.

Variation of the neutralizer vaporizer operating point by $\pm25\%$ would produce a utilization efficiency change of ±0.35 to $\pm0.70\%$. Neutralizer tests are in progress to reduce the total propellant flow and the flowrate variation due to control-loop excursions.

Runaway. As indicated by the previous discussion of Fig. 3b, the thruster operating point can go out of the PC control range during startup or during transients. This runaway, for the present thruster, is generally characterized by low screen current, high accelerator current, and low arc voltage. These conditions cause the main vaporizer current to be at maximum and the cathode vaporizer current to be cut to minimum. Recovery back into the normal control range is not possible without shutting off the main vaporizer. Other thruster configurations can reach the runaway condition with both vaporizers at maximum current if the arc voltage is not a monotonic function of cathode flowrate. That is, the arc voltage may pass through a minimum and increase with higher or lower flowrates. In such case both vaporizers must be shut off. For the present thruster configuration, only the main vaporizer was shut off in the runaway condition.

Sensing of runaway is accomplished by comparing screen current and either accelerator current or arc voltage with the respective reference values. Initial tests used screen current and arc voltage. In steady-state operation, this scheme worked satisfactorily. However, during startup, slow thermal response of the cathode vaporizer allowed runaway with high arc voltage. Sensing of accelerator current was found to be a more satisfactory solution. Implementation of an automatic runaway recovery scheme was included in the SEPST III computer software.

d. BB-1M evaluation testing. A series of tests was performed to evaluate the basic PC characteristics, independent of integration problems. The results showed

capabilities, limitations, and general problem areas fundamental to transistor power conditioning. Efficiency, ripple, regulation, grounding, and cabling techniques (internal to PC and external) are significant in overall system design. However, each of these must be clearly defined to avoid substantial differences in interpretation.

PC efficiency. There are numerous definitions for "efficiency." The definitions relating to the present work are listed below.

Type 1, thermal efficiency, is based on heat dissipation: the ratio of PC output power to output power plus dissipation. In principle, the dissipation can be accurately measured in a calorimeter. The use of output power in both numerator and denominator reduces the effect of output-power measurement errors.

Type 2, average volt-ampere efficiency, is based on the ratio of average power in. In this case, the "average" is based on average-reading dc meters for dc input and output and on rms meters for ac outputs. If the ac component (ripple) imposed on the dc values is reasonably small, and if the ripple current and voltage are in phase (nonreactive), this average E-I efficiency is identical with that in type 1.

Type 3, effective volt-ampere unit efficiency, is based on the maximum required input volt-amperes, including ripple and average output power. This definition results from the fact that the power source must supply peak power, up to certain frequency limits, while thrust depends only upon average power. The difference between this efficiency and type 2 depends upon the input ripple frequency and the power-source (solar array) frequency response characteristics. In addition, the solar-array response depends upon power loading (Ref. 36). Near the maximum power point, ripple below about 50 kHz will affect the array. Thus, the "maximum required input" is the power the solar array must supply, including the amount of ripple to which the array responds.

Type 4, effective volt-ampere overall efficiency, is an extension of type 3 to include power dissipation in cabling and connections. In total system analyses, particularly mission calculations and solar-array sizing, a single efficiency (from array output to thruster input) is generally used. This value must obviously include any significant losses. Estimates indicate that a 1 to 2% power loss can be expected.

A series of efficiency measurements was made using precision dc meters. These were intended for PC evaluation as well as to establish a consistent method of measurement without a calorimeter. Initially, the PC full-power efficiency (type 2, above) was found to be 85.2% ±0.2% (67-V input at PC; output at test console, including 4 m of cable). The measurements were made with numerous calibrated instruments for comparison and included corrections for all line voltage drops. Since this efficiency was lower than expected, a more detailed study was conducted.

Since 80% of the PC power is conditioned by the screen supply, attention was focused on the screen modules. All individual inverter input lines were joined at the PC input connector. With the staggered phase technique, the peak-to-peak ripple current at this point was about 1.5%. The base drive power, 2 W (80-V input) to 5 W (53-V input) per inverter, was added to this input power. Using this technique, a screen system efficiency (with eight inverters operating) of 85.2% ±0.2% was measured at full power, with a 68-V input voltage.

Temperature measurements between the transistors on the mounting plate on each screen inverter were made. These ranged from 26.8 to 35.2°C with the mean temperature at about 31°C. The power transistors of the hottest inverter were replaced with a new matched set. The temperature on inverter dropped to 32.5°C and the screen system efficiency increased to 85.7% ±0.2% at 60-V input voltage.

Next, a pair of Transitron transistors (ST-18037), as used in the EX-1 and EX-2 units, were substituted for the existing Solitron transistors (SDT-8805). The substitution was made in the next hottest inverter (34°C). The plate temperature dropped to 28.3°C and the screen system efficiency increased to 86.4% ±0.2% with 60-V input. The efficiency improvements observed were associated with transistor matching, to minimize circulating currents, and with transistor switching speed, which reduced switching losses. (Solitron transistor SDT-8805 switching speeds are on the order of 1 to 1.5 μs while Transitron ST-18037 units are 0.5 to 0.7 μs.)

To further evaluate the effect of the Transitron transistors, the EX-1 screen system was installed in the BB-1M unit. The results of this testing are shown in Fig. 18 as a function of input voltage and percent of full pulse width. Despite the data scatter, the trends seem consistent.
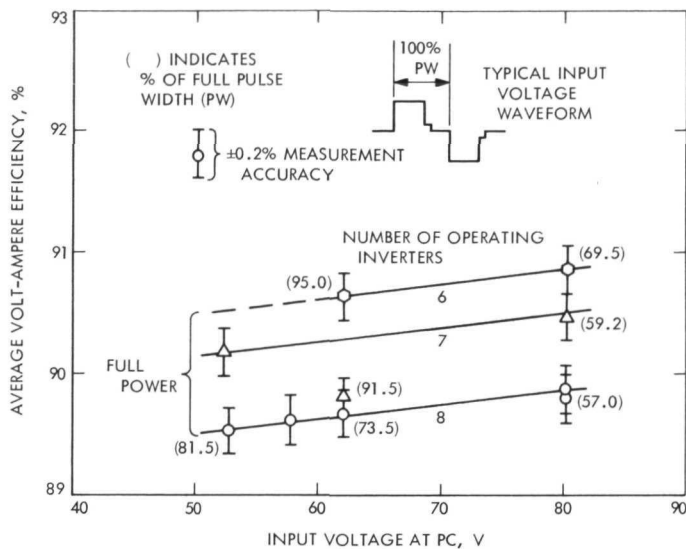
Fig. 18. Screen supply efficiency

Fig. 19. Input current and voltage ripples

Input ripple. Considering the previous efficiency discussion, the magnitude and frequency of the input ripple are important in overall system design. Measurements were made with an oscilloscope clamp-around current probe and a voltage probe. The current probe was limited to reading a fraction of the total current because the probe could not contain the normal 8-AWG input wire. The 8-AWG wire was parallel with a 14-AWG wire that would fit the current probe. For the ripple data, it was assumed that the ripple magnitude scaled directly with the dc-current level. The 14-AWG wire carried 17.35% of the total current.

Ripple current and voltage data for three test conditions are shown in Fig. 19. The oscilloscope was operated in the "chopped" mode. For PC full-power operation, using a laboratory power supply with an input of about 45 A at 64 V, the peak-to-peak current ripple is about 1.15 A at 10 kHz in Fig. 19a. If the solar-array voltage is assumed to remain constant with this ripple loading, the peak power demand increases by about 1.2%.

At full power with two screen inverters off, the ripple is as shown in Fig. 19b. In this case, the ripple current is about 1.73 A peak-to-peak at 20 kHz. This corresponds to a peak power increase of about 1.9%. The higher frequency is due to the effect of the staggered-phase screen system. Without the screen supply, but full power otherwise, the ripple is about 2.2 A peak-to-peak at 10 kHz in Fig. 19c. The final determination of the effect of ripple on overall system performance must await tests with a solar panel.

Output ripple. The output ripple of most interest is that on the screen, accelerator, and arc supplies. The principal limitations on the ripple magnitude arise from power-supply mutual interactions, servo-loop power-supply interactions, accelerator current disturbances, and propellant-utilization-efficiency variations.

Voltage ripple on the screen or accelerator supplies output induces a current ripple since the plasma-ion source is not completely emission-limited. The data of Fig. 20 indicate the typical situation. For a given ion-optics design, the total extraction voltage $(E_s + |E_6|)$ is chosen to draw a specified maximum beam current. Note that, for a constant arc current, the screen and accelerator currents vary with the total extraction voltage. If the total ripple $\Delta(E_s + |E_6|)$ is greater than the voltage margin, the ion beam is defocused on half the ripple cycle. This would result in significant accelerator current variations and a reduction in propellant-utilization

Fig. 20. Screen and accelerator current vs total extraction voltage

However, when combined with the peak-voltage ripple, the optics design is satisfactory.

The effect of the output ripple on servo-loop operation is not significant. The ripple frequency is several orders of magnitude greater than servo-loop time constants.

Regulation. Principally, two factors must be considered in determining regulation requirements (for input line and load changes): (1) system overall predictability for vehicle navigation, and (2) adequate total voltage margin as discussed in the previous section. In the first category, the parameters requiring accurate control are thrust $(I_5, E_5^{1/2})$, specific impulse $(E_5^{1/2}, \eta_m)$, and propellant utilization.

The servo loops were designed to maintain accurate control I_5 and η_m for constant E_5 and E_6. Considering the discussion of Fig. 20, a change in total voltage can result in a substantial change in η_m depending upon the magnitude of the ripple. However, assuming operation on the right-hand portion of the curves in Fig. 20, the equivalent slope is 0.45% utilization per 100 V at full power. Thus, to maintain an accuracy of 0.1% on η_m, the combined regulation of the PS5 and PS6 supplies must be better than 0.7%.

The percent regulation on E_5 is roughly double that needed on thrust and specific impulse. If the expected variation in η_m is 0.5% for 1% control on thrust and specific impulse, E_5 must be regulated to 1%. Regulation of about 0.4% (8 V for a 53- to 80-V input and 400- to 1000-mA load) was provided in the present PC design. Regulation of the accelerator supply was about 1%. The combined regulation tolerance produces a change of less than 0.2% in propellant-utilization efficiency. Thus, the regulation needed to satisfy vehicle navigation requirements on η_m appears to satisfy the total voltage margin requirement as well.

Weight. The BB-1/BB-1M model packaging was designed to closely simulate the experimental model packaging. With this approach, the BB-1M would indicate design weakness before the experimental models were completely built. The BB-1 weight was about 18 kg. With the modifications to form BB-1M, the weight was about 19 kg. A detailed breakdown for BB-1 and the experimental model is discussed in Subsection C-5-d.

5. Experimental Models EX-1 and EX-2. The EX-1 and EX-2 models were delivered in December 1970 and

efficiency. For the present thruster at full power, the margin is about 450 V.

Three sources of ripple on the arc output are available: (1) the supply-voltage ripple (into a resistive load), (2) an oscillation in the arc plasma, and (3) coupling with the screen and accelerator ripple. Of these, the second is presently most significant and can produce a peak-to-peak current ripple of about 50% of the dc level. This large ripple couples directly to the screen and accelerator current. The extent of this coupling depends largely upon the average propellant-utilization efficiency. If the peak ripple current cannot produce a large increase in screen current, as at high utilization, the effect will be relatively small. However, at utilizations below 85 to 90%, the arc ripple will be reflected in the screen current in direct proportion to the arc dc level.

At full power, the peak-screen-current ripple effectively reduces the total ion-extraction voltage $(E_5 + |E_6|)$ margin by moving the operating point to a higher level.

Fig. 21. Power conditioner experimental model (EX-1 and EX-2)

January 1971 respectively (Ref. 37). A photo of one of these units is shown in Fig. 21.

a. EX-1 and EX-2 configurations. The functional block diagram of the experimental system is the same as that shown in Fig. 10. It differs from the modified breadboard system only in the grouping of power supplies in module construction. The circuit mechanizations, while similar, have some notable differences that will be discussed below.

In the screen supply, in an effort to reduce losses and thereby increase efficiency, a number of changes were made. An additional line capacitor was used, a line choke with an energy return winding was added, capacitor turning was employed on the primary and secondary of the output transformer, and the output transformer was designed to take advantage of the reduced input-line-voltage swing. The ac coupling between the input control gates was removed since its inclusion was to protect the inverters during system development against accidents.

The 5-kHz inverter-output transformer was redesigned to provide drive directly to the two vaporizers at the output voltage since the vaporizer magamps are no longer in the primary but directly in series with the load. A winding was added to provide excitation to the magnet current sensor. Windings were provided to supply the high- and low-voltage segments of the keeper supply, which were previously derived from a separate transformer. The circuitry associated with the standby inverter was deleted and the ac coupling in the gating circuitry was removed.

The low-output power supplies in the low-voltage modulator were all repackaged to separate the supplies operating at ground potential and those floating at +2 kV or with remote transformers. The new low-voltage modulator contains the two vaporizer supplies, the neutralizer and cathode heaters, and the neutralizer keeper supply. The cathode heaters output is at +2 kV, and a remote transformer is employed so that no high voltage is present in the module.

The high-voltage modulator module contains the magnet supply and cathode-keeper supply. The magnet regulator is similar to the vaporizer circuit except that the magamp gate windings are separated and the drive signal is provided by a center-tap winding. The circuit thus forms a push-pull control circuit better known as a dc magamp. The cathode-keeper supply differs from the neutralizer-keeper supply in that the voltage telemetry is provided by a transformer that senses the ac provided for the low side of the output volt-ampere curve. The module is provided with its own drive transformer to easily facilitate high-voltage isolation. The transformer is driven from the collectors of the 5-kHz inverter.

Additional line capacitors were added to the arc inverter to reduce the capacitor losses.

The overall physical dimensions and mounting surfaces did not change from the breadboard configuration. The basic differences in the two unit types are in the frame design, choice of plate materials, choice of components and hardware, and component mounting techniques, all of which were changed to reduce weight (Subsection C-6).

Module placement was changed from the breadboard configuration to reduce wiring path lengths and thus weight. Figure 22 shows the module placement as seen from the nonradiating side. Solar-panel power is introduced at the low-voltage connection module and flows down the center of the unit branching out to the inverters. The position of the 5-kHz inverter allows low-power flow paths up the center of the unit to each using module.

The calorimeter results indicated that the expected increase of about 4% over the breadboard performance was probably experienced, but left in doubt the absolute value to within an uncertainty of ±1%. The experiment unit efficiency could probably be raised by ½ to ⅔ of 1% by lowering the overall system operating frequency by 10%. This is possible because operating frequency was about 10.5 kHz instead of the planned 10 kHz. The additional 500 Hz would not push the transformers into an unsafe region of operation. It is thus expected that the unit efficiency can be as high as 91%. The test results, summarized in Table 5, show that, at the present operating point, the power efficiency is 89.9% at 57.6 V input and 89.7% at 80 V input.

c. EX-1 and EX-2 electrical testing. Most all electrical testing of the experimental models was performed in conjunction with the final 1500-h SEPST III test. Thus, EX-1 and EX-2 electrical test results are all presented together in Section IV.

d. EX-1 and EX-2 weight summary. As indicated previously, the BB-1 design was intended as a "first cut" structural model as well as a circuit breadboard. Table 6 presents a summary by module or element to indicate the BB-1 and experimental model weights. Thus, the specific weight of the experimental models is about 4.9 kg/kW of input power (2.8 kW).

6. **Dynamic testing.** A power conditioning mockup (PCM) was used to simulate the experimental model PC for testing (Ref. 38). The PCM is shown in Fig. 23. Module masses indicated in parentheses in Fig. 22 are for the PCM, but the values shown are very nearly identical to those of the PC (Table 6).

The PCM was designed, constructed, and assembled to accurately simulate the PC with respect to its mass, center-of-mass, and construction techniques. This was achieved in the following ways:

(1) A spare frame, fabricated during the experimental model development program and identical in all significant respects to the one used in the PC, was used for the PCM.

(2) The PCM module plates were fabricated from AZ31B magnesium sheet having essentially the same modulus of elasticity as the magnesium used for the PC plates.

(3) Mocked components were carefully designed to accurately match those of the PC. Typically, the masses of the magnetics and brackets (and for other modules, some of the larger transistors, re-

1 CONTROL MODULE (498)	2 DIGITAL STAGGERED-PHASE GENERATOR (341)	3 LOW-VOLTAGE CONNECTION MODULE (116)	4 LINE REGULATOR (301)
5 SCREEN INVERTER 1 (597)	6 SCREEN INVERTER 2 (601)	7 SCREEN INVERTER 3 (601)	8 SCREEN INVERTER 4 (597)
9 SCREEN INVERTER 5 (608)	10 SCREEN INVERTER 6 (601)	11 SCREEN INVERTER 7 (600)	12 SCREEN INVERTER 8 (597)
13 LOW-VOLTAGE MAGNETICS MODULE (601)	14 5-kHz INVERTER (496)	15 ARC INVERTER (697)	16 ARC RECTIFIER FILTER (831)
17 HIGH-VOLTAGE MAGNETICS MODULE (500)	18 ACCELERATOR INVERTER (298)	19 ARC OUTPUT TRANSFORMER (706)	20 HIGH-VOLTAGE FILTER (561)

Vertical dimensions: 13.2, 24.0, 24.0, 16.3, 13.2
Horizontal dimensions: 18.8, 18.8, 18.8, 18.8

NOTES: DIMENSIONS ARE IN cm.
MODULE MASSES (IN PARENTHESES) ARE IN g.

Fig. 22. Module layout on experimental power conditioner (EX-1 and EX-2)

The harness was fabricated on a wiring jig and is tied along the top of the frame web as can be seen in Fig. 21.

b. EX-1 and EX-2 efficiency. An analysis of the experimental system efficiency is included in Ref. 37. This analysis was somewhat modified from the breadboard calculation in an attempt to account for increased losses due to the inductive switching envelope seen by the output-power transistors. The analysis used worst-case saturation voltages and switching speeds to determine the least efficiency expected. The analysis predicted an efficiency of about 91.5% at full power at all input voltages.

A test using a calorimeter at HAC was performed on EX-1 to measure the power lost when the unit was operating at full power (Ref. 34). Although there is some reservation as to the accuracy of the results, due to difficulties with the calorimeter, the results are interesting in that they confirmed the relatively constant efficiency at all input line voltages. However, the absolute values of efficiency were more consistent with the current-voltage measurements discussed in Subsection C-4.

Table 5. PC experimental model inverter and system efficiency test results[a]

Parameter	Line Voltage					
	53 V			80 V		
	Inverter frequency					
	5 kHz	7.5 kHz	10 kHz	5 kHz	7.5 kHz	10 kHz
Power dissipation per module, w/module						
Logic, drive, and filter circuits	6.8	6.4	8.3	6.4	6.5	6.05
Power transistors and composition diodes	4.1	5.1	5.2	5.0	5.9	7.8
Output transformers	↓	1.4	9.4	↓	7.6	8.0
Core loss	↓	–	2.7	↓	–	4.6
I^2R loss	4.1	–	6.7	5.0	–	3.4
Rectifier	10.1	3.3	2.3	11.2	4.4	4.4
Output filter	2.75	3.05	2.9	3.3	3.6	3.2
Total power dissipation (without output filter), W	21.0	22.2	25.2	21.95	24.4	26.25
Total power dissipation,W	23.75	25.25	28.1	25.25	28.0	27.45
Inverter efficiency (without output filter), %	92.3	91.85	90.9	92.0	91.1	90.5
Inverter efficiency using meters (without output filter), %	90.4	90.5	90.5	86.4	88.8	88.5
ΔEff ($Eff_{cal} - Eff_m$), %	1.9	1.35	0.4	5.6	2.3	2.0
Screen system efficiency using calorimeter data, %	92	91.55	90.5	91.6	90.8	90.2
Screen system efficiency using meter data, %	90.1	90.2	90.3	86.0	88.5	88.2

[a]Operation level = 250 V, 1 A, output 250 W.

sistors, and capacitors) were accurately known and mockup design was fairly straightforward. Mockup of the smaller components and much of the wiring was accomplished using pieces of metal plate or bar that simulated these components both in size and mass distribution.

(4) Attachment methods used throughout the PCM for components and assemblies closely simulated the methods used in the PC.

(5) The PCM was externally supported in the same way as the PC. In both frames there are 46 riveted nut plates spaced around the frame periphery for attaching the required structure support members. An additional attachment point common to both frames—a tapped 3.8-cm-(1.5-in.)-long cylindrical stem welded to the frame at the common corner of modules 6, 7, 10, and 11 (Fig. 22)—was also used.

The vibration loads one might expect at a power conditioner integrated in a SEP vehicle can be only estimated since at this time mission (launch vehicle) and vehicle configuration are not specified. However, sufficient information is available to allow reasonable estimates of these levels. In surveying preliminary configurations resulting from the JPL SEMMS study (Ref. 39)

and continued efforts since then, it was observed that the position and location of thrust subsystem elements relative to the launch-vehicle/space-vehicle interface are generally about the same in all configurations. Also, for most of the selected missions, the Titan IIID-Centaur appears to be the launch vehicle most likely to meet the mission constraints. Consequently, for this evaluation it was assumed that the launch environment to be simulated would be that of the Titan IIID-Centaur. Since the Viking Orbiter is to be launched by this particular vehicle, it was also assumed that the load analysis for the Orbiter was applicable to the SEP vehicle, i.e., the loads at the power conditioner can be approximated by those at similarly positioned assemblies in the Orbiter. Thus, the vibration test levels specified for these assemblies were used to define the vibration test spectrum for the PCM forced vibration test (Ref. 38).

As the first step in the test procedure, "modal" tests were performed to identify both the structure's natural frequencies and the wave shapes of the structure at these frequencies. The information from the modal tests was used to (1) verify the natural frequencies theoretically predicted in the initial design calculations, and hence give confidence in future design analyses; (2) determine which structural members would be most highly stressed in the forced vibration tests, and hence pinpoint areas

Table 6. PC mass summary

Module/component	Model BB-1[a] weights, g	EX-1, -2[b] weights, g
Control module	694	476
Staggered phase generator	499	314
Low-voltage connector	–	106
Line regulator	680	299
Screen (8 modules)	5,461	4,544
Low-voltage magnetic modulator	–	590
5-kHz inverter	590	465
Arc inverter	758	687
Arc rectifier	572	822
High-voltage magnetic modulator	–	498
Accelerator inverter	898	294
Arc output transformer	–	704
High-voltage filter	503	556
Cathode inverter	907	–
High-voltage module	581	–
Magnetic modulator	934	–
Limited use power supply	227	Included above
Remote transformers	–	Included above
Low-voltage plate and connector	136	–
Harness	1,560	738
Frame cover and screws	2,740	2,299
	17,740	13,593

[a]BB-1 = oxide-cathode breadboard.
[b]EX-1, -2 = experimental units 1 and 2.

Table 7. PCM low modal frequencies

Mode No.	Description	Modal frequency, Hz	
		Measured	Calculated
1	Bending	17.3	21.1
2	Bending	19.8	24.4
3	Torsion, bending	59.9	62.2
4	Plate mode	67.7	–
5	Torsion, bending	82.8	84.4
6	Plate mode	105.3	–
7	Plate mode	141.3	–
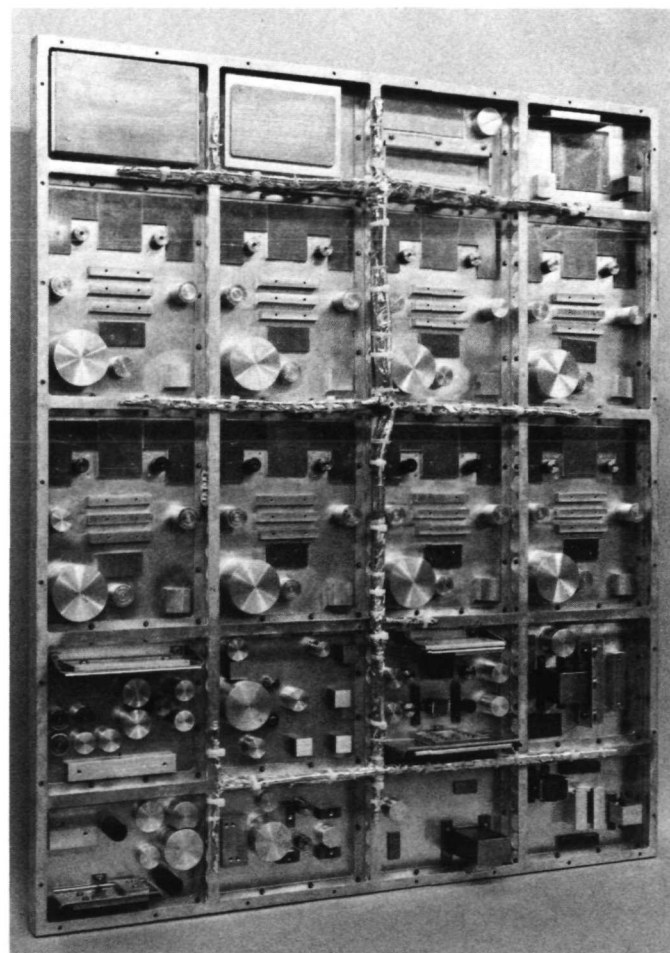
Fig. 23. Power conditioner mockup (PCM) (component side)

of major concern; and (3) properly locate (for the forced vibration test) the vibration measuring instruments at critical locations where maximum deflections should occur. Modal frequencies were surveyed over the range of 0 to 2000 Hz using both conventional and holographic interferometry techniques (Refs. 40 and 41). Details of the modal testing are contained in Ref. 38. The observed modal frequencies are shown in Table 7.

These results indicated that the structure apparently needed additional stiffening to qualify. However, it was necessary to proceed with the forced vibration tests to derive the data from which estimates of the penalties associated with making the structure qualify could be made.

The test setup for the forced vibration test is shown in Fig. 24 with the PCM mounted to a support fixture on a Ling 249 vibration exciter. In addition to being

supported around the periphery, the PCM is also supported at the stem within the periphery. Based on the modal tests, it was decided to use twenty accelerometers, one attached to the center of each module plate, to measure the PCM response to the input vibration levels. Data were recorded and stored on tape for post-test
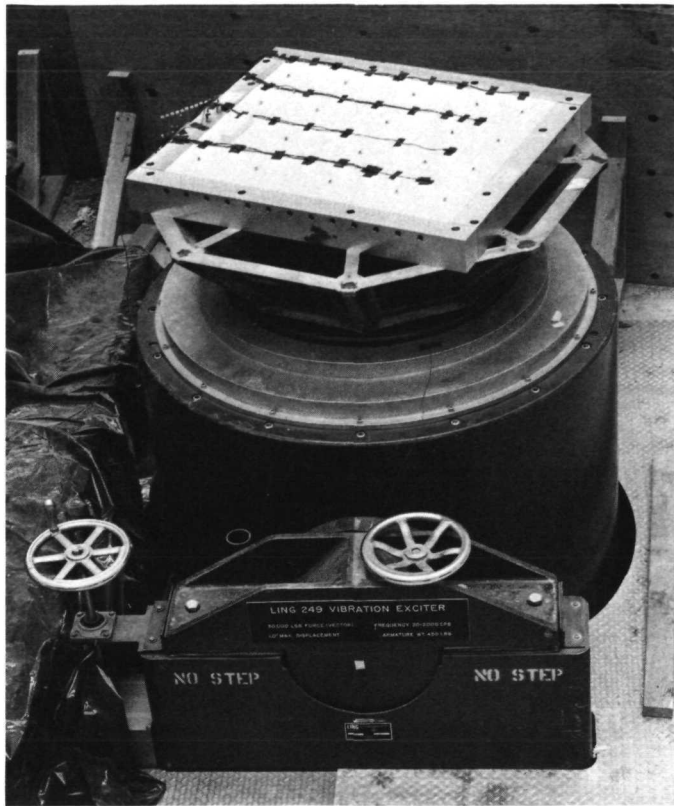
Fig. 24. PCM forced vibration test setup

Fig. 25. PCM integrity sweep (0.5 grms, 10 to 2000 Hz) response
data: (a) Module 1; (b) Module 10; (c) Module 14

reduction. A printout of real-time response data for six selected modules was provided for monitoring the test. In addition, the PCM was observed visually during the tests.

Rather than subject the PCM to the maximum specified vibration levels (Ref. 38) at the onset of the test, three intermediate low-level sinusoidal sweeps were scheduled. Prior to the first sweep, a constant 0.5-Grms, 10- to 2000-Hz "integrity sweep," the instrumentation was adjusted so that the accelerometers during the test sweeps could be estimated. At the conclusion of the integrity sweep the instrumentation was adjusted so that the accelerometers would measure within their optimum range and the first test sweep carried out. During this first test sweep, the responses of the PCM modules as observed both visually and from the printout data were considered to be excessive. For this reason it was decided not to continue with the higher level sweeps. With this termination of the forced vibration tests, the power conditioner structural evaluation was concluded. An instrumentation problem unfortunately made the first test level data unusable. However, the integrity-sweep data were adequate for a proper test evaluation and representative

plots of these data after having been passed through a narrow-bandwidth filter are shown in Fig. 25. It was necessary to filter the noise out of the original data to obtain meaningful responses at the lower frequencies

(10 to 100 Hz). From the plots in Fig. 25, the significant responses were extracted and used to calculate the zero-to-peak accelerations and displacements. These calculated responses are shown in Table 8.

Assuming reasonably accurate structural simulation between the PC and PCM, it can be generally concluded from the results of this evaluation that without some additional stiffening the present PC structural design is not adequate to withstand the launch-imposed vibration loads. Only the forced vibration test results could confirm this conclusion, but it was somewhat predictable from the modal test results. For example, inspection of the low-frequency vibration mode shapes indicated that

Table 8. Response of PCM modules to 0.5-Grms sinusoidal sweep, 10 to 2000 Hz

Module-1 response				
Response point, Fig. 25(a)	Frequency, Hz	Acceleration G(0-peak)	Displacement (0-peak)	
			cm	in.
(a)	60	2.4	0.017	0.007
(b)	160	2.7	0.003	0.001
(c)	210	2.7	0.001	0.0005
(d)	280	13.9	0.005	0.002
(e)	340	9.9	0.003	0.001
(f)	630	26.9	0.001	0.0005

Module-10 response				
Response point, Fig. 25(b)	Frequency, Hz	Acceleration G(0-peak)	Displacement (0-peak)	
			cm	in.
(a)	15	1.56	0.178	0.070
(b)	67	7.35	0.042	0.017
(c)	80	7.35	0.029	0.012
(d)	87	7.35	0.024	0.009
(e)	100	8.65	–	–
(f)	175	8.65	–	–

Module-14 response				
Response point, Fig. 25(c)	Frequency, Hz	Acceleration G(0-peak)	Displacement (0-peak)	
			cm	in.
(a)	70	14.1	0.070	0.028
(b)	76	38.2	0.165	0.065
(c)	81	32.6	0.127	0.050
(d)	145	7.8	0.009	0.004
(e)	650	10.2	–	–
(f)	900	19.8	–	–

the frame should probably be stiffer. This was confirmed by the high-frequency modal test when it was observed that the frame and plates seemed to vibrate as an integral unit. In addition, this test showed that the masses of the individual components attached to the plates determined the vibrational modes at the plates, thereby indicating that the plates should b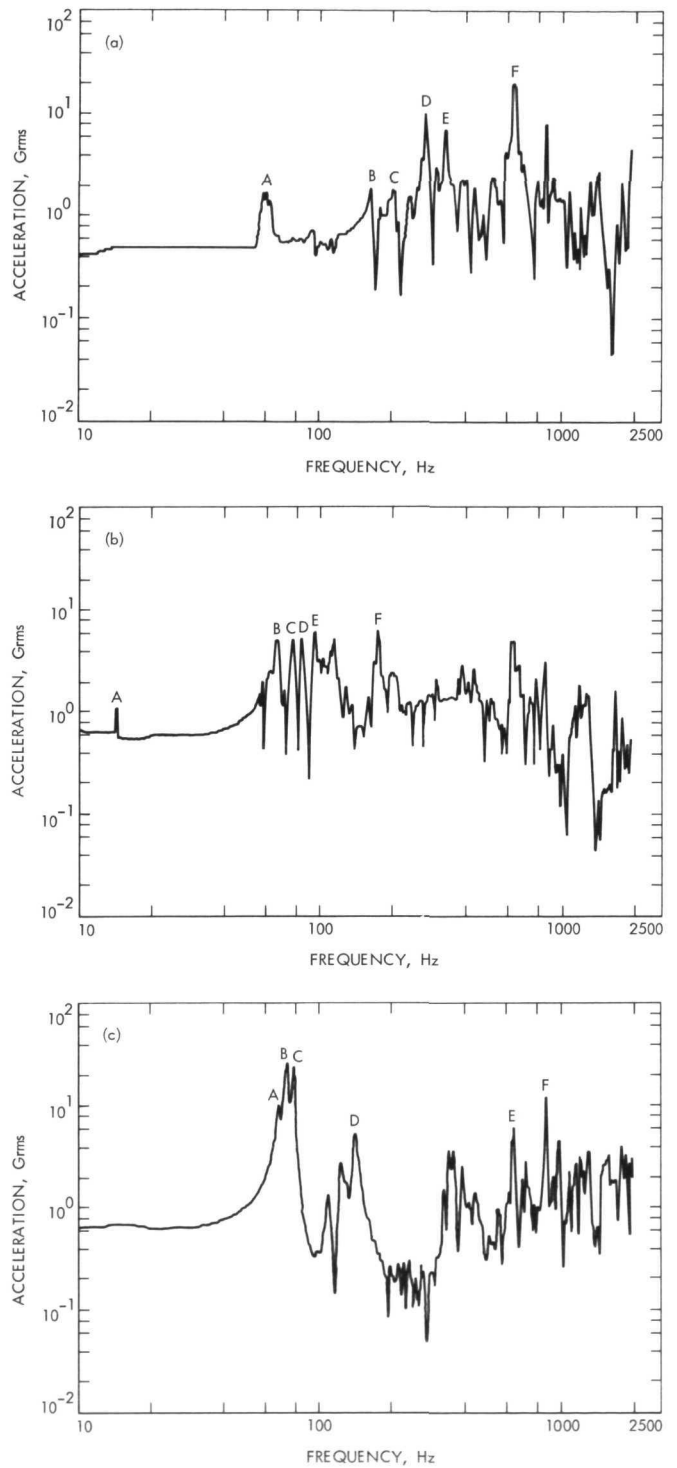e stiffened. The results of the forced vibration test reinforced these conclusions, i.e., the frame should be stiffened to minimize the low-frequency deflections, and that both the frame and plates probably would require stiffening to minimize the high-frequency acceleration responses.

Estimates of the weight penalties associated with making the presently configured PC structure qualify for launch were made. Assuming that the flat-plate geometry is retained, then the additional mass needed to stiffen the PC to minimize the low-frequency deflections would probably be no more than about 835 g, i.e., 30% of the PC structure mass (0.84 kg) or about 7% increase in total PC mass.

D. Switching Matrix

As a portion of TSS technology development, a switching matrix (see Fig. 1) was built. The ultimate decision to use this element depends upon the reliability of the thrusters and power conditioners. When system reliability with the added complexity of the switches exceeds the reliability of the noninterchangeable thruster-PC system, switching is advantageous. The tradeoff of switch weight against additional PC units is of second order relative to reliability considerations. The present use of switches does not imply a firm requirement for future systems. However, considering the desirability of failure detection (i.e., PC or thruster failure), switching a PC between its thruster and dummy loads would be a minimum requirement. The switching matrix (SMX) includes switches, a logic module, and a cabling interface.

1. **Switch.** Two types of switches were investigated: mechanical and solid state. Solid-state switching (using thyristors) is undesirable because of high losses of the thyristors and the lower reliability due to a high parts count and complex control circuitry (Ref. 42). The weight of both types of switching appears to be comparable. The mechanical stepping-type switches used in the present program (Tech Laboratories, Inc., Type 800) have been discussed previously. However, the individual switches have been hermetically sealed for operation in vacuum. Commercially available switches presently em-

ployed require the use of two units per PC. A typical hermetically sealed switch is shown in Fig. 26. Each switch has four decks with two wipers per deck. Each wiper can be connected to one of six positions. Thus, up to five thrusters can be accommodated with one position for a dummy load. The stepper motors require 28-V dc power. Each switch weighs about 1 kg or 2 kg per PC. It is expected that a redesigned flight-type switch for one PC would weigh about 1.5 kg.

2. Logic. The logic module required to actuate the switch, to determine switch position, and to prevent incorrect connections, is presently an individual unit. This unit could be incorporated into the space vehicle computer (CCS) in a flight system. The logic module is connected to a manual control and display panel (MCDP) and to the SEPST III computer. In manual operation, push buttons are used for initiating commands. In closed-loop operation, the computer sends commands to the logic directly, with the interconnection results displayed on the MCDP. The weight associated with the present logic

module is about 10 kg (Ref. 43). Flight packaging should reduce this weight to 5 kg.

To minimize weight, switching can occur only with power off (requiring all thrusters to be shut off during switching). Since cold thrusters (those not on prior to switching) require on the order of an hour to reach full power, the thrust distribution may be nonsymmetrical for a period of time. This effect must be considered by the TVC system designer.

3. Cabling interface. Each switch has sets of outputs corresponding to each thruster or dummy load. Switch terminals of the same type (e.g., arc $(+)$) are connected together on or near the switches. This eliminates the need for cable runs from every switch to each thruster (i.e., only one set of cables is required per thruster).

In addition, an interface must be provided for connecting the PCs to the switches. The SMX and the associated cabling interfaces are shown in Fig. 27. The ring
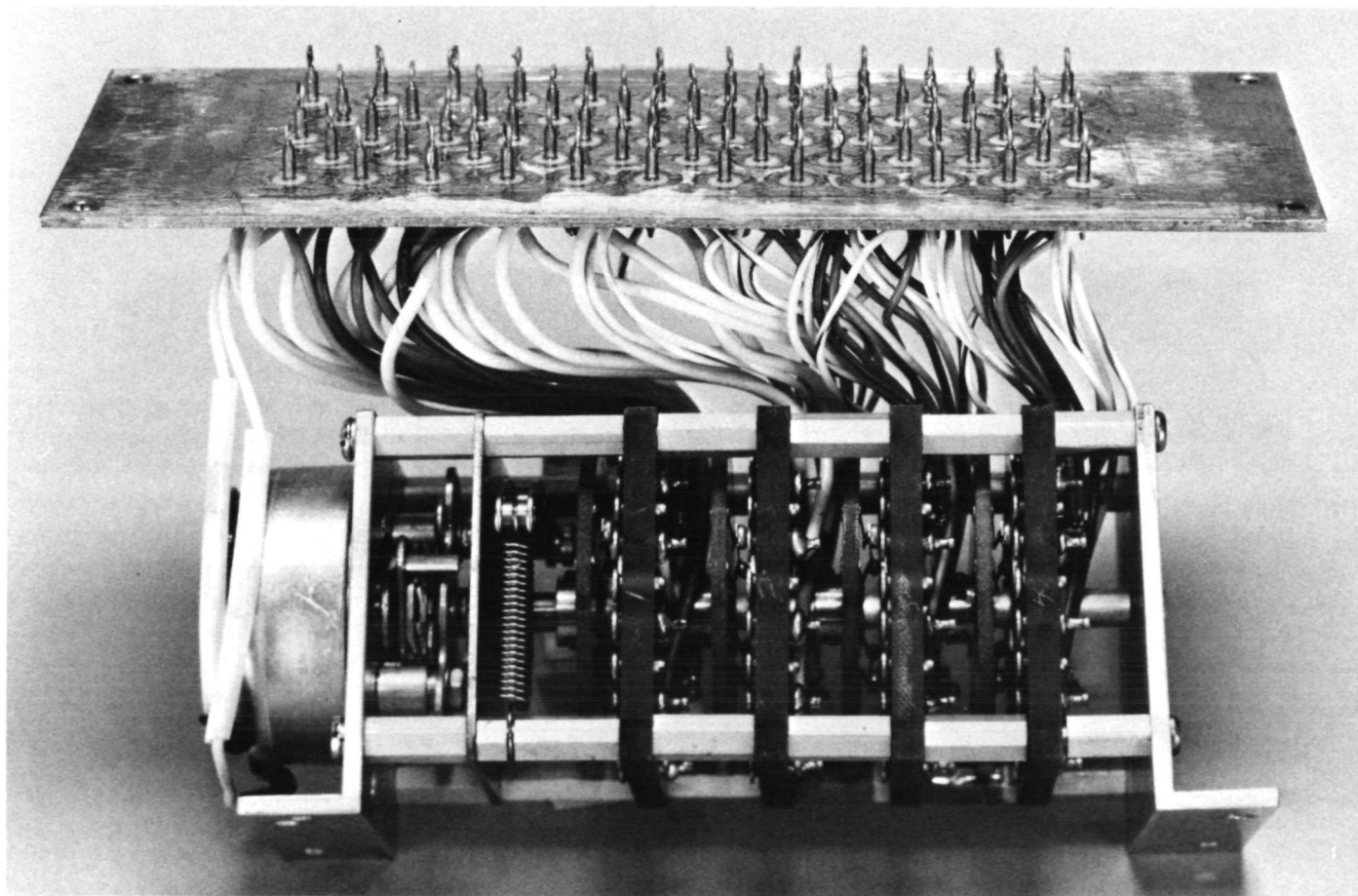

Fig. 26. Switch wired to header plate
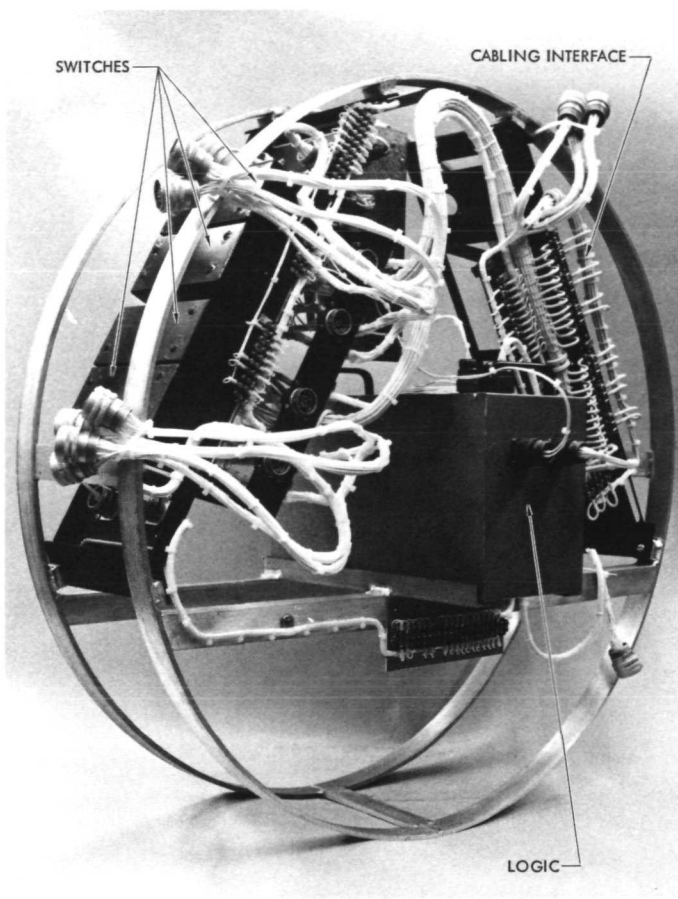
Fig. 27. Switching matrix assembly

in which the SMX is mounted fits inside a vacuum chamber spool. The loose cables attach to "bulkhead"-type feed-through connectors inside the spool. The SEPST III test set up is discussed in more detail in Section III.

E. Thrust Vector Control Mechanism

1. General. On vehicles using SEP, the thrust vector control (TVC) element will provide normal attitude control and will correct for thrust vector misalignment and vehicle CG changes due to propellant depletion. In general, three-axis control is required for this purpose. If out-of-plane forces can be accepted and control about all axes is not required simultaneously, two-axis gimballing may suffice. Many mechanization schemes have been proposed. These fall into two basic categories: (1) direct ion-beam vectoring by electrostatic deflection, translation of the accelerator/screen grid, or multiple-axis thruster gimballing; and (b) mechanical translation of the entire thruster array, combined with single-axis gimballing.

All methods in the first category are capable of providing control if two-axis beam vectoring, through a sufficiently large angle, is acceptable. Research on electrostatic and grid translation is presently in progress at HAC (Ref. 21) under contract and at NASA-LeRC. Further development is required before these concepts are ready for flight application. Two-axis gimballing does not appear to be difficult, although relatively large deflections would be required for a multithruster system. TRW, Inc., has proposed a system in which all thrusters are gimballed by means of a "wobble plate." This technique is in the preliminary design phase at present (Ref. 44).

The principal limitation on two-axis gimballing, out-of-plane forces, has resulted in the secondary category of TVC-mechanization schemes. If gimballing is limited to one axis, the remaining two axes can be controlled by translation of the thruster array. Such a technique has been implemented in the present program (Ref. 45). Previous studies have shown that this use of primary thrust for attitude control, accounting for the weight of the three-axis mechanism, results in a lighter weight system than one using cold gas.

Translation and gimballing requirements were initially based on the JPL Jupiter mission study (Ref. 46), but the more recent studies indicate similar requirements. A life requirement of 5,000 to 10,000 h places a significant constraint on actuator design. Stepper motors typically used to drive the actuators are believed to have life expectancies in the 10^8- to 10^9-step range. For the expected limit-cycle operation with a period of about 1 min., 10,000 h of operation would require about 10^6 corrections, with the assumption of a single-step deadband width and no backlash between input and output. Including the capability to correct for a few large disturbances requiring full translation or gimballing and to perform ground testing, the life requirements are in the 10^7-step range. However, the step requirements increase substantially if the limit-cycle deadband width is greater than one step.

The uncertainty in stepper-motor life at the present time has led to a conservative actuator design, i.e., a design with low backlash to conserve steps in the limit-cycle operating mode. Such a design, in near flight-ready form, is described in the following sections. The design includes consideration of launch loads, high-vacuum operation, positioning accuracy, reliability, weight, thermal loads, wiring and propellant line flexibility, con-

tamination by ion-beam-sputtered material, and testing in a 1-G environment.

2. Design requirements. The portion of the TVC subsystem described in this section includes the following items (Ref. 45):

(1) Gimbal actuators (one per vectored engine).

(2) Translation actuators (one for each of two perpendicular axes).

(3) Thruster array structure (to support the actuators, thrusters, propellant lines, and electrical cabling).

(4) Propellant lines and electrical cabling.

The TVC drive electronics, for both open- and closed-loop testing, are discussed in Subsection F.

The design requirements were taken principally from the Jupiter flyby mission study performed at JPL (Ref. 46). The requirements for the translation and gimbal actuators are listed in Table 9. The array maximum travel for both actuators is based on the five-thruster (20-cm-diam) array (Fig. 12). The translation axes are aligned with the sides of an imaginary square formed by the four outside thrusters. The output travel of ±33 cm allows any thruster to translate about half a thruster diameter past center. Two gimbal axes are provided along the diagonals. The vehicle configuration used requires ±10-deg thruster gimballing. Actuator torque is chosen to meet expected requirements for SEP systems up to 20 kW.

Table 9. Actuator requirements

Parameter	Translator actuator	Gimbal actuator
Output travel	±33 cm	±10 deg
Output torque (at zero speed), Nm	40	4.5
Slewing rate	0.63 cm/s	10 mrad/s
Maximum stepping rate, steps/s	100	
Resolution	6.3×10^{-3} cm	1×10^{-4} rad

The slewing rate, stepping rate, and step size (resolution) are determined jointly. To a first order approximation, the required time response of the vehicle to a large disturbance determines the maximum slewing rate. The values chosen (0.63 cm/s and 10 mrad/s) appear to be consistent with the requirements for vehicles in the 5- to 20-kW power range. The step resolution must consider limit-cycle operation as well as the maximum
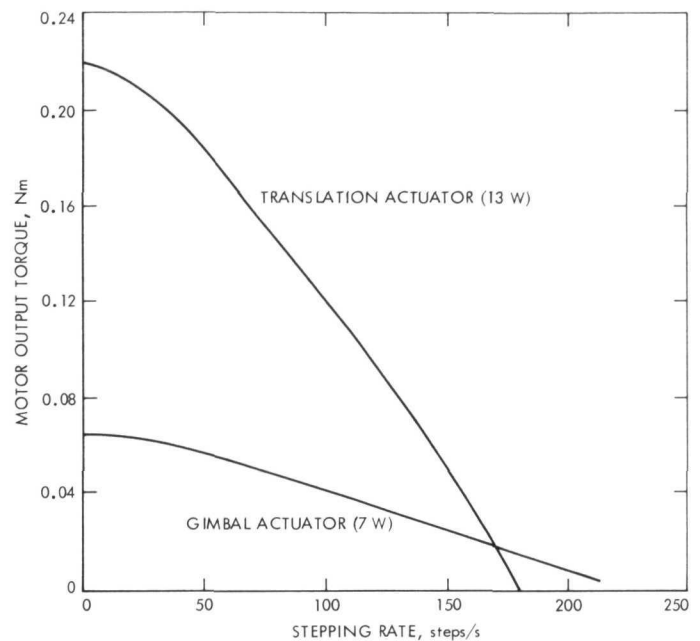
Fig. 28. Stepper-motor torque as a function of sweeping rate

stepping rate available. As shown in Fig. 28, the torque output of the stepper motor is dependent on stepping rate. For a given torque at the actuator output, with the output resolution and slewing rate specified and with the friction losses in bearings and seals estimated, the motor size can be determined. To apply small stepper motors and yet provide a design margin, the maximum stepping rate is limited to about 100 steps/s. Slewing rate and motor-stepping rate determine the gear train reduction required.

3. Detail design.

a. Gimbal actuator. In actuator design, a tradeoff must be made between friction losses, wear, torque, power, and backlash. With a straight spur-gear reduction system, the low amount of backlash must be accepted in the last gear stage (1 to 2 mrad) for low wear (long life) and reasonable power. This minimum backlash represents 10 to 20 steps with the resolution specified in Table 9. To reduce this value to less than one step requires the last reduction stage to have a backlash of less than 0.1 mrad. As shown in Fig. 29, this minimization of backlash is accomplished for the gimbal actuator by use of a high-tolerance lead screw (6.3 threads/cm) and saddle-nut configuration. The saddle nut is attached to the output sector by means of a split strap. The strap can be tensioned to provide a zero backlash coupling. The bearings supporting the lead screw are preloaded to remove backlash.
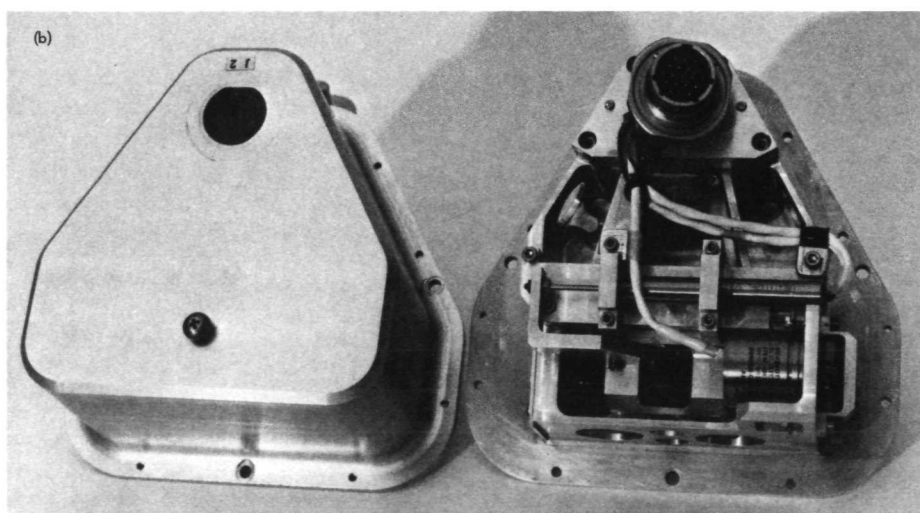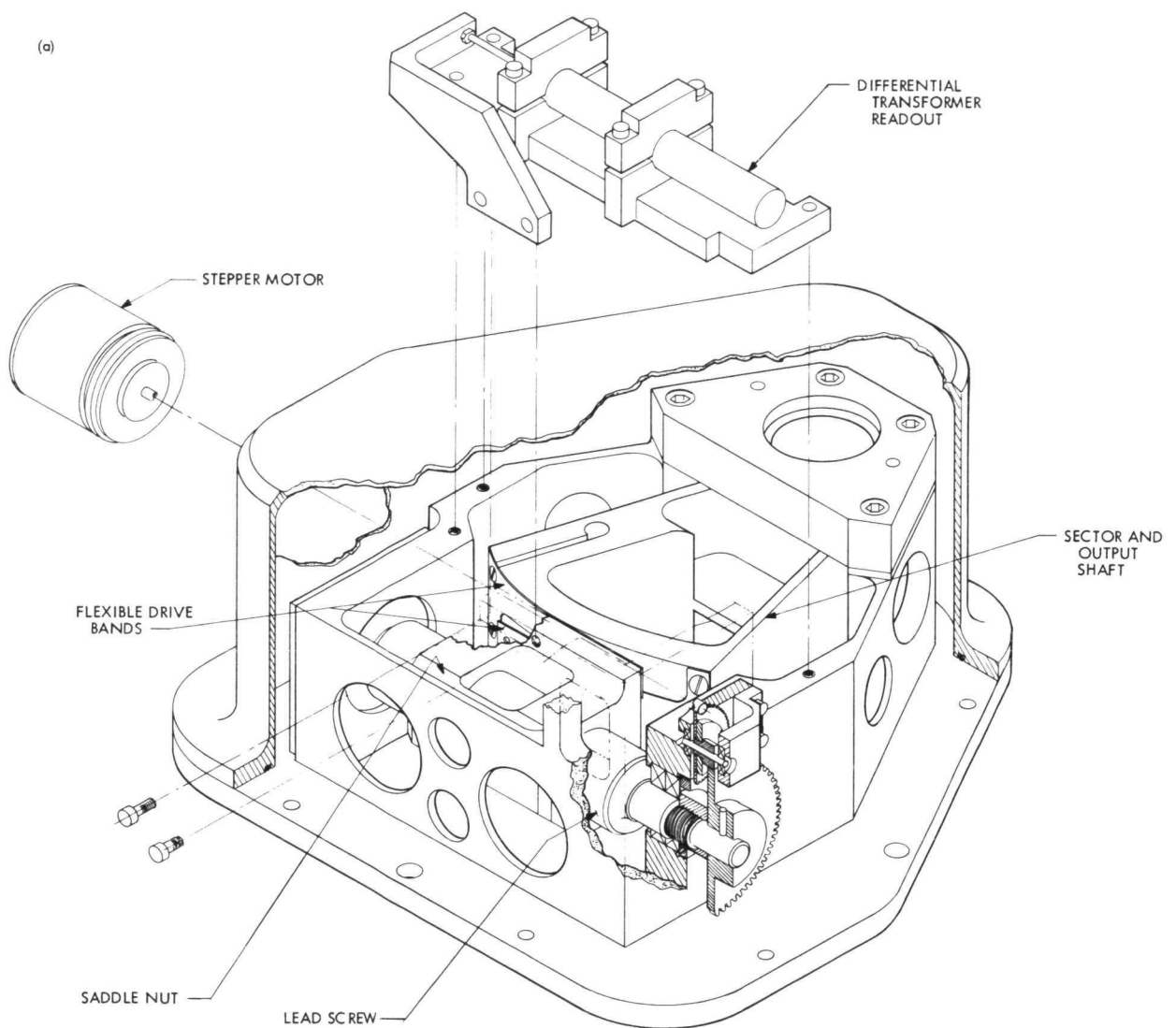
Fig. 29. Gimbal actuator: (a) exploded view; (b) gimbal actuator assembly

The three spur-gear stages from the motor to the lead screw provide 50-to-1 reduction. Thus, one step of the 90-deg (1.57-rad), size-11 stepper motor produces about 31.4 mrad of lead screw rotation or about 0.8×10^{-4} cm of saddle-nut translation. This step results in the output shaft rotation of about 0.1 mrad/step. Thus, the lead-screw and saddle-nut stage provides a reduction of about 314 to 1, which reduces (by this ratio) the total spur gear backlash. The backlash remaining results from clearance between the lead screw and saddle nut. This clearance must be less than 0.8×10^{-4} cm for the output to move on the first step. Clearances of less than this value can be obtained without substantial friction losses by lap matching the lead-screw and saddle-nut combination during assembly.

The position pickoff is a linear variable differential transformer (LVDT) that senses lead-screw position. A solid rod connects the saddle nut to the LVDT. Because there is essentially zero backlash between the pickoff and the output, testing of the actuator is simplified. The output shaft, vacuum-sealed with two O-rings, is clamped to the thruster gimbal shaft. An insulating spacer is used in the coupling to reduce heat transfer from the thruster. Spherical, self-aligning bearings in pillow blocks are used for mounting the thrusters to the array structure. The actuator case is an O-ring sealed unit and is pressurized to 5 psig with a 90% nitrogen, 10% helium mixture. Hermetic sealing is required for lubricant protection during long-term operation in space vacuum. In the packaging concept of the present unit, the entire gear assembly, including the output shaft, is supported on the base, which allows testing with the cover removed.

All metal parts of the actuator, except the split strap, are aluminum to minimize thermal expansion differences. The lead screw is a hollow shaft, hand-anodized after machining. The present actuator mass is 1.7 kg with an expected flight mass of about 1.5 kg.

b. *Translator actuator.* To obtain low backlash in the translator actuator, which is illustrated in Fig. 30, a harmonic drive unit is used as the final reduction stage (100 to 1). The basic characteristic of the harmonic drive, with minimum gear tooth friction, allows low backlash (less than 2.5×10^{-5} rad) without high friction or wear. The reduction between the stepper motor and the harmonic drive is 28.3 to 1. The total 2830-to-1 reduction produces a rotation of the output drum of 0.55 mrad per step.

A size 15, 90-deg stepper motor is used for the actuator drive. A rotary, infinite-resolution potentiometer is con-

nected to the output by means of a spring-loaded gear for position readout. As noted for the gimbal actuator, most parts of the translator actuator are aluminum to minimize thermal expansion problems. The present unit has a mass of 2.7 kg with an expected flight mass of about 2.5 kg.

A beryllium-copper split flat strap converts the actuator output drum rotary motion into linear motion of the structure, as shown in Fig. 31. The strap loops the drum and is attached to eliminate slippage. Rotation of the drum causes the strap loop to move relative to the strap ends, which results in the translation of the array.

c. *Thruster array structure and translators.* The thrusters, gimbal actuators, cabling, feedline, and rails for one translator axis are attached to the thruster array structure. The translator actuators and the bearings for both axes are housed in an intermediate carriage (Fig. 31). Thus, the carriage and array structure together translate along one axis, while the array alone translates along the second axis. Two translator rails per axis are used. These rails are solid 3.2-cm-diam stainless steel rods in the present assembly. However, beryllium tubes are proposed for flight application. The translator bearings, which are linear recirculating ball bushings, are press-fitted into the carriage structure. The completed assembly is shown in Fig. 12. For laboratory tests, the vertical axis is counterbalanced because, in space, the translator actuator is not required to lift the array weight. The lead counterweights fit within the vacuum header-array support structure (inside square tubing shown in Fig. 12). The array structure is constructed primarily of aluminum sheet with riveted joints. As shown in Fig. 12, the array could support five thrusters, although fewer are presently used for simplicity. (A third thruster was added as a spare for final system testing.)

The requirement for caging the translation system during launch was investigated analytically. The natural frequency of an equivalent spring mass system was computed, as shown in Fig. 32, for stainless steel and beryllium rods. Generally, a natural frequency above 20 Hz is required for vehicle compatibility. The results in Fig. 32 indicate that caging is required for both materials with any wall thickness.

d. *Cabling and propellant lines.* Cabling, which includes requirements for high voltage (a few kV), high current (up to 10 A), and low-noise pickup, must span the two-axis translator as well as the gimbal interface. To meet these requirements with proven space-vehicle-compatible materials, Teflon- (TFE-) insulated ribbon cable was

(a)

DRUM

FLEXIBLE DRIVE
BAND

OUTPUT SHAFT

ANTI-BACKLASH
GEAR

STEPPER
MOTOR

HARMONIC DRIVE
FLEX SPLINE

HARMONIC DRIVE
FIXED SPLINE

FILL SCREW

BEARING SUPPORT

POTENTIOMETER

HARMONIC DRIVE
WAVE GENERATOR

(b)
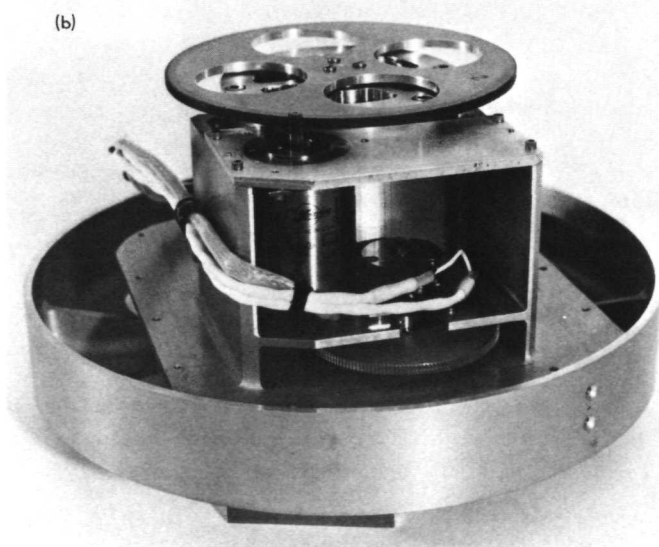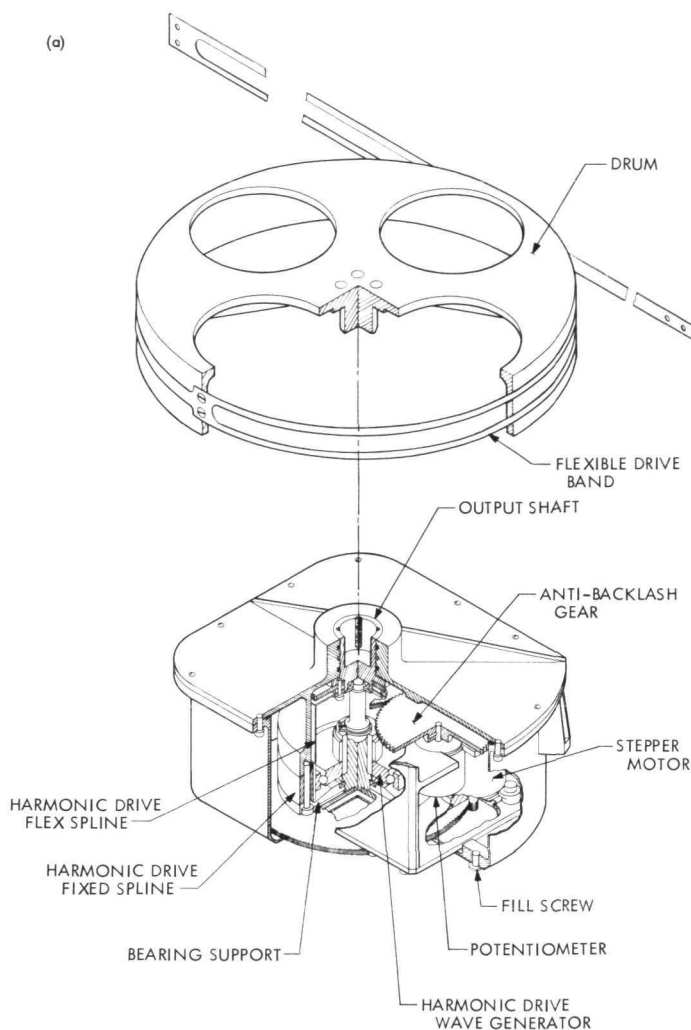
Fig. 30. Translator actuator: (a) exploded view;
(b) translator actuator assembly
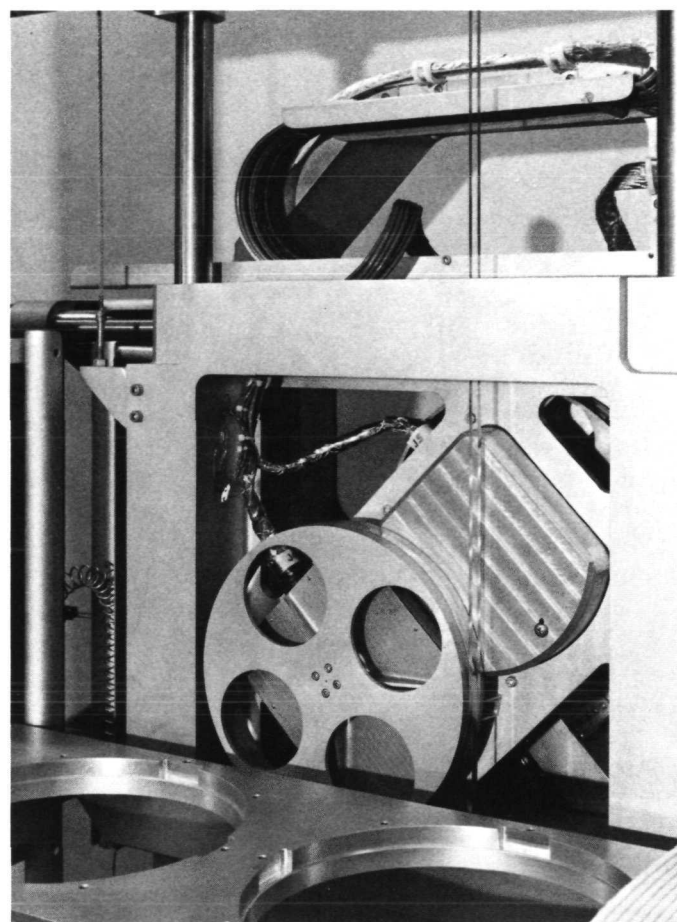
Fig. 31. Translator actuator output drum and drive strap

selected. A total of four cables are used with two for the thruster and two for the actuators. The thruster high-current (up to 10 A, floating at $+2kV$) requirements are met with four 19-strand 20-AWG conductors in parallel. The four conductors are insulated together. Nine of these sets are bonded into ribbon form with another layer of Teflon. The remaining nine thruster low-current requirements (including potentials of $+2kV$, $-1kV$, and ground) are met with 19-strand 20-AWG single conductors bonded in ribbon form. The actuators require twisted-shielded pairs and triads for minimum electromagnetic interference. A cable of pairs and triads, with braided shielding and 28-AWG conductors, is used. Each ribbon is about 6-cm wide.

The four ribbon cables are stacked and formed into an open loop. Beginning at an attachment point on the array, the first loop lies in a horizontal tray attached to the carriage as shown in Fig. 31. Thus, the loop "rolls" in this tray as the array moves relative to the carriage. The cables are then bent 90 deg to form a second loop
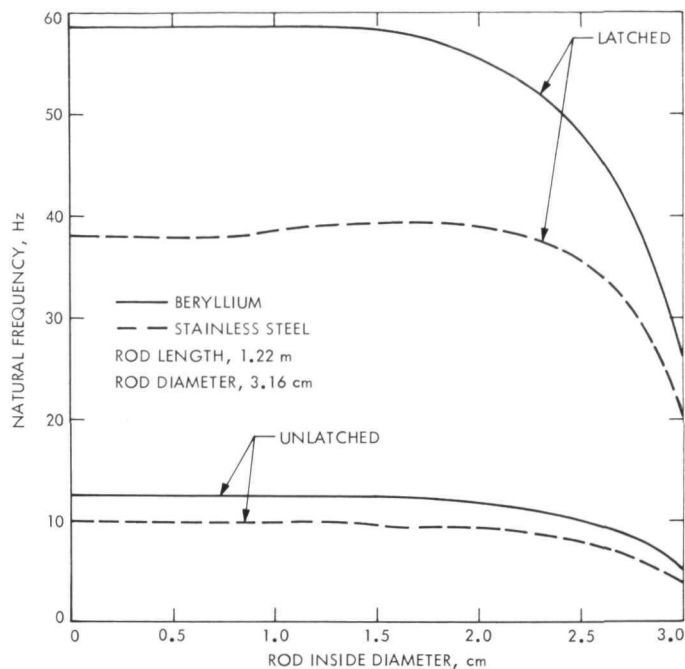
Fig. 32. Natural frequency of equivalent spring mass system of the translator rods comparing latched and unlatched configurations (natural frequency above 20 Hz is required for S/C compatibility)

along the vertical axis as in Fig. 33. Supported by trays on the carriage and mounting structure, this loop crosses the second axis. This design results in a low total loop (4 cables) rolling force of about 5 to 6 N. On the carriage, the actuator cables are split for operation of the translator actuators. On the array, all of the cables are split and distributed as required. The combined mass of the four ribbons is about 4 kg (1.12 kg/m).

The propellant feedline crosses the translator in a rolling loop design similar to that for the cabling. Fully hardened 0.157-cm-diam stainless steel tubing is first formed into a 1.9-cm-diam spring-type coil. This coil is formed into an open loop and is supported in small hemispherical trays on the array, carriage, and system mounting structure, as shown in Fig. 34. As with the cabling, the feedline loop requires only a rolling or driving force to overcome side friction with the tray. Separate coils (3 m long each) are used for each axis with a junction on the carriage. Single lines are run for each thruster from the distribution point on the array. The cabling and feedline configuration is designed so that minimum redesign would be required for flight application.

e. Actuator performance testing. The open-loop electronics console used for testing provided actuator drive
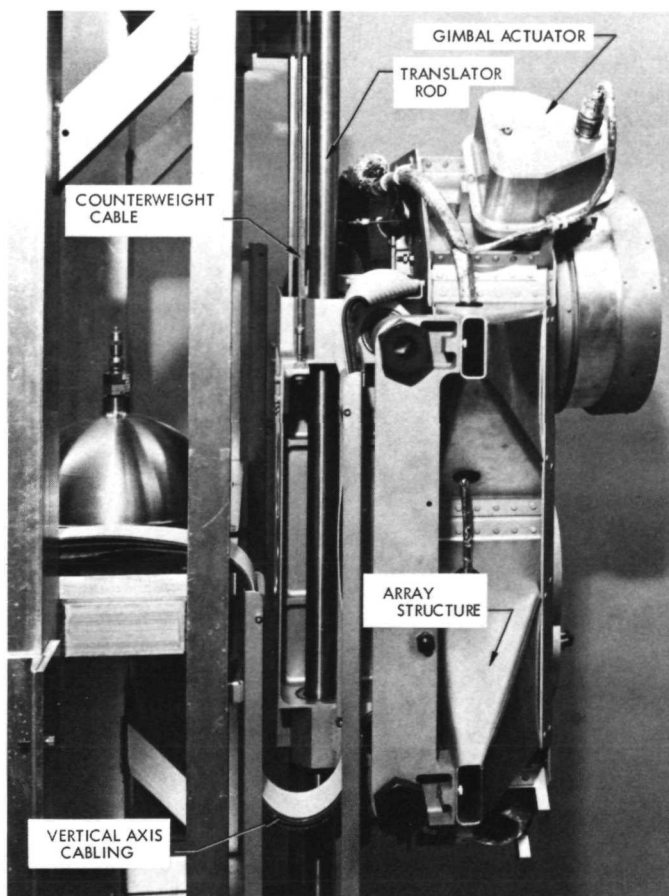
Fig. 33. Translator side view showing the flexible cable interface across the translator
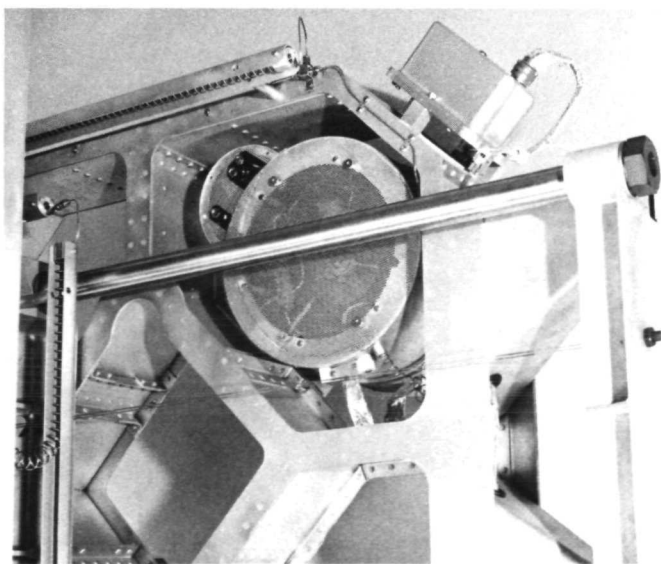
Fig. 34. Back view of translator showing how propellant feed line crosses translator interface
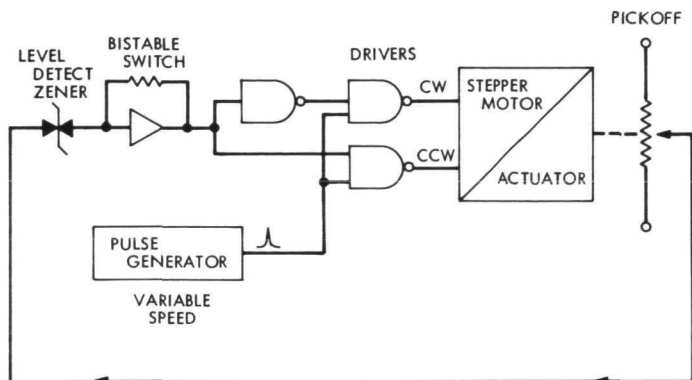
Fig. 35. Open-loop TVC electronics

Fig. 36. Translator actuator torque as a function
of stepping rate
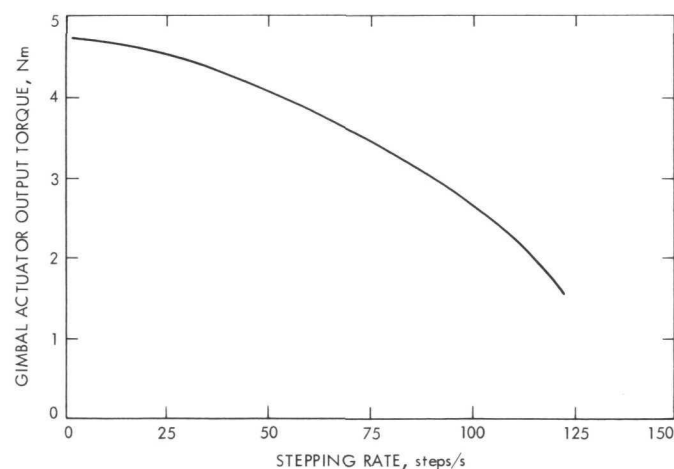
Fig. 37. Gimbal actuator torque as a function
of stepping rate

and instrumentation (position and stepping rate). A simplified block diagram for a single-axis actuator control is shown in Fig. 35. The test console had provision for controlling six actuators simultaneously. Three variable-speed pulse generators activated the stepper motors at speeds of from 3 pulses/s to greater than 100 pulses/s. Other features of the test console that were useful in the evaluation and testing of the actuators are listed below:

(1) Automatic drive polarity reversal as the actuator approached its stops (adjustable for each control loop).

(2) Individual control of each actuator tested, including start and stop, single-pulse actuation, and variable speed.

(3) Meter indications to show the angular positions of each actuator.

(4) Digital voltmeter readout of both the actuator position potentiometer and LVDT.

The following component performance bench tests were made on the gimbal and translator actuators before system assembly:

(1) Output torque vs input speed.

(2) Output torque vs angle (gimbal actuator only).

(3) Backlash measurements.

(4) Leak rate measurements.

(5) Translator draw-bar pull test.

Curves of output torque vs stepping rate were taken for the actuators by adapting a torque wrench to the output shaft. The curve for the translator actuator, shown in Fig. 36, indicates a zero-speed stall torque of approxi-

mately 40 Nm. The data for the gimbal actuator, shown in Fig. 37, indicate a zero-speed stall torque of approximately 4.5 Nm. The gimbal actuator output torque vs output angle of rotation was measured to ensure proper tensioning of the sector straps. The results of this test, shown in Fig. 38, indicate that proper strap tension
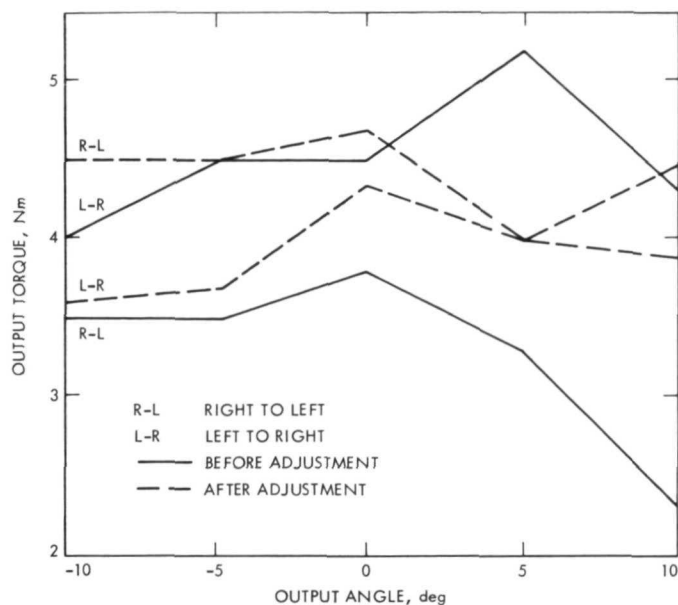
Fig. 38. Comparison of gimbal actuator output torque as a function of output angle indicating necessity of adjusting sector straps

adjustment is necessary to ensure equal torque output in both directions of rotation for all angles and to obtain the maximum torque output.

Backlash was measured for the translator actuator by mechanically attaching a dial indicator to the output shaft to measure the amount of travel per step. The actuator was stepped in one direction and then the other, with position readings taken through the reversal. The backlash was measured to be approximately one-half step. Similar measurements on the gimbal actuators indicated a backlash of 2 or 3 steps. This can be reduced by minor adjustments in the lead-screw and saddle-nut clearance. In tests described in Ref. 5, which details the equivalent SEPST II actuator, gimbal backlash was measured by a similar procedure, except that a Leitz dividing head (capable of reading angles to 1 arc-s), was used. In this case the backlash was less than one-half step.

The actuator leak rate was measured with a mass spectrometer with a 90% nitrogen, 10% helium gas mixture in the actuators. In all actuators, the leak rates were below 0.017 scc/h, which would give an extrapolated life of more than 10 years before pressure decayed to values at which vacuum welding would be a problem.

At the time that the translation actuator was designed, little was known about the configuration of the flexible cabling and propellant lines. The translation actuator

motor was sized to provide sufficient torque capacity to account for the flexible lines and was increased from size 11 (as in Ref. 5) to a size 15 for the SEPST III design. The cabling and feedline, as later designed, are nearly conservative and require little driving force. After the complete assembly of the total system, a drawbar pull test was performed in both the X and Y directions (the vertical arcs of translation are counterbalanced) resulting in about a 10-N pull force required to move the structure. This force is essentially the same as in the previous test structure. The maximum stall torque supplied to the load by the actuator is approximately 40 Nm. This corresponds to a force capability of 350 N (0.23-m-diam drum). Thus there is a substantial force margin, and a size-11 stepper motor would be sufficient for flight application.

In the previous tests on breadboard actuators reported in Ref. 5, an extensive amount of temperature testing was performed. The results of these tests indicated that the temperature in the actuators remained below 100°C during long-duration thruster runs. Since this temperature is below any component critical temperature, no temperature testing was performed on the present actuators.

f. Complete mechanism testing. The assembled mechanism was initially tested for a total of about 200 h, with 150 of these in vacuum (Ref. 6). In this period, only a few minor problems were encountered.

The translator mechanism was cycled approximately 2000 times/axis for a total of about 4×10^7 actuator steps in vacuum and 10^7 steps in air. After this testing period, the vertical translator actuator was found to exhibit erratic motion, which indicated a possible problem. Upon disassembly, both actuators were found to have significant wear on the motor pinion and mating first-stage gear, and the screws holding the flex spline to the output shaft were loose. The vertical-axis actuator had the greater wear, probably due to the heavier load. In this test, the gears were assembled without lubricant. The wear is believed to have resulted from both a lack of lubrication and the impact loading of the gears by the motor steps. After cleaning and lubrication, and using Loctite on the loose screws, both actuators (with the worn gears and original motors) returned to normal function. Further testing is in progress to evaluate the wear problem with both the old gears and the new lubricated gears. However, even with the wear, the actuators exceeded the total expected step requirements.

In initial gimbal actuator testing, the lead screw was lubricated with molybdenum disulfide and light oil.

Operation with the light oil lubrication produced a torque of the expected value. To determine their full performance range, the gimbal actuators were driven beyond the 10-deg design angle. At slightly less than 12 deg, the lead-screw and saddle-nut friction increased because of increased tension on the saddle nut from the strap, and the motor was generally unable to drive away from the ±12-deg mechanical stop. This problem is presently being studied. The proposed solution, which is being implemented, is the use of a recirculating ball-bearing-type lead screw to replace the original acme thread.

After over 4000 full cycles, the cabling and propellant lines show no visible signs of wear or fatigue. The original cabling has been used throughout breadboard air and vacuum testing for a period of eighteen months. In addition, separate tests of the thruster cables with 5 kV between alternate conductors were performed for about five months continuously. No cabling failures occurred.

The propellant lines also have been tested, without failure, for about 4000 cycles over a period of eighteen months. With the low stress level experienced by the line in flexing, the fatigue life should be greater than 10^6 cycles. Further testing will evaluate wear by the loop support trays, although no wear is apparent at this time.

g. *Mass summary.* The masses of the present TVC system components are summarized in Table 10. The reductions expected with redesign, primarily lightening the present concept, are shown in the "future" columns for a three- and five-thruster array. It is significant to compare the mass of the TVC system, including a small cold-gas system, with the mass required for a total cold-

Table 10. SEPST III TVC mass summary

Component	Present concept mass, kg	Future concept mass, kg	
	(3 thrusters)	(3 thrusters)	(5 thrusters)
TVC actuators	8.8	7.4	11.8
TVC thruster array and translator	55.0	17.0	22.0
TVC electronics	3.7[a]	3.7	3.7
Flexible cabling	5.7	5.0	7.0
Flexible feedlines	1.0	1.0	1.0
Caging for launch	3.0[a]	3.0	3.0
Total	77.2	37.1	48.5

[a]Estimated for flight hardware.

gas attitude control system, as shown in Table 11. Including the 9.1-kg cold-gas estimate and a five-thruster array, the TVC total attitude control system mass is about 58 kg. This represents a factor of 4 (hot gas) to 8 (cold gas) improvement over the attitude control system mass without thrust vector control.

Table 11. Comparison of attitude control gas storage requirements as a function of powered-flight control system mechanizations

Basic system	Variations			
	Cold gas, no panel trim	Cold gas, panel trim	Hot gas, no panel trim	Hot gas, panel trim
	Mass, kg			
3-axis cold gas	500	364	295	227
2-axis translator plus cold-gas third axis	38.7	25.5	11.3	16.0
2-axis translator plus gimbal third axis	9.1	9.1	6.8	6.8

F. Thrust Vector Control Servo Loop and Electronics

1. **General.** The TVC mechanism has produced a new problem for the vehicle attitude control system designer. Movement of the relatively large mass of the mechanism results in a vehicle angular displacement. A translator motion, intended to correct an attitude error, produces an additional angular error in the same direction. Without proper compensation, a simple control loop would be unstable. This subtle fact was apparently recognized by Mankovitz of JPL during the Jupiter mission study but not explicitly stated (Ref. 46). This instability was later noted by Barbera of NAR (Ref. 7).

2. **Three-thruster configuration.** For the purposes of the SEPST III test of the TVC, a three-thruster configuration was assumed to be nominally operating although simulations of a single-thruster shut-down transient were performed (Ref. 47). Since all rotational dynamics of the vehicle were simulated on an analog computer, it was necessary to include in the computer model the proper relationships of translator/gimbal motion and resulting torques about each axis of the vehicle.

Figure 39 shows the engine array in relation to a vehicle/solar-array configuration of a typical vehicle. The entire thruster assembly may be translated in the X and Y direction, and the outer pair of thrusters may be
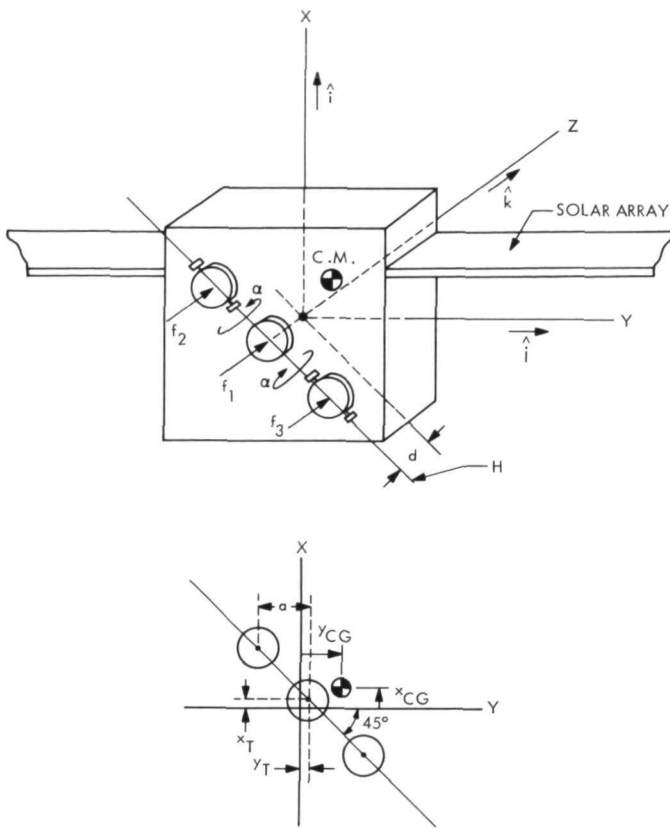
Fig. 39. Typical SEP vehicle three-engine configuration

rotated about axis H (in opposite directions). The resultant applied torque vector is derived as follows:

$\mathbf{F}_1, \mathbf{F}_2, \mathbf{F}_3$ = thrust vectors of engines 1, 2, and 3

$$\left.\begin{aligned}
\mathbf{F}_1 &= f_1\,\mathbf{k}\\
\mathbf{F}_2 &= f_2\,(\cos\alpha\,\widehat{\mathbf{k}} - \sin\alpha\sin 45^\circ\,\widehat{\mathbf{i}} - \sin\alpha\sin 45^\circ\,\widehat{\mathbf{j}})\\
\mathbf{F}_3 &= f_3\,(\cos\alpha\,\widehat{\mathbf{k}} + \sin\alpha\sin 45^\circ\,\widehat{\mathbf{i}} + \sin\alpha\sin 45^\circ\,\widehat{\mathbf{j}})
\end{aligned}\right\} \tag{5}$$

where α and the vectors $\widehat{\mathbf{i}}$, $\widehat{\mathbf{j}}$, and $\widehat{\mathbf{k}}$ are defined on Fig. 30, and f_1, f_2, and f_3 are the magnitudes of the thrust vectors.

$\boldsymbol{\ell}_1, \boldsymbol{\ell}_2, \boldsymbol{\ell}_3$ = vectors from center of mass (c.m.) to points of application of $\mathbf{F}_1$, $\mathbf{F}_2$, $\mathbf{F}_3$

$$\left.\begin{aligned}
\boldsymbol{\ell}_1 &= (x_T - x_{CG})\,\widehat{\mathbf{i}} + (y_T - y_{CG})\,\widehat{\mathbf{j}} - d\,\widehat{\mathbf{k}}\\
\boldsymbol{\ell}_2 &= (x_T - x_{CG} + a)\,\widehat{\mathbf{i}} + (y_T - y_{CG} - a)\,\widehat{\mathbf{j}} - d\,\widehat{\mathbf{k}}\\
\boldsymbol{\ell}_3 &= (x_T - x_{CG} - a)\,\widehat{\mathbf{i}} + (y_T - y_{CG} + a)\,\widehat{\mathbf{j}} - d\,\widehat{\mathbf{k}}
\end{aligned}\right\} \tag{6}$$

T = total applied torque = $\boldsymbol{\ell} \times \mathbf{F}$

$$\mathbf{T} = \boldsymbol{\ell}_1 \times \mathbf{F}_1 + \boldsymbol{\ell}_2 \times \mathbf{F}_2 + \boldsymbol{\ell}_3 \times \mathbf{F}_3 \tag{7}$$

$$\left.\begin{aligned}
\boldsymbol{\ell}_1 \times \mathbf{F}_1 &= f_1\,(y_T - y_{CG})\,\widehat{\mathbf{i}} - f_1\,(x_T - x_{CG})\,\widehat{\mathbf{j}}\\
\boldsymbol{\ell}_2 \times \mathbf{F}_2 &= f_2\,(\cos\alpha\,(y_T - y_{CG} - a) - d\sin\alpha\sin 45^\circ)\,\widehat{\mathbf{i}}\\
&\quad + f_2\,(-\cos\alpha\,(x_T - x_{CG} + a) + d\sin\alpha\sin 45^\circ)\,\widehat{\mathbf{j}}\\
&\quad + f_2\sin\alpha\sin 45^\circ\,(y_T - y_{CG} - x_T + x_{CG} - 2a)\,\widehat{\mathbf{k}}\\
\boldsymbol{\ell}_3 \times \mathbf{F}_3 &= f_3\,(\cos\alpha\,(y_T - y_{CG} + a) + d\sin\alpha\sin 45^\circ)\,\widehat{\mathbf{i}}\\
&\quad + f_3\,(-\cos\alpha\,(x_T - x_{CG} - a) - d\sin\alpha\sin 45^\circ)\,\widehat{\mathbf{j}}\\
&\quad + f_3\sin\alpha\sin 45^\circ\,(x_T - x_{CG} - y_T + y_{CG} - 2a)\,\widehat{\mathbf{k}}
\end{aligned}\right\} \tag{8}$$

Thus, the applied torque becomes:

$$\mathbf{T} = T_x\widehat{\mathbf{i}} + T_y\widehat{\mathbf{j}} + T_z\widehat{\mathbf{k}} \tag{9}$$

$$\left.\begin{aligned}
T_x &= (f_1 + f_2 + f_3)\,(y_T - y_{CG})\\
&\quad + (f_3 - f_2)\,(a + \alpha\,d\,\delta)\\
T_y &= -(f_1 + f_2 + f_3)\,(x_T - x_{CG})\\
&\quad + (f_3 - f_2)\,(a - \alpha\,d\,\delta)\\
T_z &= -(f_2 + f_3)\,(2a\alpha\delta) + \alpha\delta(f_3 - f_2)\\
&\quad \times (x_T - x_{CG} - y_T + y_{CG})
\end{aligned}\right\} \tag{10}$$

where:

$$\sin\alpha \cong \alpha \ (\text{for small } \alpha)$$
$$\cos\alpha \cong 1$$
$$\sin 45^\circ = \delta = 0.7071$$

The vehicle-fixed torque components derived above (for the rigid case) were programmed on the analog computer as functions of the variables α, x_T, and y_T, which were measured from actual thruster array motion in the vacuum test chamber. The torque expressions are a necessity for any realistic three-axis simulations of the vehicle dynamics with TVC if the thrust magnitudes are unequal and/or any thruster-out transients are to be studied. The results of the SEPST III closed-loop-system test are described in Section IV. However, certain preliminary tests are discussed in the following Subsection F-4.

3. **Control system design.** The solar electric TVC as originally proposed by Mankovitz (Ref. 46) and modified by Crawford (Refs. 48 and 49) is illustrated in the single-axis transfer function block diagram of Fig. 40. The block diagram, which in this case shows a thruster translator control loop, includes a convenient representation (θ^*) of the effect of translator reaction forces on the vehicle (valid for rotation about a single axis and for a rigid
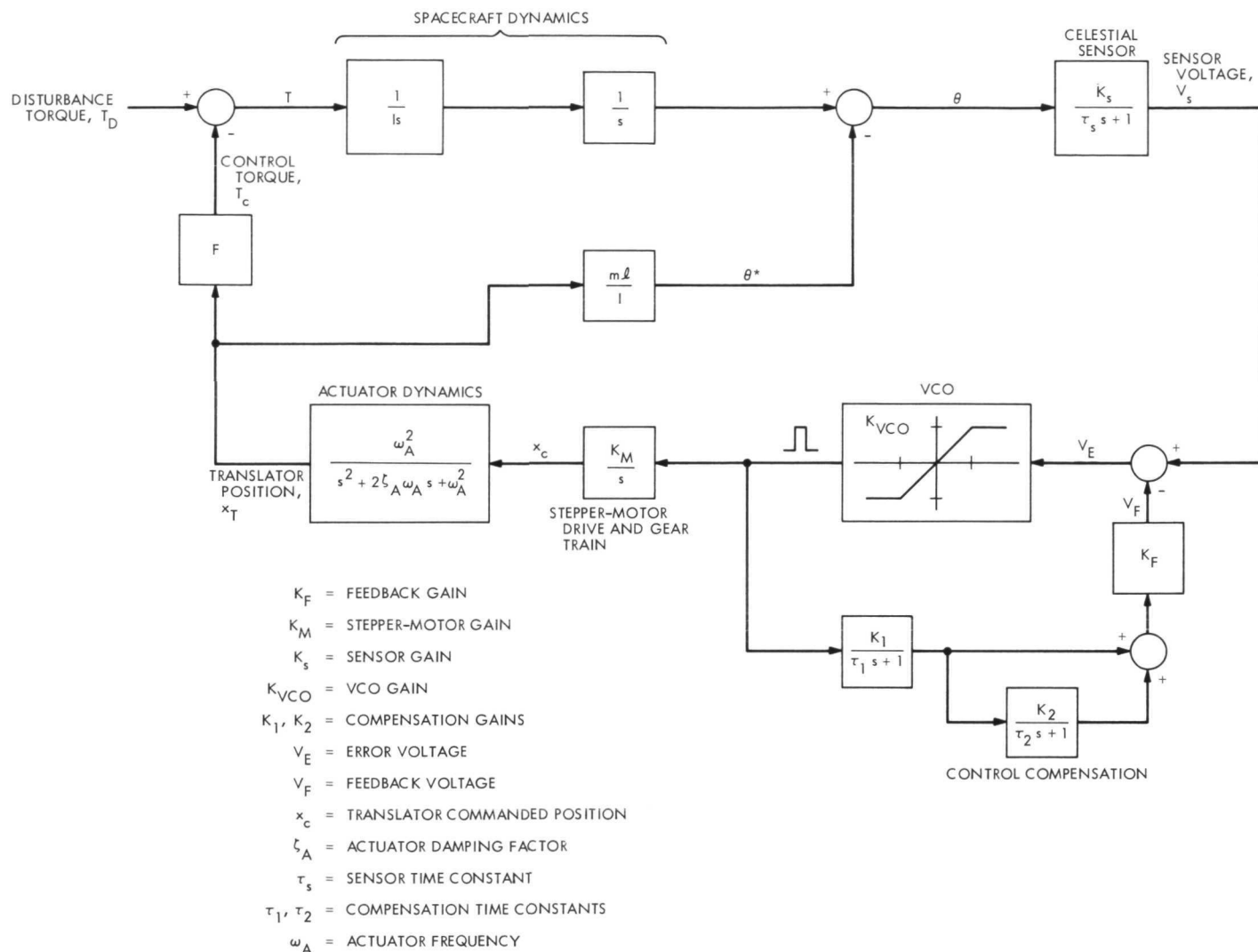
Fig. 40. Single-axis TVC transfer function block diagram

K_F = FEEDBACK GAIN

K_M = STEPPER-MOTOR GAIN

K_s = SENSOR GAIN

K_{VCO} = VCO GAIN

K_1, K_2 = COMPENSATION GAINS

V_E = ERROR VOLTAGE

V_F = FEEDBACK VOLTAGE

x_c = TRANSLATOR COMMANDED POSITION

ζ_A = ACTUATOR DAMPING FACTOR

τ_s = SENSOR TIME CONSTANT

τ_1, τ_2 = COMPENSATION TIME CONSTANTS

ω_A = ACTUATOR FREQUENCY

vehicle). The parameters m, ℓ, and I are the translator mass, the distance (perpendicular to the axis of rotation) between the vehicle c.m. and the translator c.m., and the vehicle moment of inertia, respectively. While translator interaction with the vehicle may be significant depending on the relative size of m, ℓ, and I, subsequent discussion in this report of the control problem will generally ignore this effect and assume it is relatively small.

The form of the gimbal control loop is virtually identical to the translator loop of Fig. 40. The output of the actuator dynamics block becomes gimbal angle α, which must be multiplied by the effective lever arm, $2a\delta$, and thrust, F, to produce control torque. Gimbal reaction torques on the vehicle are assumed to be of insignificant effect.

The present approach to stabilization of the translator (or gimbal) control system is illustrated in Fig. 41, where the control compensation is applied in a feedback loop around the voltage-controlled oscillator (VCO). The transfer function block diagram of Fig. 42 is a linearized version of the control loop, neglecting the high-frequency translator actuator dynamics and translator-vehicle interaction forces, but including the "tail-wags-dog" effect. The stability analysis of the linearized control loop is discussed in detail in Ref. 47.

Figure 42 shows the general form of the feedback circuitry (Ref. 48). The feedback signal is derived from the VCO output directly rather than from a potentiometer that measures translator (or gimbal) position. In this way, it is clear that a substantial improvement in feedback
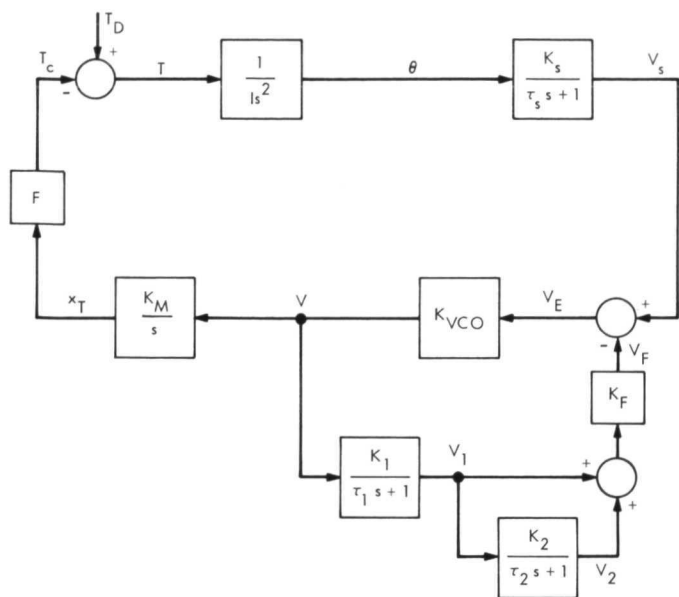
Fig. 41. Simplified TVC single-axis block diagram

signal-to-noise ratio can be obtained at the expense of
having a direct indication of translator (or gimbal) mo-
tion. Since the latter consideration is not necessary for
proper control-loop operation (absolute knowledge of
actuator output position is not required except for tele-
metering purposes), it is sacrificed for the former.

The stepper motors chosen for the actuators are 90°-
per-step permanent-magnet motors that feature a mag-
netic detent at each step. This detent allows the stepper
motor to be operated in a pulse fashion rather than having
the stepper-motor windings continuously powered. This
feature results in a significant power saving since the
stepper-motor duty cycle is low in the solar-electric
thrust vector control subsystem.

Commercially available stepper-motor driver elec-
tronics have three characteristics that make them unac-
ceptable for the thrust vector control system. These are:

(1) Windings are continuously powered, therefore
    wasteful of power.

(2) The electronics have a latch-up mode that is cor-
    rectable only by removing the power-supply volt-
    age.

(3) The reliability of the electronic components is
    unknown.

The design, as described in Ref. 48, corrects all of the
above undesirable features. Thus, the details of the
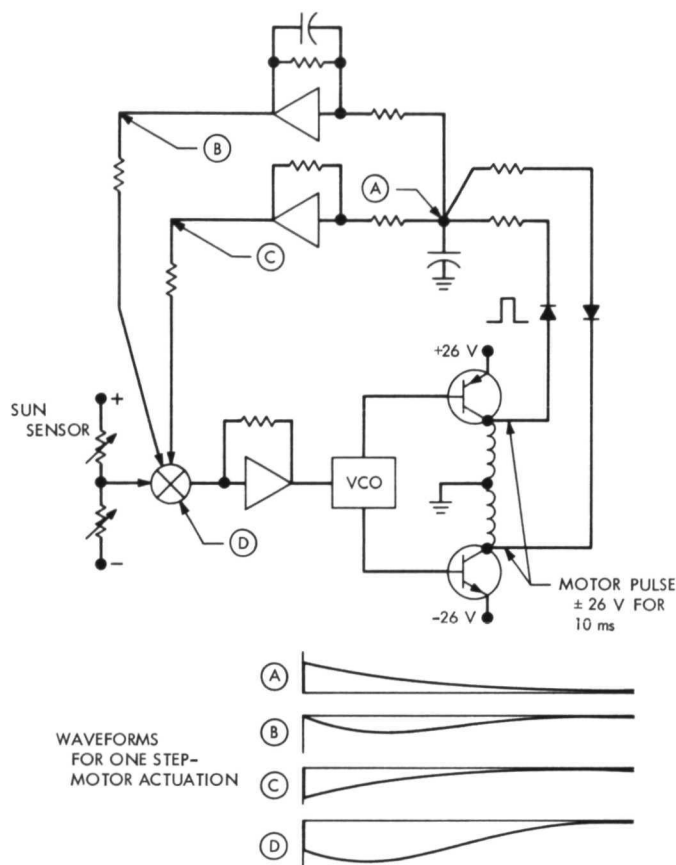
Fig. 42. Mechanization of SEPST III translator controller
and compensation

SEPST III stepper-motor driver electronics need not be
discussed in this report. However, the assembled driver
electronics for one stepper motor are shown in Fig. 43.
Each driver requires nine flat-packs, eight transistors,
and a few additional discreet parts. The circuit design
uses very little power, is free from latch-up states and
uses high-reliability components.

The closed-loop electronics package used in the SEPST
III system is shown in Fig. 44. A similar panel for open-
loop testing was also used as described in Ref. 45.

4. Preliminary TVC system tests. The closed-loop con-
trol electronics were initially tested in breadboarded
form. Tests on a single-axis loop, using simple analog
simulation of vehicle dynamics, produced results quite
similar to those determined analytically. The results are
indicated in Fig. 45. The similarity of the convergence
of the phase plane characteristics is striking.

An unexpected result of the mechanization of the
closed-loop thrust vector control system was the presence

of a very low-frequency, very low-amplitude oscillation in each axis of the control system. This oscillation was a function of the electronic compensation time constants and the amount of backlash in the gimbal and translator actuators. The electronic time constants determine the period of oscillation and the actuator backlash determines the amplitude of oscillation. Tests were run to show the effects of actuator backlash on the system. Table 12 summarizes the results.

The oscillations are a smooth sinusoid and show no irregularities. One important result of the tests shows the effect of actuator backlash on the number of stepper-motor pulses. The expected total number of pulses to be allowed per motor in the TVC System is 10^7 per axis. This includes ground testing. Assuming a one-year thrust program for typical solar electric missions it is necessary to limit the pulses to once every three seconds on the average. It can be stated that the gimbal actuator with large backlash as shown in Table 12 will not meet the mission requirements, since the margin is too small to

Table 12. Effect of actuator backlash on stepper-motor pulse rate

Actuator	Back-lash, steps	Oscilla-tion period, min	Oscillator amplifier peak-to-peak, deg	Step motor pulses/ cycle	Average time between steps
Translator	1	30	0.004	~20	1.5 min
Gimbal No. 1	0.6	30	0.006	~20	1.5 min
Gimbal No. 2	6	30	0.06	~200	9 s
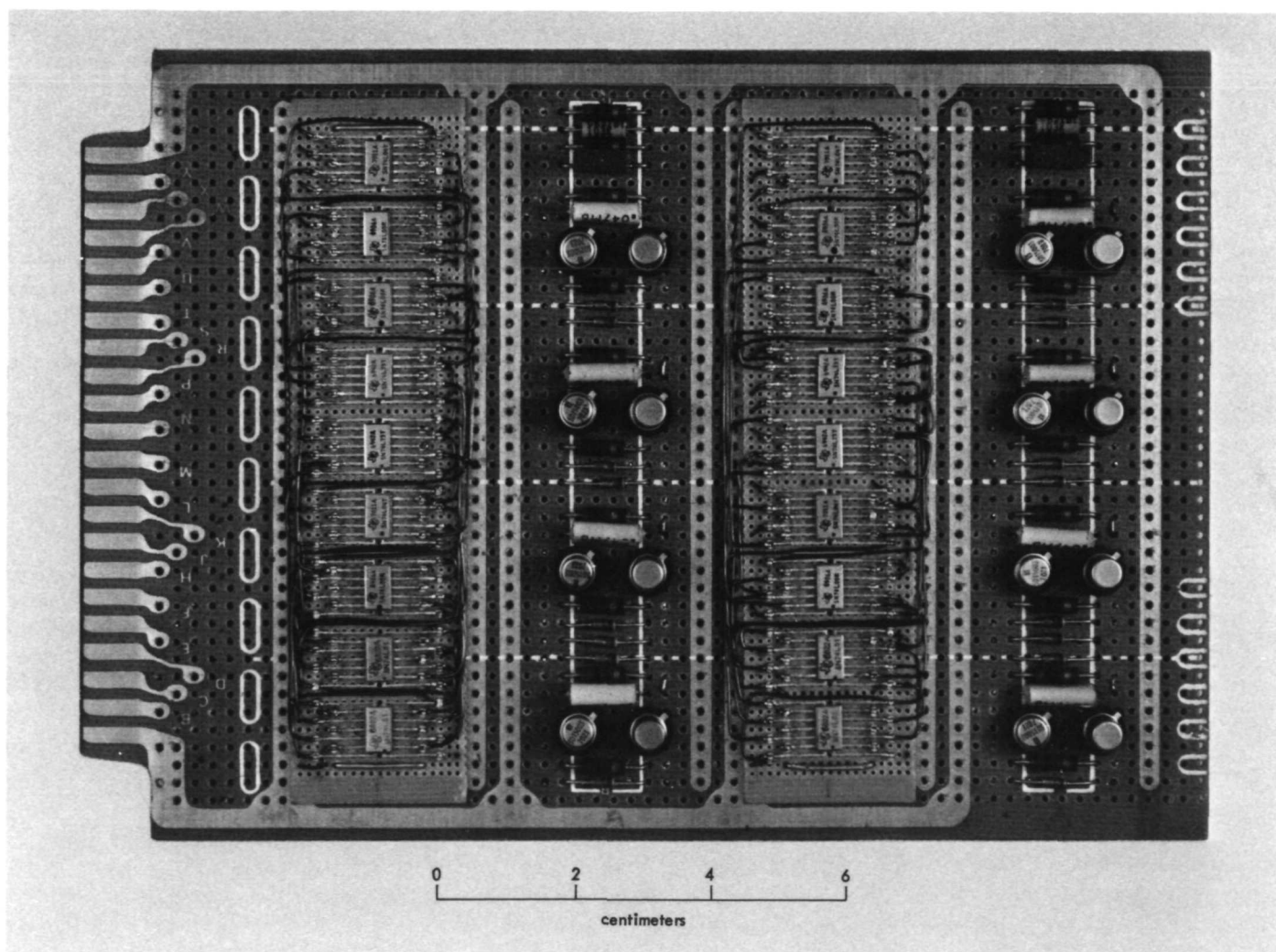
Fig. 43. TVC stepper-motor driver electronics
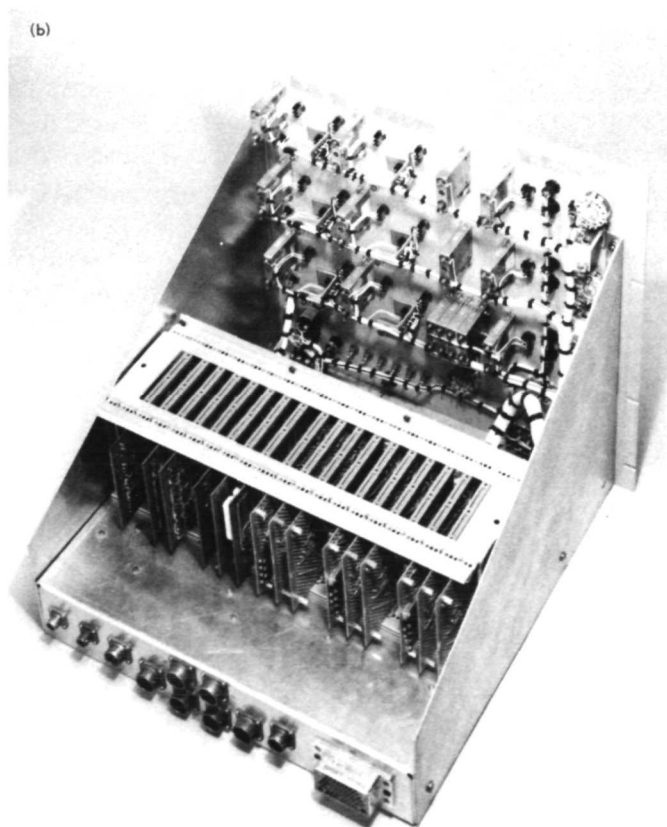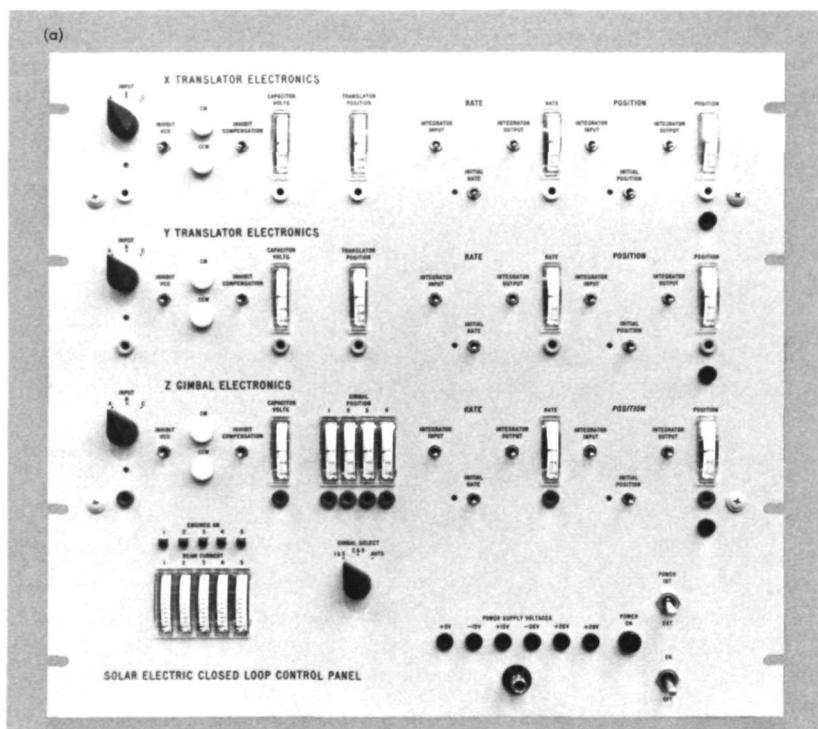
Fig. 44. TVC closed-loop electronics control panel:
(a) front view; (b) rear view
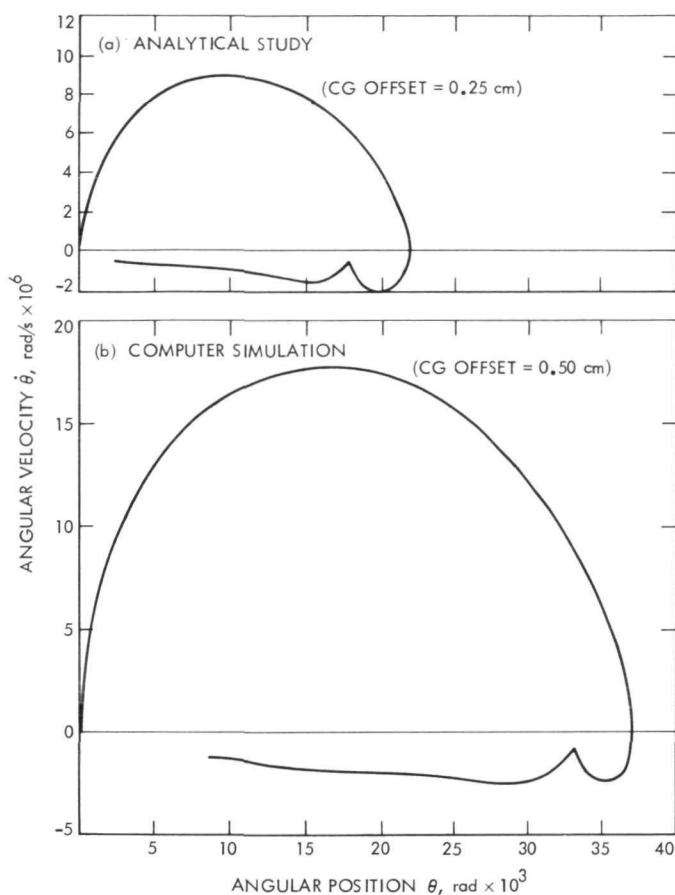
Fig. 45. Translator control-loop phase plane response

allow for acquisitions, thruster switching, variations in external torques upon the spacecraft, and variations in the thrust profile.

A benefit from the mechanization, not anticipated from the analyses, is a reduction in the total number of stepper-motor pulses in the limit cycle. Computer simulations showed stepper-motor pulses every 30 or 40 s average while the actual hardware pulses every 90 s on the average (small backlash case). The computer simulations do not include actuator backlash or the effect of discrepancies between actuator movement and electronic feedback.

5. TVC electronics noise sensitivity. Studies and laboratory tests show that the extreme sensitivity of the SEPST-III-type TVC electronics to electrical transients, low-frequency noise, and noise on the ground buss will require a radical departure from the conventional Mariner-type attitude control spacecraft configuration. Vehicle designs that allow the Canopus Tracker and Sun Sensors to be physically separated as in the Ranger-Mariner class

of vehicle cannot now be permitted in the proposed SEP vehicles. With the existing design of the TVC electronics, noise on the order of 5 mV will cause the stepper motors to pulse once every 3 s, independent of control functions the stepper motors will have to perform. This pulse rate will cause the stepper motors to exceed their lifetime specification of 10^7 pulses for the proposed missions.

One reasonable solution to this noise sensitivity problem is to combine the Celestial Sensors (both Canopus Tracker and Sun Sensors) into one assembly and to mount the high-gain thrust vector control electronics on the assembly. The Celestial Sensors assembly will have its own power supply and will be relatively immune to the typical vehicle electrical noise environment. Because of the short distance between the Celestial Sensors and the TVC electronics, electrical pick-up will be minimized. The TVC electronics output signals will be high-level digital signals that are immune to the vehicle noise environment.

The noise susceptibility of the thrust vector control system is caused by the large dynamic range of the system. This dynamic range dictates an electronic control that is responsive to very small changes in input error signals (i.e., the system is sensitive to noise). Since actual sensors were not used in SEPST III, this noise sensitivity was not a difficulty. However, space vehicle systems using sensors would have difficulty.

A second, and possibly more desirable solution to the noise sensitivity problem is through the use of "rate estimation" to determine the vehicle rotational rate from the sensors. The investigation of rate estimation was started during the SEPST III phase but was not completed in time to be included in the final test program.

The utility of a state estimation circuit, derived by Kopf (Ref. 50) specifically for the task of estimating the angular rotation rate of a space vehicle, was investigated as it might apply to the same basic solar-electric thrust vector control problem. The estimator, receiving celestial sensor measurements of the space vehicle's angular position, both filters the sensor signal and derives an estimate of vehicle angular rate.

Comparisons of X- and Z-axis responses in particular show the simulated rate estimator loops to be well damped and substantially faster than the standard SEPST III control hardware (Ref. 47). The gimbal loop (Z-axis) response was drastically improved due to the estimator

and proper control parameter choices. The low inertia, Y-axis control loop was adjusted to provide good response without lowering the celestial sensor gain as was done in the standard system.

In summary, the rate estimating TVC certainly promises a vastly improved control capability over the standard approach. A control bandwidth improvement by a factor of 2 to 3 does not seem unreasonable, and yet this still does not threaten to result in any significant solar-array interaction problems, much less any serious destabilizing effects.

G. Propellant Storage and Distribution

1. **General.** The study of mercury-propellant tankage concepts for an SEP system began in 1965 (Ref. 51). Initially, positive expulsion metal bladders in spherical tanks were used but were discarded because of fatigue failures and high pressurization requirements. Elastomeric bladders were chosen to avoid these problems. SEPST III tankage evolved from a design discussed in Ref. 52. A 23-cm-diam spherical tank was chosen to store about 82 kg of mercury. In contrast with the SERT II blow-down-type pressurization that substantially increases the tank size, a pressurization scheme using a liquid (Freon TF) in equilibrium with its vapor was chosen. The propellant storage and distribution (PDS) system is shown schematically in Fig. 46. The PSD is comprised of three

major elements: (1) the tank, (2) the propellant expeller, and (3) the pressurant. Other necessary components include the shutoff valve, pressure transducer, thermal control heaters, and distribution line(s) from the tank to the thruster(s).

2. **Tank design.** Early in the tank development, Ti-6Al-4V was selected to be the most desirable of the candidate materials due to its high strength-to-weight ratios. At that time, this alloy appeared to be compatible with the pressurant (Freon TF, also known as Freon 113), but there had been concern over its compatibility with the propellant (mercury) for long periods, e.g., 10,000 h. Consequently, at that time, a number of titanium samples were soaked in mercury for 3000 h, put through the conventional tensile tests, and subsequently examined (Ref. 52). As a result of this examination it was concluded that no problems should be encountered at the expected operating temperatures and pressures and that Ti-6Al-4V was the recommended tank material. However, further considerations since that time (which are discussed in Subsection 6) indicate that such a conclusion may not be appropriate at this time. The design selected (Ref. 53) is shown in Fig. 47 with the design features listed in Table 13. Two tanks with the welded construction shown in Fig. 47 were fabricated. Earlier in the program, stainless steel tanks, with a clamping configuration for sealing, were built to evaluate seal designs. The stainless tanks were used in the SEPST III final test.
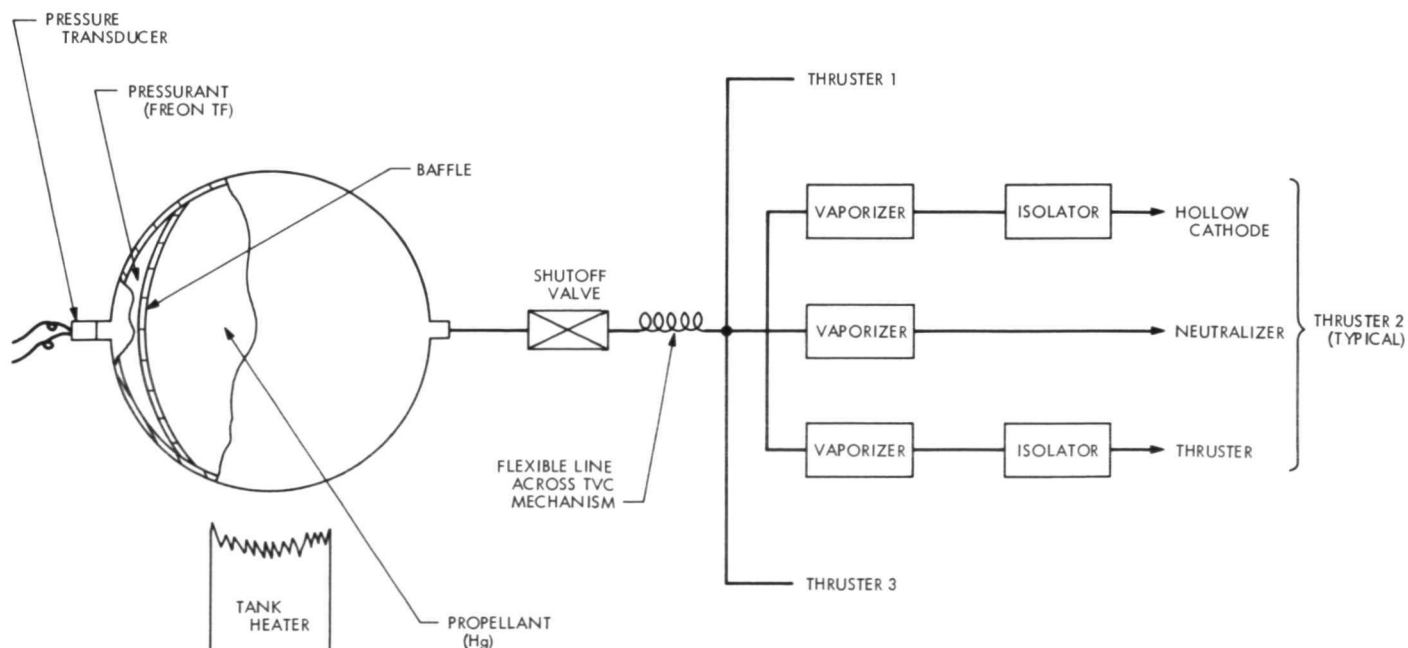
Fig. 46. Schematic of propellant tankage and distribution subsystem
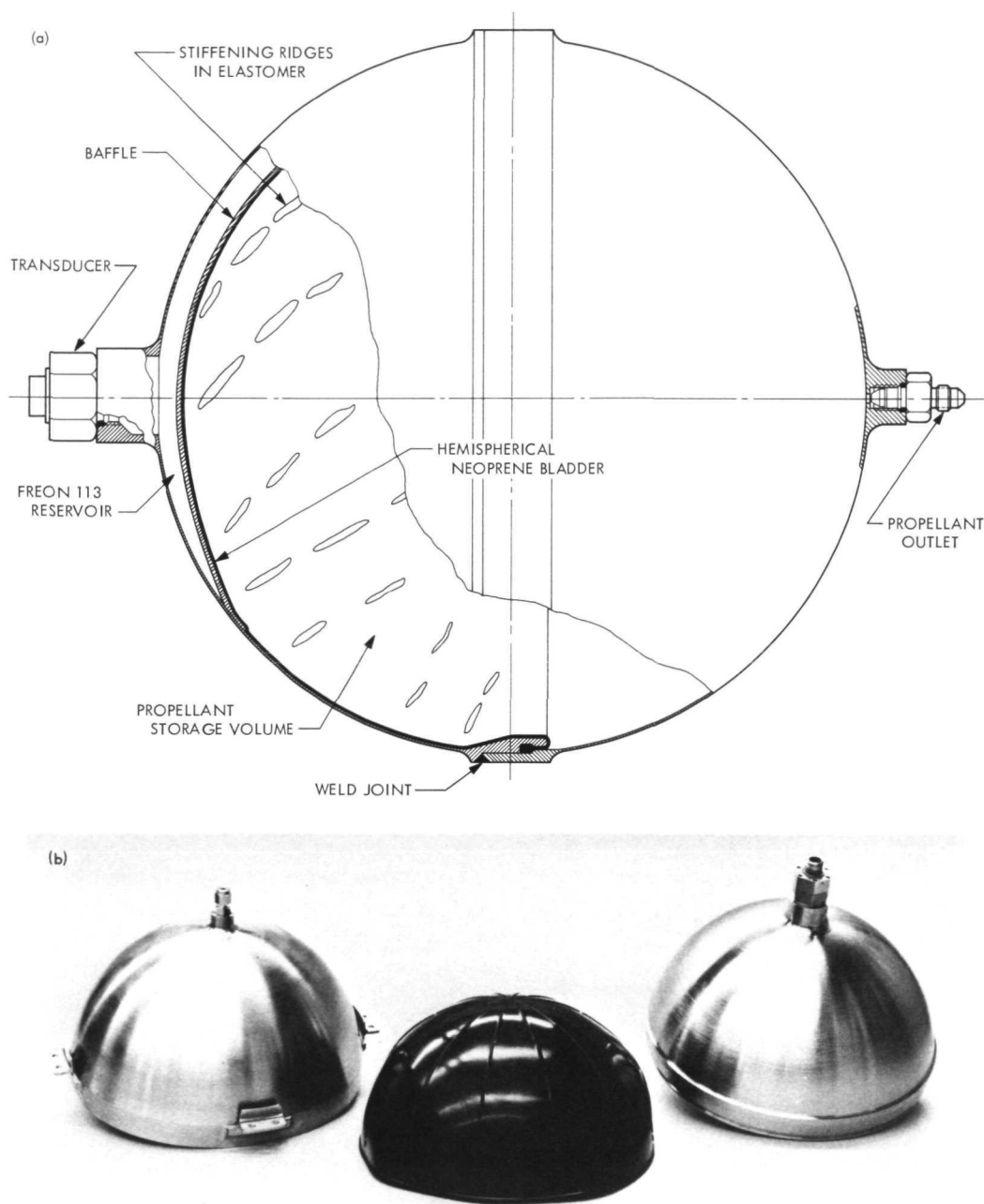
Fig. 47. SEPST program propellant tank design (propellant-loaded position): (a) line drawing; (b) disassembled mercury propellant tank (titanium, 82 kg capacity)

3. Propellant expeller. The propellant expeller, which is also the interface between the propellant and the pressurant, is an inverting elastomer bladder made to have high strength (tensile strength $= 27.6 \times 10^6$ N/m² (4×10^3 lb/in.²)) with the composition shown in Table 14.

Evaluation of the compatibility of mercury and neoprene elastomers led to the selection of a neoprene (Ref. 52). From permeability tests of neoprene to the pressurant

(Freon TF), it was concluded that the Freon-neoprene combination was suitable.

In the fabrication specification, the bladder-curing requirement was specified to be 20 min, at 307°F. With these specifications, it was estimated that the neoprene had a tensile strength of 4000 lb/in.², an elongation value of 7000%, a tear strength of 450 lb/in., and a hardness of 61 Shore A.

Table 13. Propellant tank features	
Parameter	Parameter value
Material	Ti-6Al-4V (room temperature yield strength for original billet unknown, but for final shell configuration can probably be assumed approximately 8.27×10^8 N/m² (120,000 psi))
Configuration	Spherical; 22.9-cm (9.00-in) ID; 0.051-cm (0.020-in., nominal wall thickness
Dry weight	1.18 kg (2.6 lb) (includes expeller)
Volume available for propellant	5900 cm³ (360 in.³) (allows for 81.8 kg (180 lb) Hg)
Volume available for pressurant	160 cm³ (10 in.³) (allows for 0.23 kg (0.5 lb) Freon TF)

4. Pressurant. The mercury propellant is expelled from the tank by the expeller which is pressurized by Freon-TF vapor. To insure that essentially all the mercury is expelled, while not exceeding the surface tension forces of the vaporizer, the vapor pressure should be maintained within the range of 3.5×10^4 to 2.1×10^5 N/m² (5 to 30 psia), corresponding to a temperature range of about 15.6°C to 82.3°C. Maximum expected temperature is about 65°C.

The volume required to insure that all the mercury is expelled from the 23-cm-diam tank was calculated to be about 82 cm³ (Ref. 52). The present design allows for about 164 cm³, or about 0.23 kg Freon TF.

5. Compatibility of expeller with pressurant (Freon TF) and propellant (mercury). Initial expulsion tests using neoprene, as designated in Table 14, were reported in Ref. 53. Since that time a two-month soak test at 65.5°C was completed, whereupon the mercury was expelled, the setup disassembled, and the neoprene expeller examined. The diaphragm was intact and appeared to be in satisfactory condition.

6. Compatibility of tank (Ti-6Al-4V) with pressurant (Freon TF) and propellant (mercury). As mentioned, static sample testing indicated that Ti-6Al-4V was compatible with both pressurant and propellant. At first glance the design seems more than adequate. For example, using the standard stress equation for a sphere with internal pressure, the theoretically required wall thickness (t) (neglecting welding joint efficiencies, and corrosion) is calculated to be (for 3.5×10^5 N/m²)

$$t = \frac{PR}{2S} = \frac{1.94 \times 10^4}{S} \quad (11)$$

Table 14. Expeller composition	
Material	Parts by weight
Neoprene GN	100
Stearic acid	1
Neozone A	4
Maglite D	4
EPC	30
Zinc oxide	5

where S = allowable stress, P = pressure, and R = radius. Assuming that S is ¼ the ultimate (8.14×10^8 N/m²), t is on the order of 0.01 cm. The actual thickness is 0.051 cm, which is about the minimum that can be achieved in machining. Since this tank design was considered for flight-type application, a stress analysis was performed to determine if the tank could withstand loads typical of those experienced during a launch, viz, a 10-G vertical load in the direction toward the propellant exit, a 4-G vertical load 180° away from the 10-G load, and 4-G lateral loads. Under these conditions and assuming a tank fully loaded with propellant and pressurant, the membrane stress was calculated to be about 1.03×10^7 N/m² (15,000 lb/in.²), which was not considered excessive.

A factor not taken into account was the consideration that the selected material is one of those high-strength materials (defined as one whose yield strength-to-density rates = 1.78×10^3 m or higher) that can fail by catastrophic, brittle fracture (rather than by plastic deformation) at some stress well below the yield strength. These high-strength materials are also susceptible to stress-corrosion cracking in the presence of certain environments, causing failure to occur at an even lower stress. Such failures were not observed in the earlier "soak-and-pull" tests performed on the samples because conventional tensile (and impact) tests do not reveal the tendency of a material toward brittle fracture behavior (Ref. 54). The subject of fracture and its behavior is much too broad and complex to be fully explored here but a summary of its concept and terminology is in order so that further discussion in this report can be better understood. For more details on the subject Refs. 55 through 68 are pertinent and suggested.

Brittle fracture, which is known to originate at cracks or crack-like flaws, can be analyzed by a number of ways.

The basic assumption in fracture mechanics is that failure occurs when the stress intensity, K_I (a single solar

quantity proportional to the applied load and the geometry of the cracked body), at the flaw tip reaches a critical value, K_{IC}. This critical value, also termed fracture toughness, is independent of loading conditions and may be considered a material constant. Therefore, the critical stress intensity can be obtained with either an increase in flaw size or an increase in stress level. Flaw-size changes are a result of subcritical flaw growth, which can be caused by cyclic stresses and/or sustained stresses in an aggressive environment. From results of sustained stress testing of cracked specimens (Ref. 65) it was observed that there was an apparent threshold stress intensity below which flaw growth does not occur. Where flaw growth is due to stress corrosion this apparent threshold value is designated K_{ISCC} [it should be noted that stress-corrosion cracking always involves the conjoint action of both stress (tensile stress only) and corrosion]. Consequently, to do a fracture mechanics evaluation requires among other things that the K_{IC} and K_{ISCC} values for the material either be known or derived.

Out of necessity the SEPST III tank design was evaluated ex post facto, since the shells had been fabricated prior to a fracture mechanics analysis. Results of this evaluation and its impact on the applicability of the design for a mission consideration are discussed in Subsections G-6-a and -b. Results of two separate analyses are presented: (1) the effect of Freon TF on the tank design, and (2) the effect of mercury on the design. It has been assumed throughout that the diaphragm is adequate to prevent any Freon TF from passing into the mercury side of the tank, so that a third possible analysis (i.e., the effect of a mercury-Freon-TF mixture on the design) would not be necessary.

a. Ti-6Al-4V and Freon TF. Fortunately, fracture toughness data exist for Ti-6Al-4V in a Freon-TF environment. From tests reported in Ref. 65, it was determined that K_{ISCC}/K_{IC} is about 0.59, which one might consider very roughly as a "corrosion factor." More clearly, the explanation of this ratio is the following. For Ti-6Al-4V with a certain size crack or flaw there is some stress (below the yield value) at which the flaw will increase at such a rate that only a catastrophic failure can occur, even if the stress were relieved immediately upon reaching that value. The stress intensity associated with this set of circumstances is K_{IC}. Note should be made that at initially lower stresses than the critical stress, the flaw may or may not grow. If the titanium alloy, while stressed, is in Freon TF the flaw will not grow if the stress intensity is 59% that of the critical stress intensity. Or, similarly, if it is assumed that the flaw sizes are the same

in both cases it also means that the stress is 0.59 that of the critical stress.

Using this information and assuming a safety factor of 5, the proof stress the present tank (in contact with Freon TF only) should withstand without failure is calculated to be

$$S = \frac{PR\,(5)}{2t\,(0.93)\,(0.59)} = 3.5 \times 10^8\ \text{N/m}^2\ (5.13 \times 10^4\ \text{lb/in.}^2)$$

(12)

where 0.93 allows for the decrease in strength due to a maximum expected operating temperature = 65.5°C (150°F) (Ref. 52). A safety factor of five was suggested because of the questionable quality of the tank welds and because the yield strength of the tank material was not really known. To attain the above proof stress each of the tanks must be proof tested to a pressure of

$$P_{proof} = 3.5 \times 10^5 \frac{5}{(0.93)\,(0.59)}$$

$$= 3.2 \times 10^6\ \text{N/m}^2\ (460\ \text{psia})$$

(13)

b. Ti-6Al-4V and mercury. Unfortunately, the compatibility of Ti-6Al-4V in the presence of a mercury environment is not as clearly defined as that with Freon TF. Presently available data and other sources suggest that the use of such a combination is highly questionable, especially when the material is used in a pressure vessel application. In a recent solar-electric propulsion vehicle mission study report (Ref. 7), 304-LC stainless steel was chosen because of "reported attacks" on both aluminum and titanium by mercury. References 55 and 58 report these incompatibility problems.

In Ref. 55 it is reported that the liquid mercury-titanium couple is known to exhibit liquid metal embrittlement. However, it is not too clear on what temperatures and stress conditions this observation was based. Reference 58, in the main, reports high temperature ((204 to 982°C) (400 to 1800°F)) corrosion data. The authors of Ref. 58 note that "stress-corrosion cracking of titanium and its alloys can occur on mercury" and that "additional studies in this area are recommended before committing titanium or its alloys to use in contact with mercury." Some data relative to reducing corrosion at high temperature applications by nitriding the surface are tabulated, and indications are that for some of the titanium alloys corrosion can be reduced. However, Ti-6Al-4V apparently was not one of the alloys considered as it was not on the list. The authors conclude (for high-temperature

considerations) that based on the data presented, "the applicability of titanium for mercury service is limited. Additional data should be obtained before any such use is planned." The only data at room temperatures (25 to 33°C) were for unalloyed titanium A-70. Results of these data indicate that "no evidence of oxidation, cracking, or loss of coherence was observed for liquid Hg" exposed to the Ti-A-70.

As a result, the compatibility of 6Al-4V titanium is unresolved. Sample testing, presently in progress at TRW, to obtain fracture toughness data on 304 stainless steel and 6Al-4V titanium may help clarify the issue in the near future.

7. Other PDS components. Presently, the distribution tubing is 300-series stainless steel and will probably remain the same for flight requirements. The shutoff valve is a VALCOR Engineering Corp. Latching-Type Valve (Part No. V66600) weighing 0.25 kg. This valve was designed for launch loads but has not been qualified. Similarly, the transducer (Statham Absolute Pressure Transducer Model No. PA 285TC-50-350 constructed of 347 stainless steel, and weighing 0.11 kg) might also be considered flightworthy. In the SEPST III test setup the tank heaters were commercial 115V-AC glass-insulated heater tapes.

8. Bench testing. The experimental setup and execution of the tests were similar to those described in Refs. 52 and 53. Figure 48 shows the tank mounted on the test
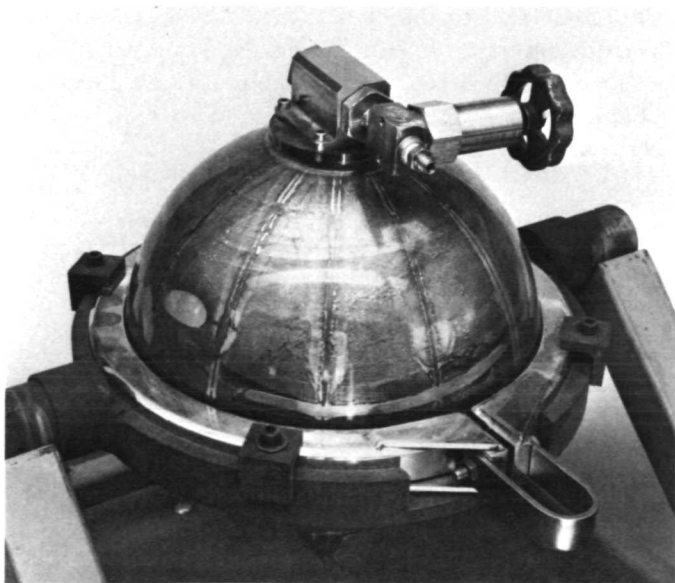
Fig. 48. Diaphragm evaluation test setup (postexpulsion)

stand. The tank design is similar to that described in Ref. 52 except that a lucite, rather than a stainless steel, hemisphere was used for the mercury-expulsion side of the tank.

In three of the six runs performed, 35 psia GN_2 was used to expel the mercury. The tankage (including mercury) was at ambient temperature for two of the runs and at approximately 150°F for the other. Freon 113 was used in the remaining three runs with the tankage temperature at approximately 150°F. The Freon pressure was measured to be approximately 25 psia, which agreed with the vapor pressure expected at this temperature. The tank was oriented alternately in two positions to satisfactorily test the bladder: (1) with the mercury outlet 90 deg from the vertical, and (2) with the mercury outlet in the top vertical position.

After each of the six tests, the bladder was removed from the tank and carefully examined. Special attention was directed to the portions of the bladder near the location where the bladder formed the seal between the two hemispheres. No failures were observed from any of the runs, and it was concluded that the present bladder design is satisfactory.

In assembling the SEPST III setup, using the latching value, the possibility of excessive pressure spikes ("water hammer") at the vaporizers after opening the valve was considered. A test was performed to measure the pressure overshoot at the end of a 3-m coiled feedline. This line was one half of the feedline crossing the TVC mechanism (Subsection E-3-d). The latching valve was placed between a mercury reservoir and the coiled line. A pressure transducer was placed at the end of the line. The feedline was evacuated with a vacuum pump before opening the valve.

Results of the tests are shown in Fig. 49 for three conditions. The three runs correspond to different levels of reservoir pressurization. The pressure overshoot is reasonably small for all cases (10%). The suppression of the "water hammer" is attributed to the coiled line and the small tubing bore. It was concluded that opening the valve between a pressurized tank and the vaporizers would not cause vaporizer damage or push mercury through the porous tungsten.

9. Environmental testing. A major question to be resolved is whether or not an off-loaded SEPST-III-type tank can adequately withstand the expected launch vehicle vibration load levels and thereafter function properly for 10,000 h. Of primary concern is the effect of
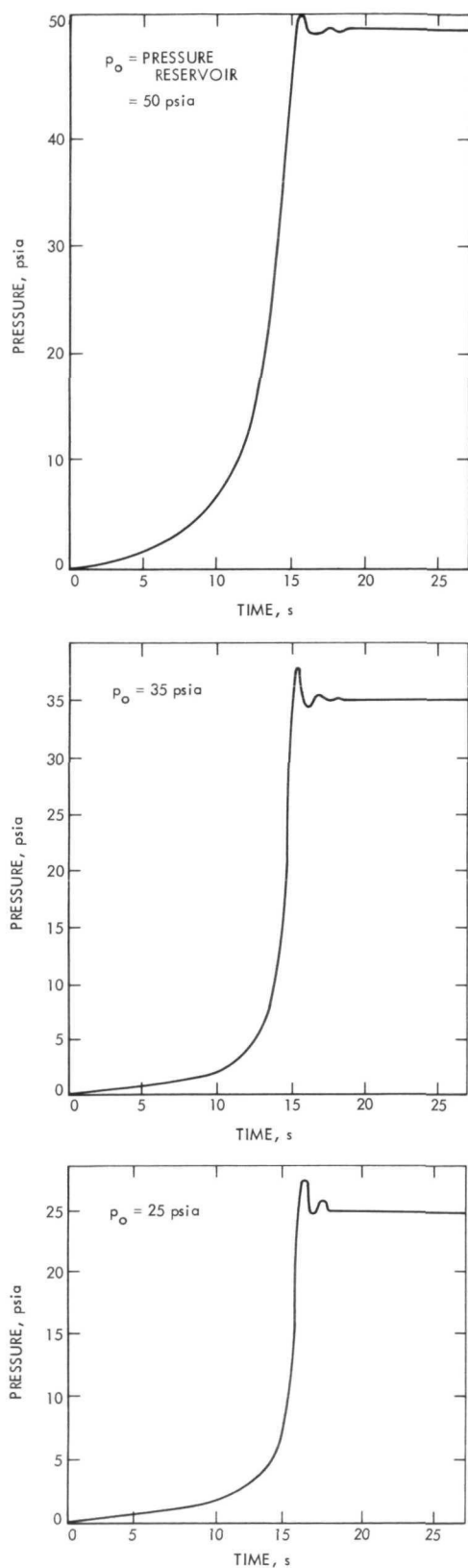
Fig. 49. Hg "water effect" in feedline (feedline: length = 3 m, OD = 0.152 cm)

propellant sloshing on the tank, baffle, and diaphragm. In addition, sloshing tests will define tank mounting forces required for structural design.

H. Command and Control Subsystem

1. General. It is anticipated that the SEP TSS on deep space missions will require some degree of automatic control. This control requirement results from the expected limited use of communications through the Deep Space Network (DSN) due to the time sharing of the DSN for multiple missions. During long periods (up to a week) without communications, off-normal TSS operation could jeopardize the mission success and/or make guidance and navigation impossible.

The SEPST III command and control subsystem (CCSS)* was designed to automatically perform all presently known TSS control functions. This approach allowed the difficulty of fully automatic control to be assessed and provides a baseline for possible modifications or simplifications. The primary part of the CCSS is a PDP-11 digital computer. The input and output (I/O) logic (Fig. 50) is the interface for the computer (Fig. 1) with other elements. The computer is commanded from a teletype for initial startup, interrogation, data printout, override and shutdown.

2. Requirements. To provide adequate data for subsequent trade-off studies, it was decided that the SEP-controller should be capable of performing all presently envisioned control and monitoring functions required for fully automated subsystem operation. One can distinguish functions related to the operation of the subsystem and those dealing with the emergencies created by a subsystem malfunction or component failure. These functions include:

(1) Feedback-dependent turn-on sequencing.

(2) Performance monitoring and correction of substandard operation.

(3) Failure detection, identification and elimination.

(4) Adjustment of thrust level and selection of the number of operating thrusters, in accordance with a prestored flight plan.

In addition to the above mission-oriented requirements, the SEP CCSS also had to be designed to meet the

*The designation "CCSS" is used to distinguish the SEP TSS Computer from the standard space vehicle "CCS."

requirements of a subsystem engineering development program. These included providing test engineering capability for monitoring, checkout, and manual intervention. Fail-safe features for unattended operation of the breadboard thrust subsystem also had to be provided.

In view of the R&D character of the project, a software implementation was selected because of the flexibility it provided for expeditious modification during subsystem integration and checkout. It was recognized that this implementation mode would require considerably more computer memory and computational capability than would be needed or available on an actual mission; the optimization of the implementation mode for a flight CCSS will be the subject of future trade-off studies.
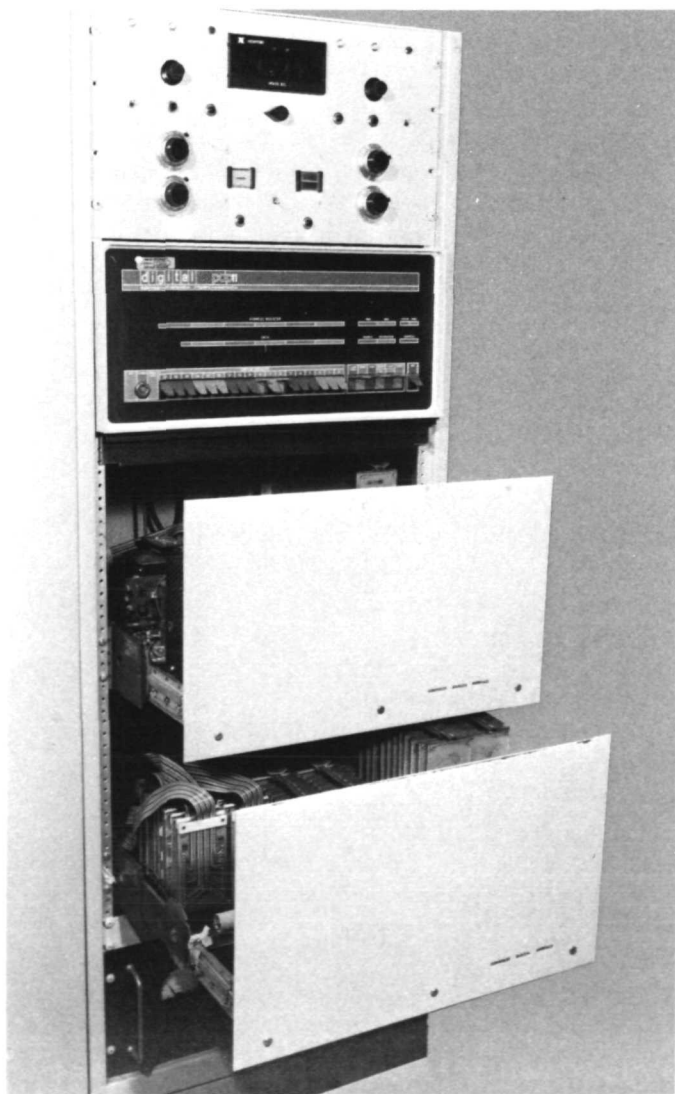
Fig. 50. System computer (PDP-11)

3. Implementation.

a. General. Because of the developmental nature of both the CCSS and the thrust subsystem the flexibility of a programmable controller was considered indispensable. The selected implementation mode was that of a dedicated, general-purpose minicomputer (Ref. 69). Application of a commercial minicomputer allowed the execution of all functional subroutines in software. The required size memory, capable of satisfying the needs of the program, could easily be provided.

The possibility of sharing usage of a large multipurpose computer, such as the UNIVAC 1108, was precluded by the difficulty of maintaining continuous operation in competition with higher priority users of the large computer. Furthermore, the power, word size, and operating system complexity of a large computer would have resulted in a software program that would be difficult to relate to any onboard computer. Minicomputers, on the other hand, have many similarities with vehicle computers, and where differences do exist, they are readily identifiable. The possibility of using an actual spacecraft-type computer was not seriously considered because none were available.

The actual computer selected was a PDP-11 computer with 8124 words of 16-bit memory. An ASR-35 teletype was used to provide operator communication and to simulate the ground station. A special-purpose analog and digital interface, described in Ref. 70, enabled the controller to send and receive the necessary signals. The PDP-11 computer and the interface hardware are shown in Fig. 50. Specific programming information is presented in Ref. 70.

b. Software implementation. The primary software vehicle for the implementation of the functional requirements is the functional subroutine (FSR). Each identifiable controller task is represented by an FSR and all CCSS requirements can be satisfied by some combination of these FSRs (Ref. 69).

The FSRs were developed after the functional requirements were translated into flow charts. The flow charts were then programmed into the PDP-11 computer. During the subsequent operation of the electric thrust subsystem, the FSRs were verified, corrected and refined.

The functional subroutines developed to meet identified mission requirements are:

(1) FSR1: thrust subsystem turn-on.

(2) FSR2: monitoring the performance of a thruster/power-conditioner set.

(3) FSR3: thrust level control.

(4) FSR4: dummy load checkout.

(5) FSR5: forming a thruster/power-conditioner set by designating the elements.

(6) FSR6: forming a specified number of thruster/power-conditioner sets from the elements available.

(7) FSR7: power margin measurement.

(8) FSR8: operation at a reduced thrust level.

The details on the individual FSRs are presented in Subsection 5.

These major functional subroutines are linked together and form a closed-loop servo system that operates entirely automatically (Fig. 51). The subsystem, once started, operates without need for any intervention; the level of thrust is adjusted according to a stored power profile, as is the number of operating sets. In the case of failure or out-of-limit operation, the controller initiates emergency corrective actions. These will remain in effect until overriding commands are received from the ground station.

The controller program is designed around a small real-time executive that keeps time and coordinates commands and functional subroutines. The controller's executive has additional message printout functions.

Commands can start or stop an FSR. Commands are of two types, immediate and timetable commands. Timetable commands are stored together with the absolute time at which they are to be executed. At the proper time, they are decoded and implemented by the executive.

An FSR, once started by a teletype command or by another FSR, will continue automatically to its conclusion. FSRs can remain operational for hours or for the entire duration of the mission. They are usually sequences composed of many segments or many iterations of a few segments.

The main elements of a typical FSR segment are: (1) reading telemetry feedback data, (2) comparing these with expected data, and (3) deciding whether to proceed, or declare a malfunction or to try again later.
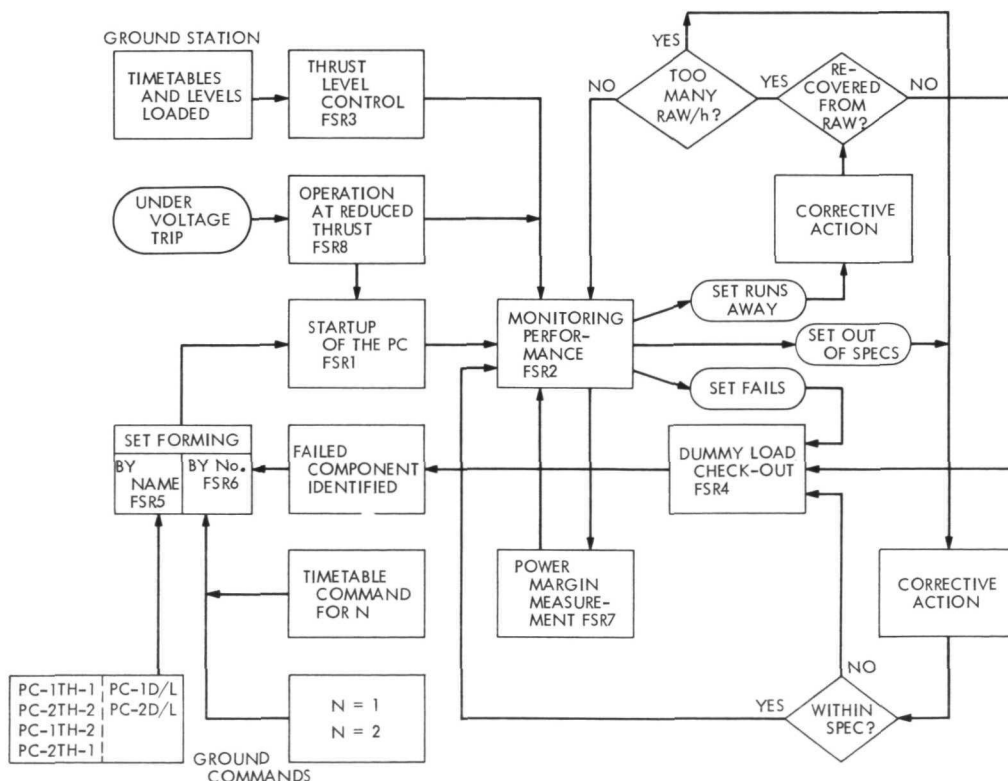

Fig. 51. SEPST III software flow diagram

Proceeding generally means initiating another segment of the FSR or sending a control signal to the subsystem, such as a pulse, a logic level, or a reference adjustment. Declaring a malfunction triggers a sequence of events that resets the FSR used to its starting point and starts another FSR that tries to correct the malfunction.

Trying again later is accomplished by use of the preset clocks. The preset clocks are software interval timers. Each clock consists of two words: one contains the number of time units being counted and the other contains the address to which the program should jump when the count is finished.

Interval timing is a requirement because in some cases a precise interval is of intrinsic importance, and because it can be used to reduce the "duty cycle" of the particular FSR and, consequently, the load on the computer.

c. Operation. The normal mode of operation of the SEP CCSS is fully automatic. Operator intervention by keyboard commands is permitted but not required. A semiautomatic mode is available in which the controller pauses at certain critical checkpoints waiting for an operator decision whether or not to proceed. Also, a manual mode is provided that switches control capability from the computer to a manual control panel. The panel provides control pulses and the reference voltages. The operator relies on facility instrumentation for feedback in this mode of operation. The manual mode makes it possible to perform maintenance of the computer without halting the rest of the subsystem operation.

d. Interfaces. The operator communicates with the controller by keying in four-digit discrete or quantitative commands on the keyboard of the ASR-35 teletype. He can make the commands effective immediately or at some later time. A four-character message with a time tag is printed out to record the occurrence of any significant event. Telemetry data printouts and diagnostic printouts are also available.

The controller sends each power conditioner five pulsed commands sequencing its turn-on and turn-off. Each of these commands is of 28-V amplitude and 150-ms duration. Two reference levels that regulate the power demand of the thrusters, the arc- and beam-current references, are supplied to each of the two power conditioners in the form of analog 0- to 5-V signals. These can be adjusted in 2.5-mV steps. The controller receives 0- to 5-V analog telemetry data from each power conditioner. These data define the ten individual power conditioner outputs. Also, a PC-OFF, 5-V status signal is available.

The CCSS sends the switching matrix an enabling signal and a switching command. The enabling signal is a relay closure that makes 28-V solenoid power available to the switching matrix. The switching command, which identifies the required thruster power-conditioner set, is a 6-bit, parallel, 2-s pulse produced by the operation of six relays. The switching matrix sends the controller eight discrete status indications, one for each possible set combination.

The direct interface between the SEP controller and the TVC mechanism is limited to the controller supplying information as to which thrusters are turned on. The TVC advises the controller in the case where reaction jet control has been applied. The TVC has its own access to the power conditioner thrust level telemetry.

4. Integration phase. The initial phase of the integration consisted of installing the PDP-11 and ASR 35 in the test facility, interconnecting all the interfaces (Fig. 1), and loading the assembled programs into the computer. A PDP-10 computer was used to accelerate the assembly of the programs. In the following phase the individual functional subroutines were debugged, using the semiautomatic mode of operation. During this phase several changes and additions to the control program requirements were identified and implemented; the flexibility of the software approach proved advantageous in making the required program modifications. For example:

(1) A vaporizer cycling sequence (described in Subsection 5) was added to FSR1 to eliminate the problems caused by condensation of mercury during startup.

(2) The startup of an already warm thruster was accelerated by eliminating unnecessary delays.

(3) The feedback magnitudes of currents of the arc power supply were redefined to distinguish between the preheating of the body of the thruster and the actual arc.

(4) Comparison of the arc current to the arc reference level, as one of the indications of a properly operating thruster, was abandoned as not practical.

(5) A number of threshold levels and timing intervals were modified.

After all the FSRs were declared operational, the interconnecting links between the individual FSRs were established and closed-loop operation was evaluated. "Out-of-spec" conditions were artificially created and the

predicted responses of the controller were verified. A 1500-h functional test run of the thrust subsystem, which followed, provided the opportunity to observe subsystem behavior on a day-to-day basis.

A good portion of the integration period was devoted to overcoming problems related to the noise environment of the test setup. (The term "noise" is meant to include all undesirable transient and interference effects.) The noise environment in the laboratory was high. Large, electrical transients on ground lines and on signal lines were caused by arcing of the thruster or by switching of the various pumps and support equipment associated with the facility. The noise was not unexpected, and measures were taken in the initial design to preclude direct damage to components by power surges and to generally eliminate known noise where possible. Therefore, the general approach during the integration period was to eliminate the effects of the noise, rather than the noise itself. Some specific observations and the corrective actions taken are described below.

Initially, the technique of reading the analog telemetry data consisted of a single level measurement, within a window of a few microseconds duration. It was found that erroneous readings were recorded due to presence of ac ripple and noise. Measurements indicated that interfering pulses could last up to 10 μs. The sampling technique was then modified and an average of eight readings, taken within a period of 40 ms, utilized.

Although the computer itself was isolated from noise, the interface flip-flop registers were found to be susceptible to some of the larger transients, resulting in spurious changes in state of some of the flip-flops. These changes were especially undesirable when they occurred in the registers servicing the digital to analog converters, which supplied the reference levels to the power conditioners. Variations in reference levels, if uncorrected, could cause system failure. Consequently, the control program was modified and these registers are now refreshed every second from core memory, which is not susceptible to transients as are the flip-flops.

Crosstalk between signals on adjacent wires in the long, flat cable used between interface registers and the controller caused some errors in reading data. The crosstalk proved to be of short duration as it existed for only 200 ns after gating or addressing a register. The problem was solved by increasing the delay between the time of addressing a register and the time of reading the register's data into the computer.

The computer itself seemed only slightly susceptible to the high noise spikes, but the program stopped about once every 100 h. Because the program was otherwise intact and no damage to the computer was ever discovered, a hardware timing device and some supporting software were added to automatically restart it. This permitted unattended operation of the electric thrust subsystem.

As the noise environment of the space vehicle has not yet been defined, the above remedies will not necessarily apply to a flight application. However, the test experience gave considerable insight into the kinds of problems that must be anticipated in designing a subsystem control program for flight application. Studies, now in progress at JPL, will help determine the electromagnetic compatibility requirements of the SEP CCSS interface on a vehicle and define the degree to which the experiences gained during this phase of the program can usefully be applied to flight technology.

5. Functional subroutine details.

a. Starting of a set, FSR1. This algorithm takes care of starting the specified thruster-power conditioner set. The routine may be started by a ground command or by a signal generated within the computer. Two cases are considered: (1) starting a cold set, i.e., a set that was dormant for more than 15 min., and (2) restarting a temporarily turned-off set, i.e., a set that was inactive for less than 15 min.

Starting of a cold set: initial conditions. The power conditioner (PC) is off, and the PC panel is maintained at $-45\,^{\circ}$C or above.

Starting of a cold set: turn-on sequence.

(1) The computer issues a command to the temperature controller, which raises the temperature of the PC panel to 0°C, as required.

(2) When the temperature attains 0°C level and the PC is off, the turn-on cycle starts. The beam reference level is set to minimum, and the arc reference to the level that will produce a 3.5-A preheating current.

(3) The ON1 command is generated by computer. This initiates the preheating of the main vaporizer (manifold, isolator, and feedline), the tip of the hollow cathode, and the backplate of the thruster. Most of the preheating power comes from the arc power supply that feeds the heating power through

a thermal switch (Klixon). The telemetry Table 15*
requirements must be satisfied.

(4) Upon completion of the warm-up cycle, when the
temperature of the body of the thruster reaches
175°C, the Klixon opens and the current supplied
by the arc power supply is interrupted.

(5) The computer generates the ON2 command, which
starts heating the cathode vaporizer, the main
vaporizer, and the neutralizer. The telemetry Table
16 requirements should then be satisfied.

(6) The computer waits for the arc to strike. This may
take up to 30 min., during which period the Klixon
may close again to rewarm the thruster.

(7) When the arc ignites and the arc current attains a
4-A level, the arc reference is automatically raised
to produce a 6-A arc current, and, for 30 min., the
main vaporizer is cycled on and off to burn out
the excess mercury inside the thruster. The ON2
command turns the vaporizer on; the OFF1 com-
mand turns it off.

(8) After cycling has been terminated, the ON3 com-
mand is issued by computer. The command turns
on the rest of the PC's supplies and thrust is in-
itiated. A 15-min. delay is allowed for the operation
to stabilize at the minimum power level. After this
delay, the control of the reference levels of this set
is transferred to the power profile control (FSR3),
while the responsibility for monitoring the per-
formance of the set is assigned to FSR2.

Restarting of a warm set: the initial conditions. The
power conditioner (PC) has been off for less than 15 min.

Restarting of a warm set: turn-on sequence. The turn-
on sequence is faster because some of the delays are
eliminated. Approximately 30 min. are required for the
set to become operational. The turn-on sequence is as
follows:

(1) PC panel temperature is above 0°C, thus ON1
command is automatically issued at once and telem-
etry data confirm that the thruster is hot. Thus
Table 15 is bypassed and no delay is encountered.

(2) The computer generates the ON2 command and
telemetry data are checked against Table 16. When
the arc strikes and the 4-A level is reached, the arc
reference is raised to produce 6-A current. Cycling

of the main vaporizer is initiated, but it is limited
to a 15-min. duration.

(3) The computer generates the ON3 command and,
after 15 min., FSR2 is started and power profile
control, as per FSR3, established.

b. Monitoring the performance of a set FSR2. The
purpose of this subroutine is to detect and initiate the
required corrective steps when the set (1) runs away, or
(2) operates out of limits or fails.

Runaway. The runaway (RAW, Fig. 51) of the thruster
is characterized by a temperature rise in the main vapor-
izer, a decrease of beam current and an increase of
accelerator current. When a runaway condition is de-
tected, the following procedure is initiated.

(1) The computer turns off the main vaporizer, causing
the accelerator current to decrease.

(2) After the accelerator current has dropped below
the specified level, the main vaporizer is restarted.

(3) The runaway counter registers the occurrence of
the runaway and the set is declared operational.

When more than two runaways per hour are recorded,
the following additional steps are taken to reduce the
frequency of runaways.

(1) If the set is not operating at the maximum arc ref-
erence, the computer steps up the arc reference
one step at a time, for a maximum of three times
until the frequency of runaways decreases.

(2) If the arc current cannot be raised any more, the
computer looks for another good thruster and, if
such is available, reconnects the PC to that thruster.

(3) If no other thruster qualifies, the computer begins
to reduce the beam current of the malfunctioning
set in an attempt to save the set even if it results
in operation at reduced thrust level.

Should all the above measures fail to eliminate the
runaways, the set is declared damaged, is turned off,
and is directed into FSR4 for dummy load checkout of
that PC. It should be noted that:

(1) The higher level of arc current raises the power
consumption, and continued operation in such a
mode is not desirable.

(2) The lower level of beam current reduces the thrust
level and thus changes the flight path. This makes
continued operation in such a mode undesirable.

---

*All the table requirements are listed in Subsection 6.

At the next scheduled change of reference levels, as defined by the flight plan, the computer restores the scheduled arc and beam references on the assumption that the set has recovered from the temporary abnormal conditions. Should this not be the case, a temporary deviation from the flight plan will once again be generated.

Out of limits or failure. Three electrical parameters are considered critical: beam current, screen voltage, and accelerator voltage. Screen or accelerator voltages lower than the specified minimum are considered as a set failure and the failing set is turned off and directed into FSR4 for dummy load checkout of the PC. When only the beam current is out of limit, the computer overrides the power profile setting of the arc reference and raises the arc current by one step. This is generally instrumental in bringing the beam current within the specification. Should the beam current fail to come within the specified limits, the arc current can be raised two more times.

When the out-of-limit condition for beam current continues, the computer looks for another good thruster, or, if such a one is not available, it starts reducing the beam current on the existing set. The original reference levels prescribed by the power profile are restored at the time of the scheduled change of reference levels.

c. Thrust level control, FSR3. The output characteristics of the solar array can be predicted quite accurately in terms of its distance from and inclination toward the sun. The normal degradation of the solar array is also predictable in terms of mission time (Ref. 1). The maximum power available can be translated into the profile of thrust, which should be closely followed to keep the vehicle on its projected course. The thrust level depends upon the level of beam current, which in turn is controlled by the beam reference. The arc control is exercised by the arc reference. The arc-reference level is slaved to the beam-reference level by the functional relationship represented by Fig. 52.

The FSR3 algorithm is responsible for adjusting the levels of the individual references by specified values at a designated time. The desired profile can be loaded into the SEP computer either before or after launch. It can be modified or completely rewritten by ground commands at any time. The procedure of loading the power profile into the memory consists of:

(1) Defining the initial and final number of sets, also specifying when the number of working sets should be modified.
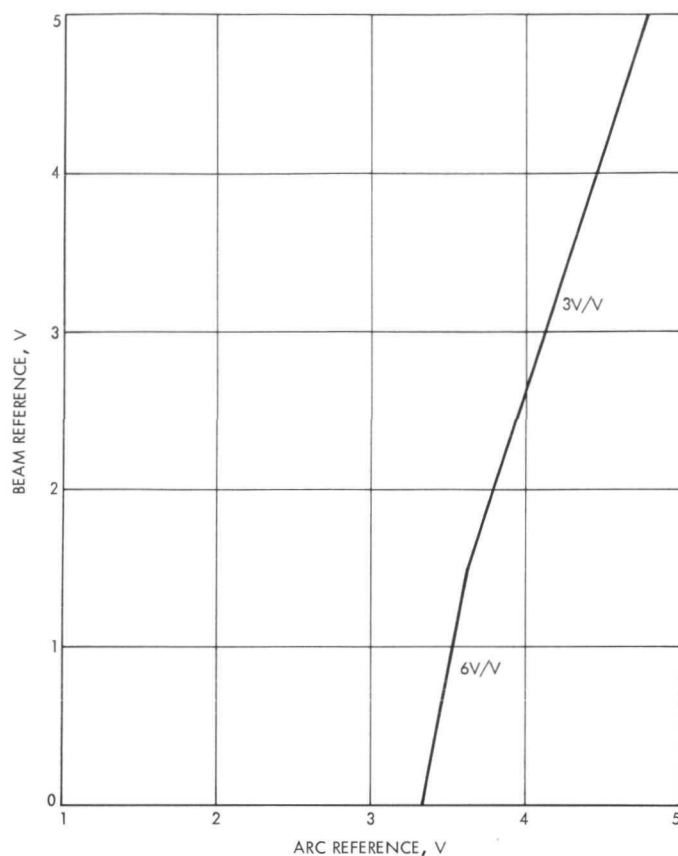
Fig. 52. Relationship between input references

(2) Defining the size of steps of references of arc and beam currents. The size of the steps is common to all power conditioners.

(3) Defining the initial reference levels for all power conditioners. The separate levels for each power conditioner can be specified.

(4) Specifying the time intervals for incrementing or decrementing the individual reference levels.

It should be noted that at the lower thrust level the slope of the beam/arc functional relationship (Fig. 52) increases. Thus, for the same size of the step of beam reference, the size of the step of the arc reference must be reduced. The algorithm provides the means of doing this.

d. Dummy load checkout, FSR4. The outputs of each power conditioner are short-circuit proof. This means that the individual power supplies will continue to operate without damage if the output is short circuited. An exception to this rule is the screen power supply. A short circuit across the output of this supply will cause an

automatic shutdown of the entire power conditioner. The above characteristics were utilized in deriving the procedure for inflight dummy load (D/L) checkout. The checkout is performed when a power conditioner-thruster set fails to turn on during the FSR1, or when the specified requirements of the FSR2 cannot be satisfied. The suspected power conditioner is then tested in the D/L position.

The checkout is accomplished in two steps that permit the inspection of all open- and short-circuited outputs.

The screen supply is checked out on a resistive, 90% load. To reduce the weight of the screen load to a bare minimum, the checkout time is limited to approximately 140 ms. The size of the load bank drops from 2000 to a 280 J level, with a total weight of 0.03 kg.

The telemetry data that were recorded during the D/L checkout are compared with Tables 18 and 19 of acceptable data. The nature of trouble either inside the power conditioner or the associated thruster, is defined.

The subroutine FSR4 is started by either a ground or computer command when a set failure is reported. Two variants of FSR4 will be reviewed.

D/L test by ground command. Two commands are provided: one for D/L testing of PC-1, and the other for D/L testing of PC-2. Each command initiates the following sequence of events:

(1) All working PCs are turned off.

(2) The specified PC-X is reconnected to D/L.

(3) The panel temperature of PC-X is checked. If it is below 0°C, the preheating of the panel is ordered.

(4) When the temperature of the panel is above 0°C, the ON1 and ON2 commands are sent to PC-X by computer.

(5) The references for PC-X are set to specified levels and the computer issues the ON3 command.

(6) The first set of parameters as per Table 18 are measured.

(7) The computer energizes D/L relays and after 100 ms the second set or readings, as listed in Table 19, is taken.

(8) The routine is ended by turning off PC-X 40 ms later. The complete telemetry data, as per Tables 18 and 19, are subsequently printed out by the teletype.

D/L test by computer command. The test sequence is as follows:

(1) All working PCs are turned off.

(2) The specified PC-X is reconnected to D/L.

(3) The panel temperature of PC-X is checked and if below 0°C the preheating of the panel is ordered.

(4) When the temperature of the panel is above 0°C, the ON1 and ON2 commands are sent to PC-X by the computer.

(5) The references for PC-X are set to specified levels and the computer issues the ON3 command.

(6) The first set of parameters, as per Table 18, are measured; 40 s are allowed for the telemetry outputs satisfying Table 2A of Ref. 69.

(7) The computer energizes D/L relays and after 100 ms the second set of readings, as listed in Table 19, is taken.

(8) PC-X is turned off.

(9) The telemetry data are analyzed and the computer defines whether the power conditioner or the thruster is damaged. The complete telemetry data are printed out.

(10) The FSR6 is initiated (Fig. 51), and a new, working set automatically replaces the damaged one.

e. Forming of set, FSR5 and FSR6. Two methods of forming a set are available: (a) by designation of the set(s), or (b) by specifying the number of sets to be formed.

Designating the set, FSR5. This algorithm is responsible for interconnecting the thrusters and power conditioners in such a way as to form specified sets, irrespective of the initial status of the interconnections. The specified set will be defined as PC-X and TH-Y PC for power conditioner, TH for thruster. The routine is started from the ground by a command that defines the desired set by name, e.g., set A consists of PC-1 and TH-2. The following sequence of events results:

(1) The computer checks if both PC-X and TH-Y are in working order.

(2) Both PCs are commanded off.

(3) By means of the computer-generated commands, the existing interconnections of the switching matrix are modified and PC-X—TH-Y set is formed.

(4) PC-X is started by FSR1.

(5) The performance of the PC-X—TH-Y set is monitored (FSR2).

Specifying number of sets, FSR6. This algorithm is responsible for manipulating the interconnections of thrusters and PCs in such a way as to provide the vehicle with the required number of working sets that are compatible with the requirements of the thrust vector control mechanism.

FSR6 can be started by a ground command or computer command. N = 1 or N = 2 set (Fig. 51) can be requested by a signal from FSR4. The following sequence of events results:

(1) The computer checks if the specified number of PCs and thrusters is available.

(2) The computer checks how many of the existing sets can be used.

(3) The computer defines new sets that are needed.

(4) The new sets are formed (FSR5).

(5) The required number of sets is started (FSR1).

(6) The operating sets are placed under flight profile control (FSR3).

(7) Performance of all operating sets is monitored (FSR2).

f. Power margin measurements, FSR7. The power margin is defined as the percentage difference between the maximum available power and the actual power being consumed. As the exact prediction of the degree of degradation of the solar source is not possible, the power margin that exists may vary between 18% and 0% (Ref. 6).

Guidance and navigation may be improved by knowing the actual size of the margin. It is considered desirable to periodically monitor the solar source to determine the value of the margin available. The candidate concept for an accurate peak power measurement has been proposed (Ref. 6) and the computer FSR7 subroutine that controls the measurement has been developed.

The subroutine may be started by a command from the ground, or from FSR3 as scheduled by the flight plan. A few minutes are required to define the margin, during which time the subsystem operates at a minimum thrust level.

The following sequence of events then takes place:

(1) The actual power level, P_A, at which the subsystem operates is determined by measurement.

(2) Thrust is reduced to the minimum reference level.

(3) The peak power level, P_P, of the solar source is measured.

(4) Power margin, $m = (P_P - P_A)/P_P$, is computed.

(5) Thrust level is restored to the original value as specified by FSR3.

g. Operation at a reduced thrust level, FSR8. In the case where the power margin diminishes to zero, the solar source goes into a current-limited mode of operation; the source voltage collapses, and the power conditioners are tripped by the undervoltage sensors. Operation at a reduced, unscheduled thrust level must be initiated.

To restart the subsystem, the computer:

(1) Measures the peak power of the source.

(2) Determines whether operation with the specified number of sets is feasible.

(3) Modifies the reference levels as defined by the thrust-level profile stored in FSR3 to operate as close to the scheduled power level as possible, while retaining a power margin of at least 1%. The designated sets are then restarted (FSR1). Operation at a reduced thrust level continues until the next communication with the ground station.

6. Computer tables. Table 15 is used within the FSR1, the functional subroutine for startup of a set. The telemetry (TM) data are compared to the requirements of this table at the beginning of the thruster warmup cycle and after the ON1 command has been issued. To satisfy the requirements, all the incoming TM levels must be higher than those specified.

Table 15. FSR1 acceptance levels after the ON1 command

Power supply No.	Power supply name	TM of output voltage, V	TM of output current, V
1	Magnet	—	2
4	Arc	—	1.8
8	Neutralizer keeper	4.5	—
9	Cathode tip heater	—	1.0
10	Cathode keeper	2	—

Table 16 is used within FSR1, the functional subroutine for startup of a set. The TM data are compared to the requirements of this table, after the ON2 command has been issued. To satisfy the requirements, all the incoming TM levels must be higher than those specified.

Table 16. FSR1 acceptance levels after the ON2 command

Power supply No.	Power supply name	TM of output current, V
2	Main vaporizer	2
3	Cathode vaporizer	2
7	Neutralizer vaporizer	2

Table 17 is used within the FSR1, the functional subroutine for startup of a set. The TM data are compared to the requirements of this table after the ON3 command has been issued and the actual beam and arc currents have reached the reference levels. To satisfy the requirements, the incoming TM levels must be higher than those specified.

Table 17. FSR1 acceptance levels after the ON3 command

Power supply No.	Power supply name	TM of output voltage, V
5	Screen	3.4
6	Accelerator	2.5

Table 18 is used within the FSR2, the functional subroutine for checking out the PC on dummy load (D/L). The TM data are compared to the requirements of this table after PC has been connected to the D/L and the ON3 commands issued. To satisfy the requirements, all the incoming TM levels must be higher than those specified.

Table 18. FSR2 acceptance levels after ON3 command

Power supply No.	Power supply name	TM of output voltage, V	TM of output current, V
1	Magnet	—	2.5
2	Main vaporizer	—	2.5
3	Cathode vaporizer	—	2.5
4	Arc	2.5	—
5	Screen	2.5	—
6	Accelerator	2.5	—
7	Neutral heater	—	2.5
8	Neutralizer keeper	2.5	—
9	Cathode tip heater	—	2.5
10	Cathode keeper	2.5	—

Table 19 is used within the FSR2, the functional subroutine for checking out the PC on dummy load (D/L). The TM data are compared to the requirements of this table, after the terminations of dc outputs have been modified by actuating the D/L relays. To satisfy the requirements, all the incoming TM levels must be higher than those specified.

Table 19. FSR2 acceptance levels after D/L relay actuation

Power supply No.	Power supply name	TM of output voltage, V	TM of output current, V
1	Magnet	—	2.5
4	Arc	—	2.5
5	Screen	3	3
6	Accelerator	2.5	—
8	Neutralizer keeper	—	2.5
10	Cathode keeper	—	2.5

III. SEPST III System Test Setup and Instrumentation

TSS testing required a substantial amount of special equipment, in addition to the basic TSS elements, as illustrated in Fig. 53. The TSS elements that directly interface the instrumentation elements are also shown in the figure.

For initial integration and checkout purposes, laboratory-type power supplies were provided. One set per thruster was available. These laboratory supplies duplicated the PC outputs in terms of power level, power type (5-kHz square wave or dc), and control-loop operation. Remote control of all supplies from the experiment control center (ECC) was provided. The ECC is shown in Fig. 54.

The laboratory supply and PC (switch) outputs terminated in the "transducer box." Patching cables connected to a given thruster through transducers could be connected to either a PC or laboratory supply set. Transducers for both dc (magnetic amplifier type) and ac (rms-dc) currents and voltages were used.

Data signals from: (1) thruster current and voltage transducers, (2) PC input power transducers, (3) PC telemetry, (4) the temperature-reference junction, and (5) pressure transducers were collected at the data system patch panels. The data was then distributed to other locations as illustrated in Fig. 53.
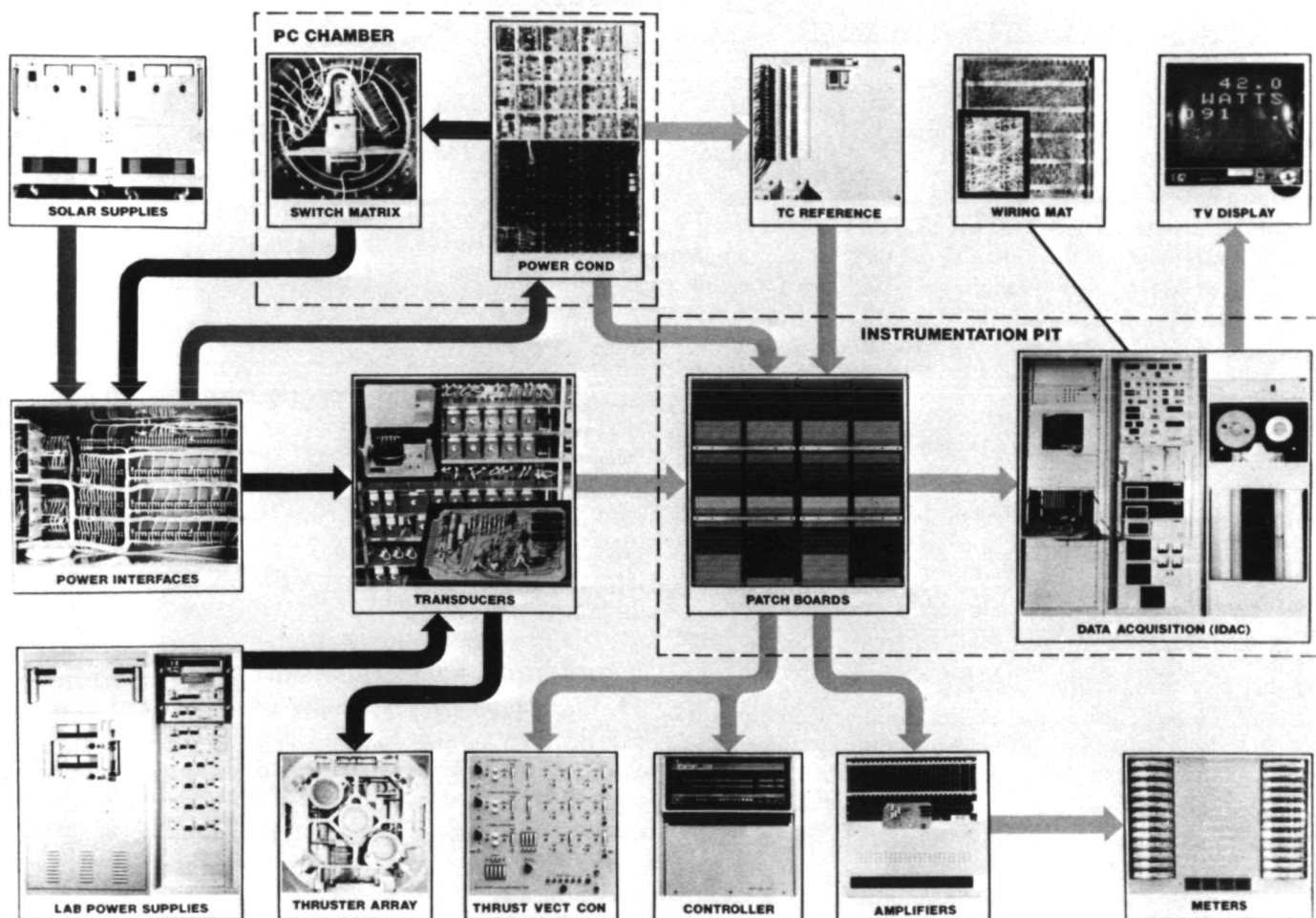
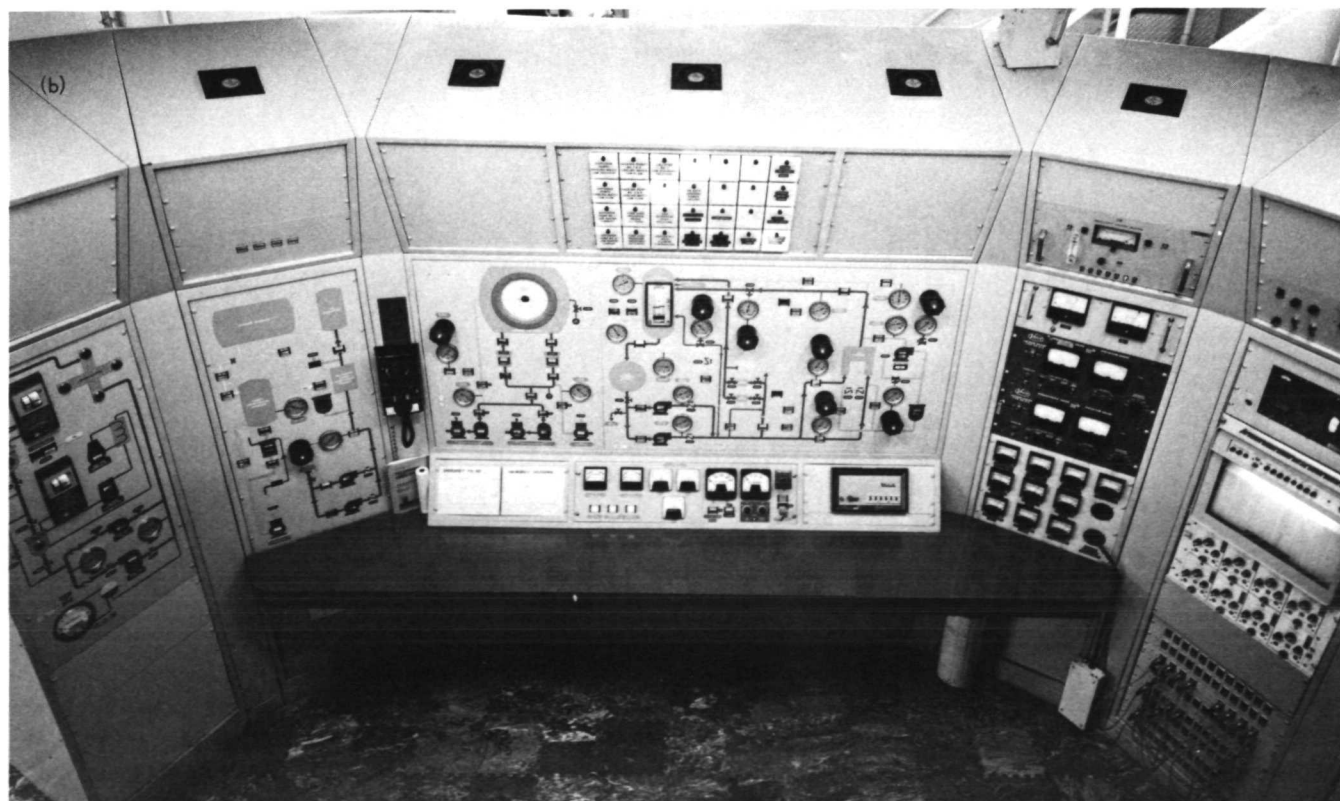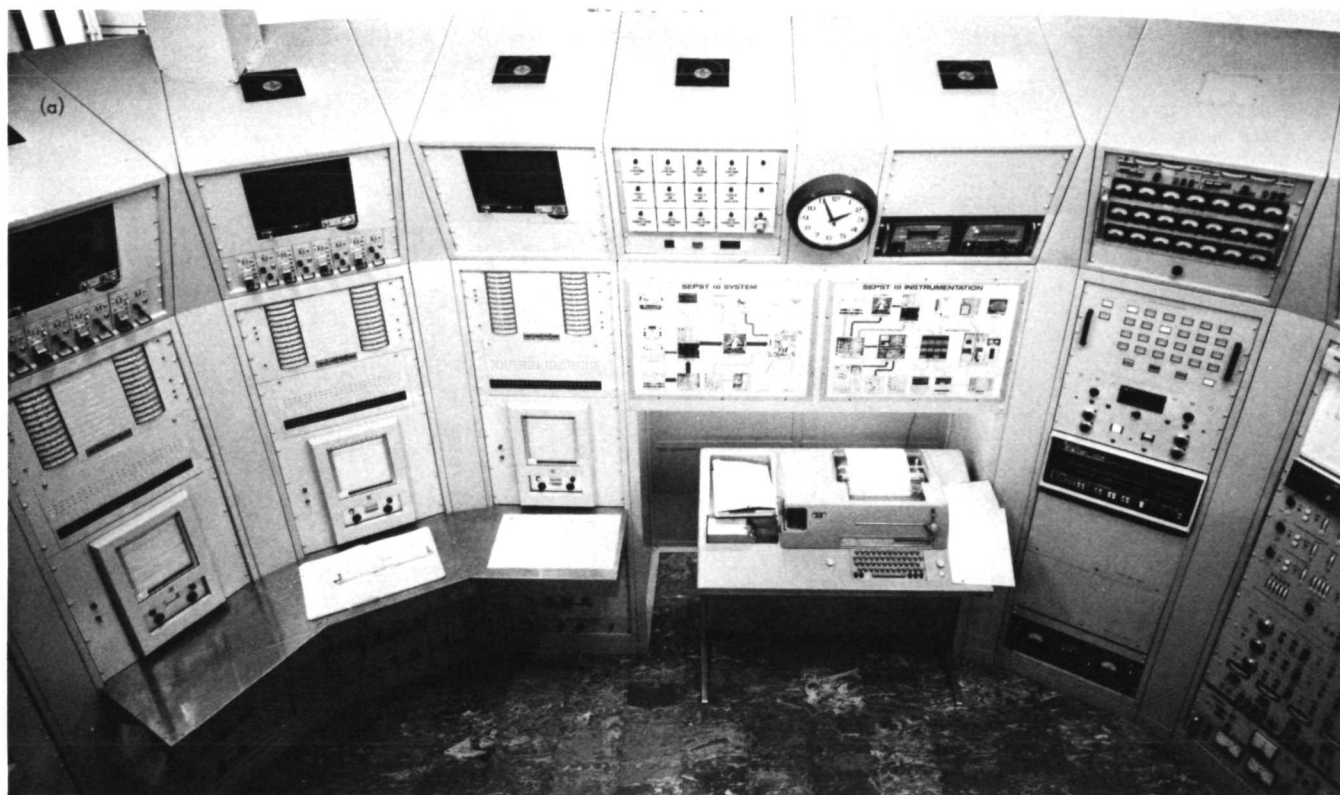Fig. 53. SEPST III instrumentation block diagram

Fig. 54. Experimental control console: (a) thrust subsystem control; (b) facility control

Fig. 55. IDAC system and low-voltage power supplies

Presently all transducer and temperature data are put into a data recording system (Fig. 55) (IDAC, meaning integrated data acquisition and control). The data are multiplexed using a programmable scanning sequence, converted into engineering units, and are stored on magnetic tape and/or printed out on paper tape. Any IDAC channel can be displayed on any of five monitors, three of which are in the ECC. The data are in engineering units and the display is updated each time the multiplexer is scanned. Six-hundred data channels are available. The IDAC system is also designed to check limits on data and indicate failures.

During testing, PC telemetry data (16 channels per PC) in the form of 0 to 5 Vdc analog signals were monitored by the computer (for TSS control) and were recorded by the teletype. Signal buffer amplifiers, required to interface the IDAC, were not available and telemetry data was not recorded by the IDAC system. Eight selected telemetry channels were recorded continuously during testing on a brush recorder in the ECC.

Thruster current and voltage transducer data were sent through amplifiers to meters in the ECC. Since the transducers were in lines going directly to the thruster,

the meters indicated thruster conditions with either PC or laboratory supply operation.

Data was also supplied to the TVC electronics to indicate the operating thrusters and individual thruster ion-beam currents. As noted previously, this information was an input to the vehicle dynamics analog computer program.

The physical layout of the test setup is shown in Fig. 56. The previously described TSS and instrumentation elements were located as shown. Most interconnecting wiring is omitted.

The main (2.3- × 4.6-m) and PC (1- × 2-m) vacuum chambers are connected by a gate valve but both chambers have conventional oil diffusion pump systems and have liquid-nitrogen-cooled surfaces. The LN$_2$-cooled panel in the PC chamber provides the radiation sink for PC heat rejection. All cabling that connects to the elements in the PC chamber (PCs and SMX) passes through Deutsch bulkhead-type connectors mounted in the "feedthrough spool." This includes high-voltage power, low-voltage power, signals (commands, telemetry, and SMX data) and thermocouples. Figure 57 shows an end
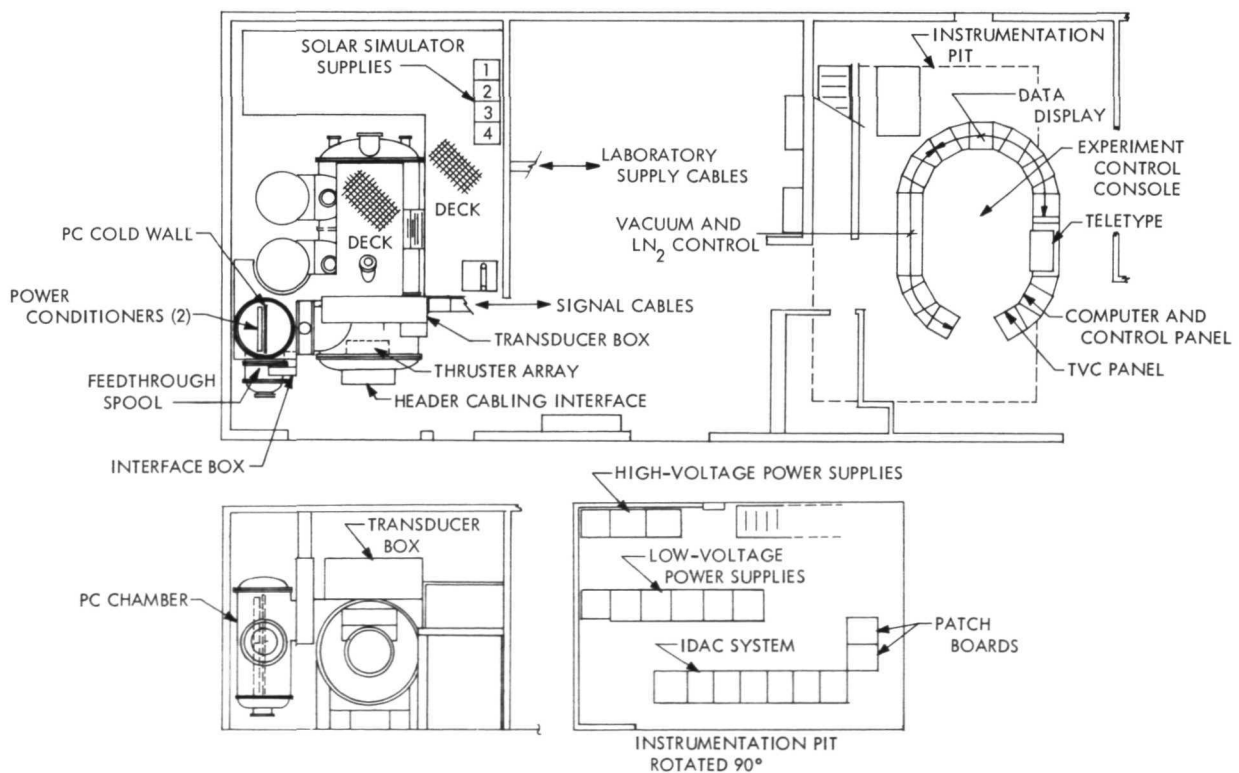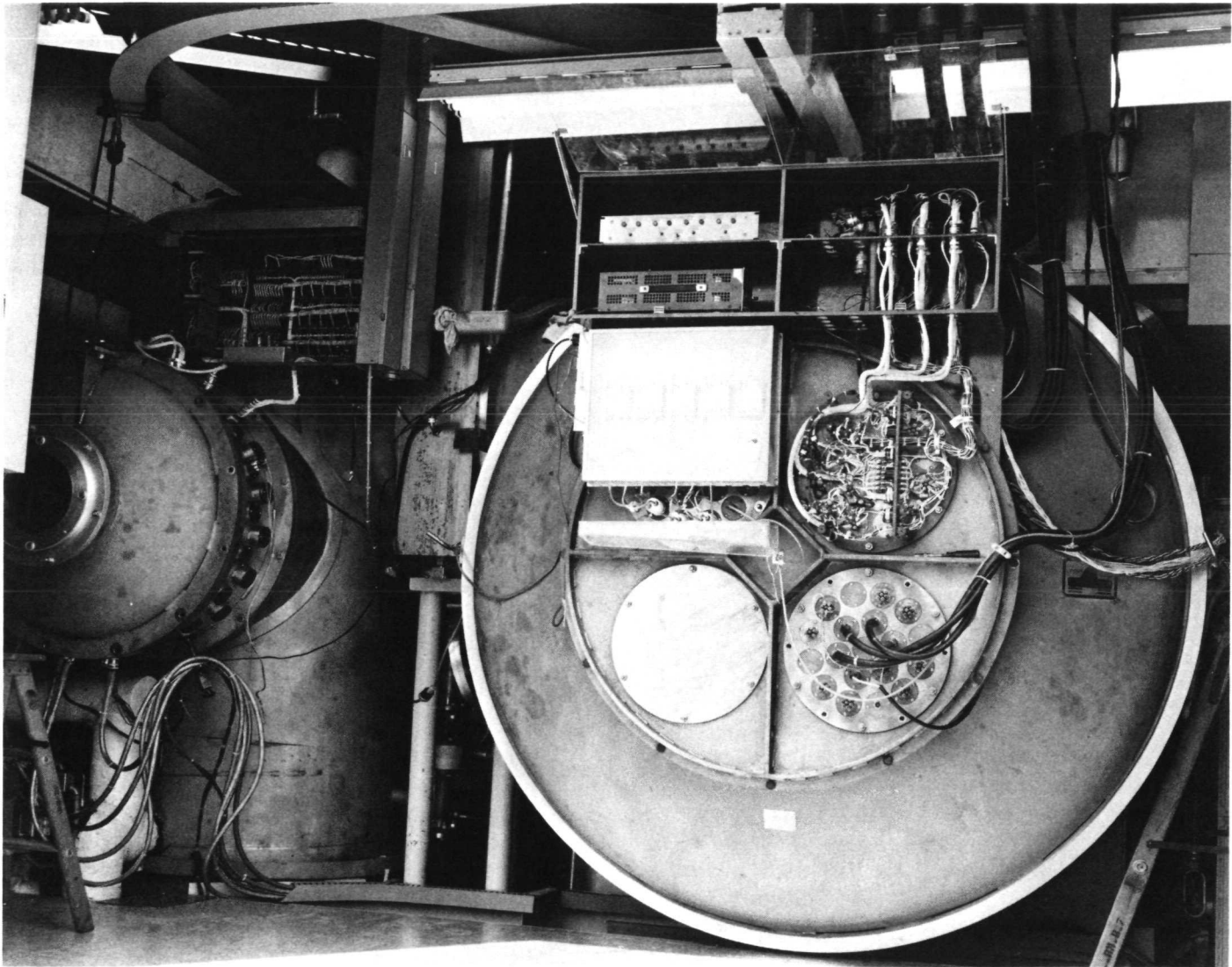

Fig. 56. Test system layout

Fig. 57. Vacuum header

view of the tanks, including the heater wiring and interfaces. Vacuum system controls are shown in Fig. 54.

Power outputs (from PCs or laboratory supplies) for the thrusters go to the transducer box and are connected to an interface panel at the main chamber header. Deutsch connectors are used to provide easy header removal. The thruster side of the interface panel is hardwired to conventional ceramic/metal-seal vacuum feedthroughs. Cabling from the main header to the thruster array uses Teflon-insulated ribbon-type cable, to meet the flexibility requirements of the TVC, and is terminated at the thrusters in Deutsch connectors. Additional information on the ribbon cable design is available in Ref. 45.

As Fig. 56 indicates, the TSS CCSS computer, TVCE, manual command panel, and switch command panel are located in the ECC. The IDAC patchboards (Fig. 58) and lab power supplies are located in a room directly below the ECC. The vacuum and LN$_2$ systems are also

Fig. 58. IDAC system patch panels

controlled from the ECC, resulting in control of the entire test from one location.

IV. SEPST III System Testing

A. General

The primary objective of the SEPST III testing was to demonstrate the operation of the functionally-complete TSS. This demonstration took the form of a 1500-h test during which two PC-thruster sets were operated simultaneously. A third thruster, provided for redundancy, was operated for a portion of the 1500 h. Operation was controlled by the CCSS computer and the TVC system was activated periodically. However, before the 1500-h test could be performed, a number of pretest and operating procedures had to be developed. These procedures are test results in the sense that similar procedures will be required for a flight TSS. In presenting the test results, the procedural aspects are described first, followed by the TVC testing and the 1500-h test results. Then, supplementary tests, integration problems and failures will be described.

B. Pretest and Operating Procedures

1. **Pretest operations.** The primary pretest operations began after both the main and PC chambers were pumped to high vacuum. After the PC chamber reached 10^{-5} torr, full PC thermal-control heater power (180 W per PC using thirty resistive heaters) was turned on. Without cooling the PC chamber "cold wall," the PC temperatures stabilized at about 50°C. This condition was maintained for about 12 h. The cold wall was then cooled with LN$_2$, with the heaters at full power. The typical PC temperature history during the cold wall cooling is shown in Fig. 59. The thirty heater elements per PC were not distributed uniformly by area because of mounting constraints, resulting in the nonsymmetric temperature distribution indicated by the two curves. The PC temperature was then cycled between −20°C and +30°C by periodically cycling the heaters and LN$_2$. The cycling was intended to remove trapped gas in electrical terminals and under tightly fastened components. Pressure bursts were generally experienced during thermal cycling in the early testing, but the bursts gradually disappeared after a few pump-down cycles. The PC chamber pressure was in the range of 1×10^{-6} to 2×10^{-6} torr after bake-out and was continuously recorded.

After this bake-out and thermal cycling period, totaling 18 to 24 h, the PCs were turned on slowly on dummy
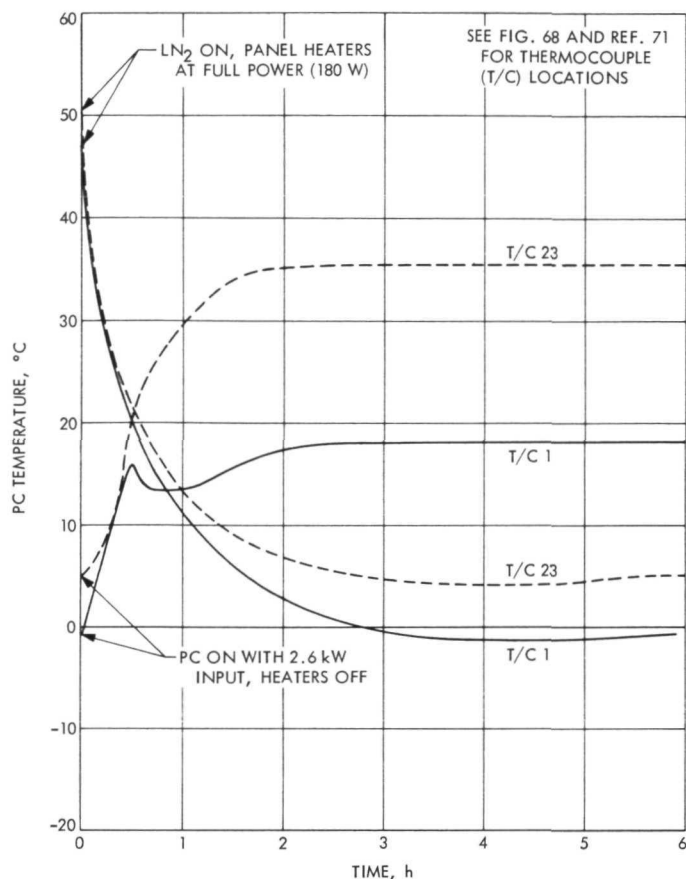
Fig. 59. Power conditioner temperature response

loads. All supplies except the screen (beam) supply were turned on first. Each of the eight screen inverters was then checked by switching on the individual inverter input power, using manual switches in the interface box (Fig. 60). The inverters were switched in one at a time with a maximum of three inverters operating (about 1200-V and 0.5-A output). Gradually, all inverters were switched in and checked at full power. This procedure required each inverter to operate at 350 to 380 W output and provided assurance that the inverters would operate well at the normal maximum 250-W condition. This pump-down and bake-out cycle was performed 10 to 15 times in the course of integration and system testing.

A thruster was checked using laboratory supplies if it had been repaired since the previous run with a PC. Otherwise, the three thrusters were assumed to be operable. The thruster array was generally in thermal vacuum (10^{-6} torr or less) for 24 h or more before starting the testing. The thrusters and thruster-array structure cooled to $-25°C$ and $-5°C$ respectively during this period of exposure to the LN$_2$-cooled chamber liner.

Except for an outgassing phase, this pretest procedure would not apply to a flight TSS.

2. Initialization. The following operations sequence was designed to produce a continuous and smooth startup. A similar sequence is expected for a flight TSS.

A TSS test is initiated by activating the CCSS computer. The computer is instructed to form two PC-thruster sets. The first choice configuration, built into the set selection subroutines (Ref. 69), uses the two corner thrusters in the combination of PC-1/TH-1 and PC-2/TH-2. If PC or thruster failures have occurred prior to forming the sets, the computer chooses the next best alternative configuration. However, with only two PCs and three thrusters, the selection is simplified over more complex arrays.

The computer then verifies that the PCs are warmer than a preselected temperature. Initially, $-18°C$ was selected as the minimum temperature for safe PC operation based on transistor characteristics. However, it was found that the PC command relays would not operate below about $-10°C$. This limitation can be corrected if necessary with available relays.

3. Thruster startup. The computer first generates the initial dc reference levels for beam current (I_{sR}) and arc current (I_{4R}). The beam-current level is set to 0.5 A (minimum power) and the arc current to 3.8 A, as determined by thruster preheat requirements; the references are set for the two PCs separately. The ON1 commands are then issued. The power supplies in each PC activated by the ON1 command are listed in Table 4.

The arc current is used to preheat the thruster from the storage temperature to minimize mercury condensation. Heaters and a thermal switch are connected in parallel with the normal arc circuit. In this preheat phase the computer checks telemetry data for the magnet current, arc current, cathode heater current, cathode keeper voltage, and neutralizer keeper voltage.

After 25 to 30 min the thermal switch opens (at about 175°C) and the arc current drops to zero. The computer detects this condition and issues the ON2 command, activating the main vaporizer, cathode vaporizer, and neutralizer heater. The computer checks these vaporizer and heater currents. The keepers ignite in about 10 min and the arc ignites about 5 min later.

When the arc current exceeds 4.0 A, the computer can distinguish the actual arc current from the preheat arc
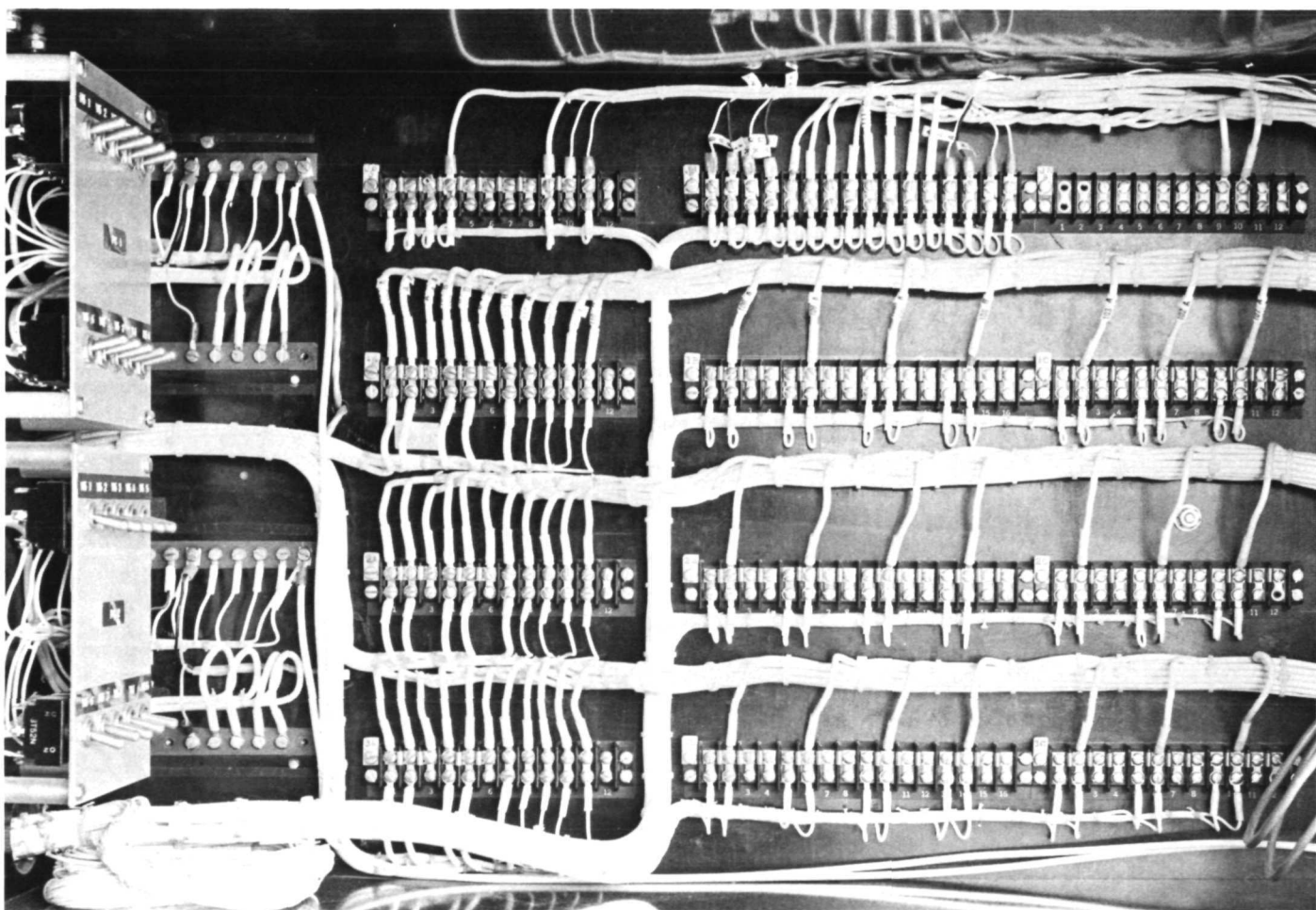
Fig. 60. Power interface box

current, and the arc reference is increased to 6.0 A. It was found that the high-voltage supplies would trip (recycle) frequently if high voltage was applied immediately after establishing the arc. This was apparently due to unstable arc conditions and the lack of thermal conditioning on the grids. This condition was accentuated when starting a thruster that had immediate prior exposure to the atmosphere. In addition, without high voltage and beam current, the main vaporizer operated at full power. This resulted in low arc voltage that turned off the cathode vaporizer. To maintain a steady arc condition with a normal cathode flowrate, the main vaporizer power was reduced. This was accomplished by cycling the main vaporizer off and on periodically, using the OFF1 (turns the main vaporizer off only) and ON2 commands respectively. A duty cycle of 50% (15 s OFF/15 s ON) was used for 15 min followed by a 33% duty cycle (30 s OFF/15 s ON) for an additional 15 min. The preheat and cycling is illustrated in Fig. 61. Note that the arc stabilizes near the end of the cycling. This time for stabilization was the basis for choosing the cycling duration of 30 min.

High voltage (beam and accelerator) is applied by the ON3 command, which is issued by the computer immediately following the cycling sequence. Using the cycling phase, the beam current is established easily. The thruster half-power conditions are maintained for 15 min. With satisfactory operation, the computer declares the thruster "operational" and proceeds to the "flight profile" routine.

C. Thruster Vector Control Testing

1. **Initial tests.** The SEPST III test configuration, insofar as it applied to thrust vector control system test, was basically that illustrated in Fig. 62. Vehicle attitude dynamics, including the engine array thrust and torque
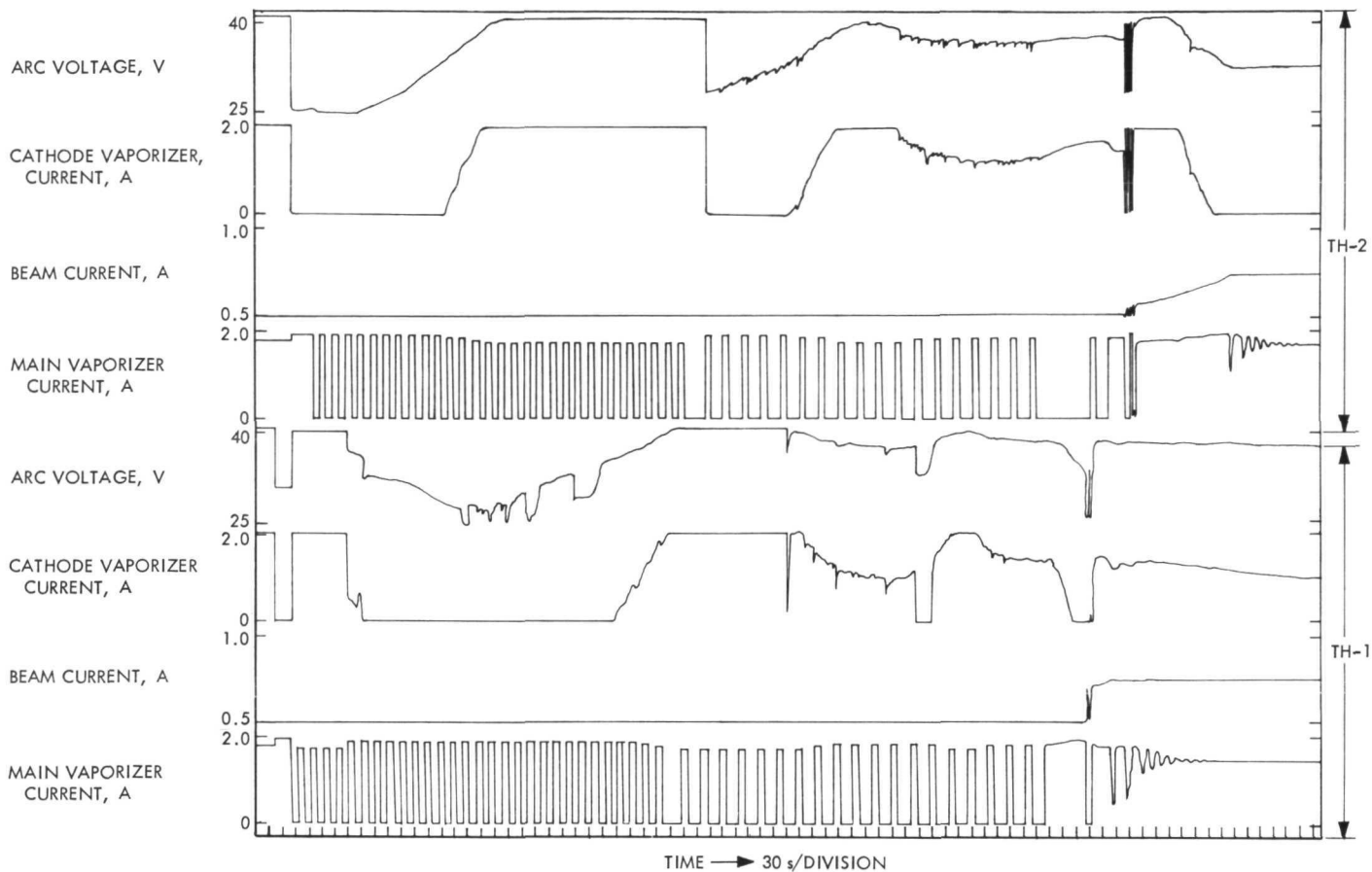
Fig. 61. Thruster startup sequence

TIME ──► 30 s/DIVISION
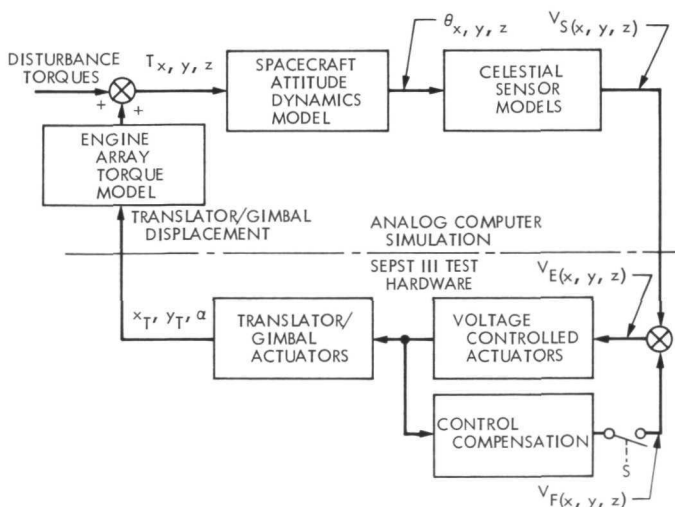
Fig. 62. SEPST III TVC test configuration

equations, and celestial sensor characteristics were modelled on an Electronic Associates, Inc., 231-R analog computer. The complete analog computer simulation program for the attitude dynamics (including scaling) is discussed in Ref. 47. The simulation required the use of 5 electronic (diode "quarter-square") multipliers, 13 integrators, 36 summing or inverting amplifiers, approximately 35 potentiometers, and a Brush Instruments' strip-chart recorder. Error voltages produced by the simulated sensors were buffered by unity-gain differential amplifiers and sent by way of JPL Central Recording System (CRS) cables to the Electric Propulsion Systems Laboratory (EPSL), the location of the ion-engine array's vacuum test chamber and associated TVC electronics. The three (X, Y, Z axes) sensor error voltages were then supplied to their respective VCO input terminals at the X-Y translator and gimbal control electronics panel (Fig. 54a).

Voltage proportional to translator X and Y displacement and outer engine gimbal angle were returned from the EPSL via buffer amplifier and CRS cable to the analog computer. Of course, in a flight situation, the two outer engine gimbal actuators would be required to deflect equally in opposite directions to realize the total available roll (Z) torque. However, the test hardware provided no mechanism for enforcing this condition and,

as a result, it was necessary to simply take one of the gimbal angles as "α" and assume that the two actuators were synchronized.

One of the first tests performed prior to the complete closed-loop, 3-axis, TVC simulation was an open-loop exercise of the translator and gimbal mechanisms. Switch S shown in Fig. 62 was opened (i.e., no feedback compensation voltages were supplied to the VCO inputs). Constant celestial sensor output voltages were sent from the analog computer to the VCOs causing the actuators to move the translator and gimbals at a constant rate. The simulated sensor voltage levels were gradually reduced in steps from about 2 V to 0.02 V, and the translator and gimbal displacements were recorded as the mechanisms moved back and forth over their complete range of travel. During these tests, an incorrectly phased electrical limit-stop circuit was discovered in one of the gimbal actuator's drive electronics, which prevented the actuator from being stepped off the stop once it had been engaged. This was easily remedied.

The results of the open-loop tests indicated a problem in the response of one translator actuator at low pulse rates, a similar but less severe problem with the other translator actuator, and a visible backlash characteristic in the gimbal actuator being used for the simulation. The translator actuator problem displayed itself as an intermittent failure to step, although it occurred with greater and greater frequency as the VCO pulse rate to the stepper-motor drive was reduced. In fact, for the actuator that translates the engine array assembly in a vertical direction, the effect was very pronounced, and in several instances the translator stopped completely for VCO pulse rates less than about 5 pulses (steps)/s. The actuator driving the translator assembly in a horizontal direction exhibited only a slight tendency to miss steps at very low stepping rates. Even though the engine array was counterweighted for vertical motion, the balancing was not exact, and the added load appears to make a significant difference.

A clue to the origin of the translator difficulty is the apparent lack of any history of such behavior during bench testing of the closed-loop electronics, when the actuators were, of course, not under mechanical load. In addition, the difficulties also were not apparent when the engine array was translated using an older set of actuator drive electronics (which can be used only for open-loop operation). The older drive electronics (a commercial design) have the characteristic of continuously powering the stepper motor windings as opposed to the

newer design (described in detail in Ref. 5), which pulses the windings for a relatively short, fixed period of time regardless of the pulse repetition rate. The objective in the new design is to save power, since the stepper-motor duty cycle will be quite low during normal TVCS operation. The new design also is free of "latch-up" states and uses higher reliability components.

It became clear then that initial sizing of the stepper-motor drive pulse period (12.5 ms for translator actuators, 10 ms for the gimbal actuators), while adequate for actuator stepping under no-load, was unacceptable for at least the translator actuators under load. Circuit modifications were made to widen the drive pulse supplied by the VCOs. Satisfactory operation was not achieved until the translator and gimbal actuator drive pulses were lengthened to 20 ms and 16 ms, respectively.

Some suspicion was also voiced by the actuator designers that gear wear or damage might have had much to do with the problem by increasing the frictional load. As a result of that theory the worst offending actuator was removed, found to be well worn with some broken gear teeth, and was replaced with an actuator in somewhat better condition. However, with the 12.5 ms pulse drive resubstituted, poor actuator response was again observed, substantially unchanged from the first test. Widening the pulse to 20 ms again cured the problem.

2. Closed-loop TVC responses. Figure 63 shows the recorded responses of several variables within the TVC (modified as discussed in Subsection C-1 and in Ref. 47) for a test run with initial translator and gimbal position offsets. In the case of the translator, the position offsets are analogous to and indistinguishable from center-of-mass misalignments in the X and Y direction. Initial values were: $y_T = 0.07$ ft, $x_T = -0.08$ ft, and $\alpha = 0.095$ rad.

Transient response of the X and Y axes, as controlled by the Y-translator and X-translator respectively, were nicely damped and therefore quite satisfactory. The "glitch" in $y_T(t)$ at about 310 s is as yet unexplained, although there is some suspicion that it was the result of a power transient to the ion-thruster recycle (trip). (Such power transients had been observed previously to couple enough energy to some TVC cables to momentarily send a short burst of pulses to one or more of the actuators.) Note also that the response magnitudes in the Y-axis were roughly 10 times greater than those in the X-axis. This was a consequence of dropping the Y-axis sensor gain by a factor of 10 to compensate for
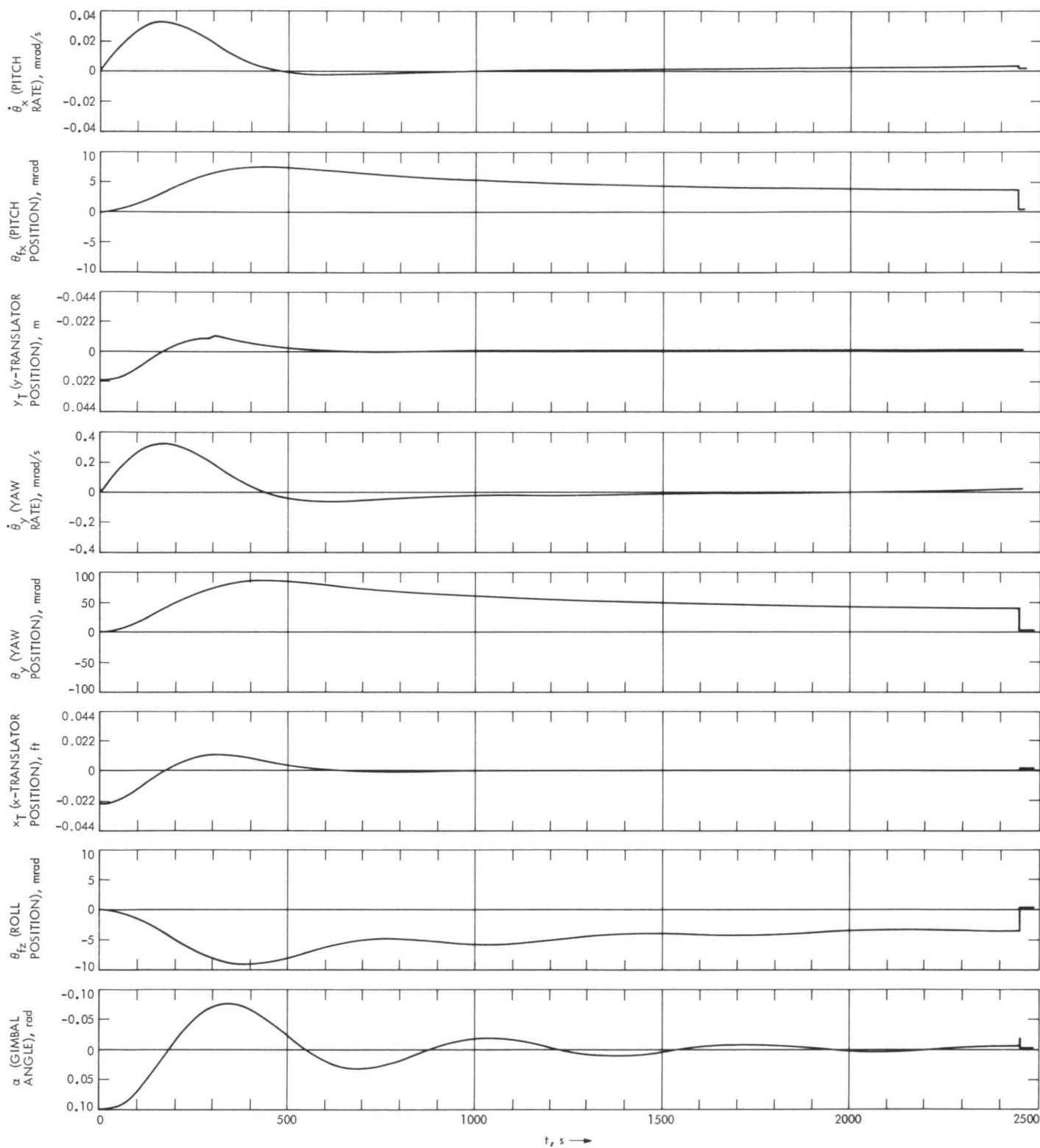
Fig. 63. TVC (modified) test response to initial translator and gimbal displacements

about 10 times less inertia in the Y-axis. VCO and compensation loop parameters were the same for both translator loops.

The gimbaled Z-axis response obviously was not well damped and therefore somewhat less than satisfactory in performance. Adjustment of the gain factors K_2 and K_F substantially improved the loop damping (Ref. 47).

As indicated previously, the gimbal drive pulse was widened even though it did not appear to be necessary. However, a somewhat different problem from that experienced with the translators was evident in the case of the gimbal performance. Recordings of gimbal angle displacements (Fig. 63) showed a definite flattening on the peaks and valleys of the response, characteristic of gear backlash or hysteresis. Substantial backlash in a gimbal actuator has also been observed in bench testing (Ref. 48). While the backlash did not significantly degrade the transient performance of the system, it can have very undesirable effects during limit cycle operation, i.e. increasing the limit cycle amplitude of spacecraft angular position error as well as actuator stepping frequency. A new gimbal actuator design, to be tested in the near future, promises to correct the backlash problem.

Figure 64 is another recording of the TVC response to initial translator and gimbal displacements, showing the pitch phase-plane transient. Of particular interest in this X-Y plot is the very evident effect of analog computer
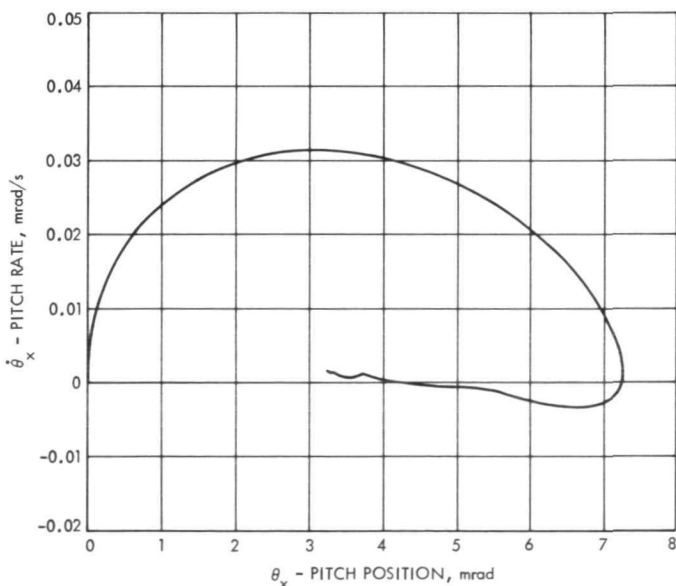
Fig. 64. Simulated spacecraft response to a disturbance (Ref. 47)

integrator drift during the test. When the phase-plane trajectory (which starts at $\dot{\theta}_x = 0$, $\theta_{fx} = 0$) first crosses the $\dot{\theta}_x = 0$ line at about $t = 470$ s, the requirement that the slope of the curve be infinite is very nearly met, although there is a slight positive bias (drift) in the rate. However, at the next apparent crossing ($t \cong 1500$ s), the proper rate/position relationships are obviously not present, an indication of significant levels of drift in both the rate and position integrators.

At the conclusion of the TVC transient test response to initial engine displacements ($t \cong 2500$ s), an "engine-out" condition was simulated by instantaneously setting $f_2 = 0$ (Subsection F-3). The TVC response to that action is shown in Fig. 65.

Engine gimbal angle and roll angular position remained reasonably quiescent during the engine-out transient, as they should, in spite of the 50% reduction in effective roll-control torque. Translator displacements (each is required to move 0.375 ft to put the resultant thrust vector through the vehicle c.m.) were well damped as predicted by the linear analysis. And response time of the translator loops was predictably slowed due to the smaller control forces and the accompanying lower loop gains. Total translator excursions during the transient were less than 0.6 ft out of a total available travel of 2.2 ft. Peak pitch-angle excursion of the vehicle during the transient was 2.3 deg.

As a check on the SEPST III TVCS test results, particularly those shown in Figs. 63, 64, and 65, the system equations were programmed for digital computer solution using CSSL III (Continuous System Simulation Language) on the Univac 1108. The vehicle dynamic characteristics were programmed exactly as they were for the analog computer. Control parameter values were, for the most part, taken at their nominal values (e.g., actuator gear ratios, sensor gains) except for a few compensation loop parameter changes of the order of 5% that were made to better reproduce actual test responses. Detailed comparisons, presented in Ref. 47, indicate good correlation between the digital and analog results.

D. 1500-h Test Results

1. **Test profile.** The summary of testing time accumulated on the TSS (two PC-thruster sets operating simultaneously) and on the PCs is shown in Fig. 66. The numbered arrows indicate system shutdowns and/or failures and are discussed in Subsection D-3. The PC accumulated time includes all tests performed in thermal vacuum.
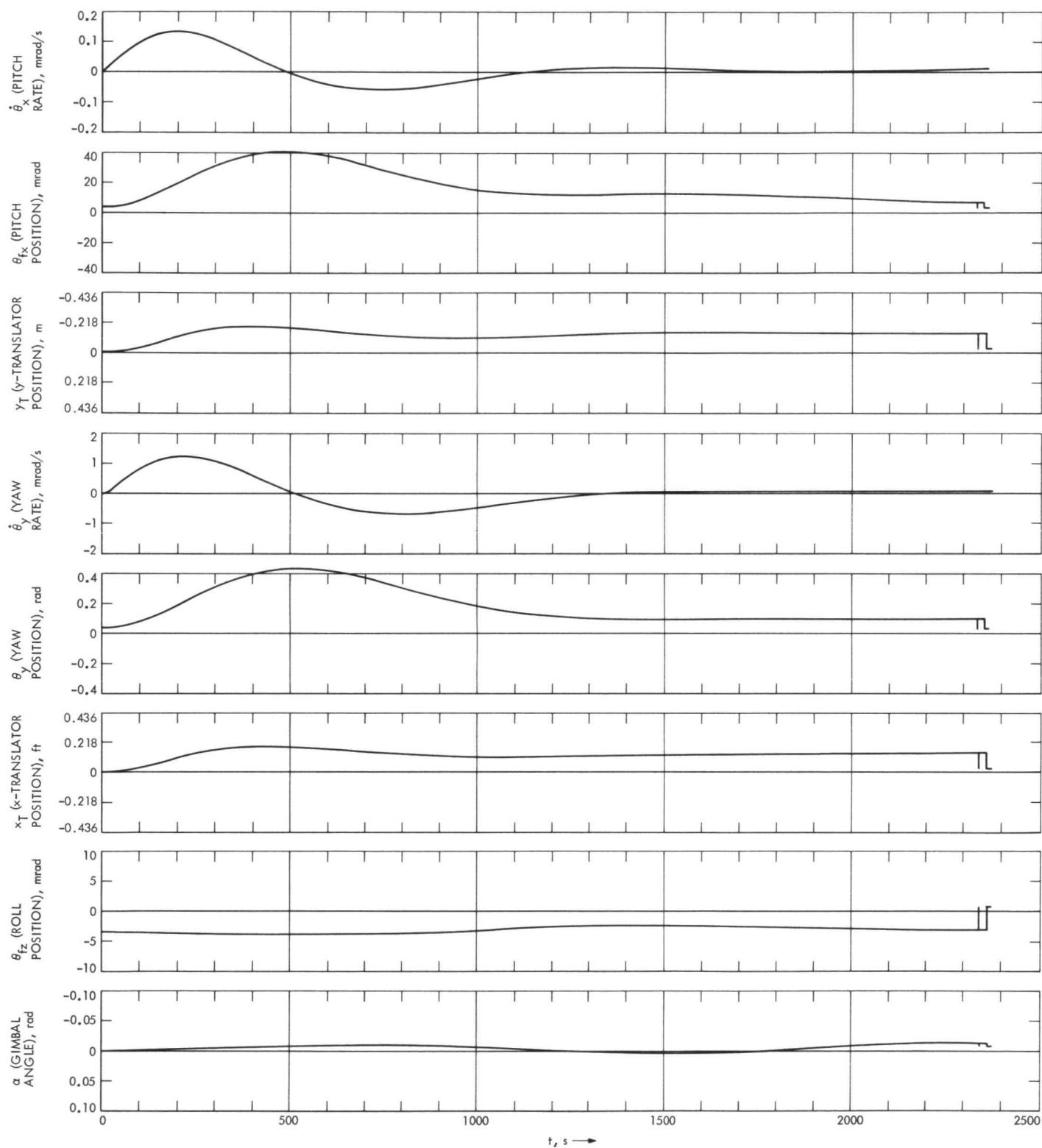
Fig. 65. TVC test response to engine-out ($f_z = 0$) transient condition
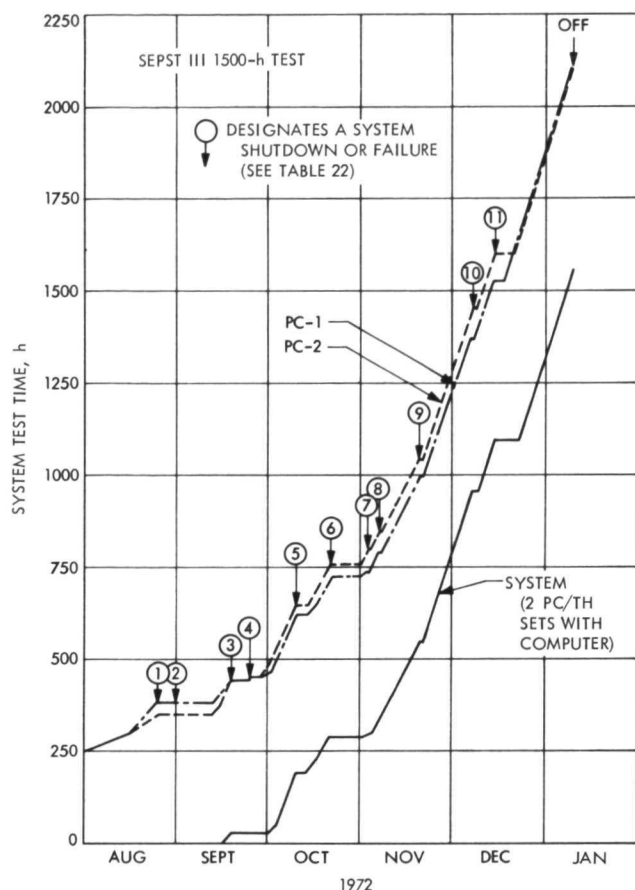
Fig. 66. SEPST III 1500-h test operating profile

Table 20. 1500-h test plan

Time period	Test
0 to 100 h	Establish system nominal operation
100 to 110 h	Check TVC functions
110 to 200 h	System operation with variable input voltage
200 to 300 h	PC-thruster switching
300 to 400 h	Power matching
400 to 1100 h	Check efficiencies
1100 to 1500 h	Accelerated flight profile
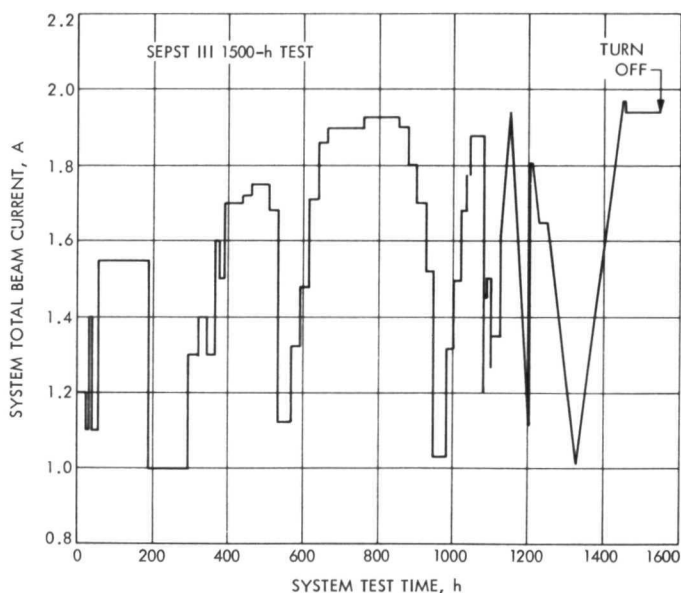
Fig. 67. SEPST III 1500-h test event occurrence

The test plan followed in performing the 1500-h test is shown in Table 20. The corresponding total ion-beam current history during the 1500-h test is presented in Fig. 67. During the first 1100 h of the test, the beam- and arc-current level changes were commanded through the teletype/computer manually. This approach was used to accomplish the tasks in Table 20 and to establish mass flowrates and propellant utilization efficiencies over long intervals (12 to 72 h) with constant conditions. The "flight profile" incrementing program incorporated into the CCSS computer was based on operating with a propellant utilization efficiency of about 95%. In the last 400 h, the computer increased and decreased the power level automatically using both 2- and 4-h intervals between increments. Both PC-thruster sets were changed simultaneously. Increment intervals as short as a minute or as long as desired were found to be acceptable.

At several times during the 1500 h, the PC input voltages were varied to demonstrate the PC regulation capabilities. Within the accuracy of the data system (±0.5%),

the PC efficiency, including input and output cabling losses, remained constant for input voltage variations over the full design range of 53 V to 80 V.

2. PC temperature distribution. Typical PC steady-state temperature distributions for five operating conditions are presented in Fig. 68. The operating conditions include thermal control heating with the PC turned off. Although thirty-six thermocouples were used, the data of Fig. 68 represent only a rough average of the detailed temperature distribution. Hotter areas, near transistors and magnetics, and colder areas, on the panel edges, are known to exist.

The data indicate that changes in module and panel heater placement might improve the temperature uniformity. The panel heaters should be distributed by area

	CONTROL MODULE	SCREEN (SCR) INVERTER (INV)	SCR INV	LOW-VOLTAGE MODULATOR	HIGH-VOLTAGE MODULATOR
	49 12 ● -10 32 -7 -2	47 -2 ● 3 25 10 22	● 20 47 -6 4 46 11 -3 25 7 ● 15 16 29	48 -2 ● 12 9 18 25	47 -1 ● 13 1 15 20
	STAGGERED-PHASE GENERATOR ● 29 58 54 4 10 ● -2 -7 33 4 -2 13 3	SCR INV 22 ● 51 48 5 0 9 4 ● 19 13 26 34 25	SCR INV 13 ● 51 48 2 -2 16 12 ● 25 21 17 40 38	5 kHz INV 6 ● 51 52 2 6 20 21 ● 24 26 10 29 33	ACCELERATOR INVERTER 51 4 50 20 6 ● 18 2 20 25
	CONNECTOR MODULE ● 30 57 15 48 -6 2 ● -2 -11 34 6 -6 -1	SCR INV 23 ● 51 47 5 0 10 6 ● 21 15 27 37 29	SCR INV 14 ● 50 11 47 19 -2 ● 26 10 36 20 18 34	ARC INV 7 ● 54 51 11 7 23 26 ● 28 33 11 34 39	ARC OUTPUT TRANSFORMER 3 ● 51 51 6 6 ● 16 19 4 20 25 29 24
	LINE REGULATOR ● 31 49 44 4 -1 35 13 9 ● 15 13 43 23 18 -2 36 3 ● 4 8	SCR INV 24 ● ON 43 COLD 4 WALL -2 ● =-148 4 28 13	SCR INV 15 ● 42 46 -8 -5 8 13 16 22 19 27 34 OPEN CIRCUIT ● 21	ARC RECTIFIER-FILTER 8 ● 53 47 10 2 17 19 ● 23 26 12 28 31	HIGH-VOLTAGE FILTER 45 -1 9 ● 14 5 19

Legend:

DATA SET	OPERATING CONDITIONS	POWER, W
1	LN₂ OFF, HEATERS ON	180
2	LN₂ ON, HEATERS ON	180
3	LN₂ ON, PC ON	1620 (INPUT)
4	LN₂ ON, PC ON	2120 (INPUT)
5	LN₂ ON, PC ON	2675 (INPUT)

ALL TEMPERATURES ARE °C

● INDICATES THERMOCOUPLE LOCATION

Fig. 68. PC steady-state temperature distributions

rather than by module. Relocation of the nondissipative modules, such as the control module, staggered-phase generator, and connector module, would provide m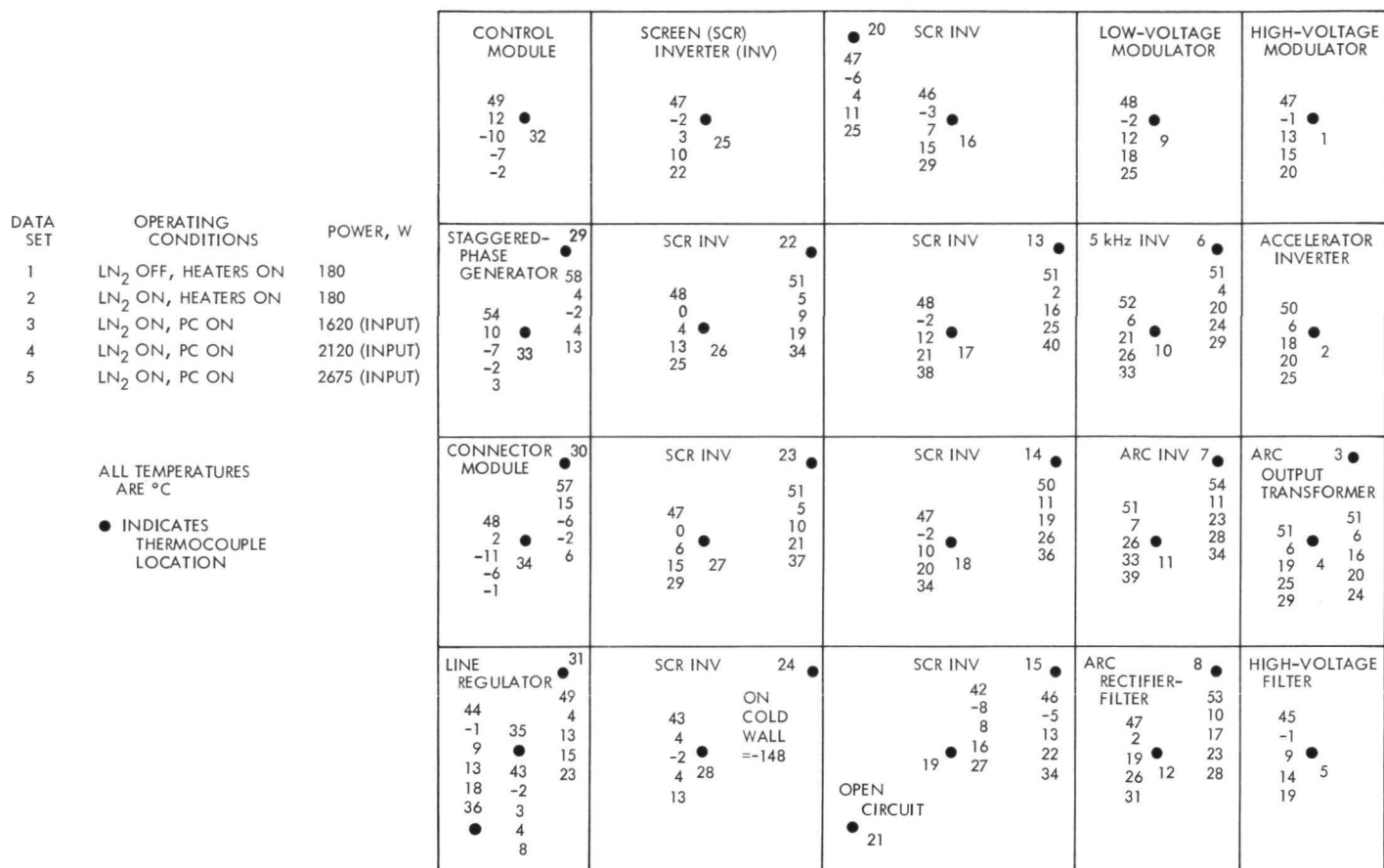ore efficient heat rejection. However, on the average, the radiating temperature at full power is close to the design value of 25°C. The arc inverter appears to be the hottest module and should be enlarged or moved to a cooler area of the panel.

3. **Failures.** The principal failures experienced in the SEPST III test program are grouped into "integration" and "1500-h test" categories. Failures during TSS integration were used to improve or eliminate element weaknesses prior to the 1500-h test. Failures during the 1500-h test were associated primarily with component problems (such as cathode life) or with problems not experienced during integration.

a. *Integration-failures.* The general types of failures that occurred in the final year of SEPST III integration are summarized in Table 21. With the exception of cathode failures, the "corrective action" indicated eliminated the problem for the duration of the testing. A few failures occurred due to assembly or wiring errors, but were not fundamental or design problems.

b. *1500-h test—shutdowns and failures.* As Fig. 66 shows, the 1500 h of TSS operation were accumulated over a period of about four months with eleven interruptions described in Table 22. The failures listed in Table 22, with the exception of No. 4 and possibly No. 6, were due to component failures. Only 4c can be considered a "system" failure. The PC-temperature controller is not considered to be part of the thrust subsystem (i.e., it is part of the vehicle thermal control subsystem).

In the case of failure 4c, the computer was apparently perturbed by a noise pulse during thruster arcing. An incorrect information bit was sent to the arc reference generator resulting in the high (7.5-V) dc reference command (the arc supply design maximum was 9.0 A, represented by a 5.0 Vdc reference signal). Subsequently, the

Table 21. Primary failures during SEPST III integration

No.	Type	Corrective action
1	Thruster hollow-cathode isolator internal arcing	Replaced original screen labyrinth disks with solid one-hole disks
2	Thruster connector pin to pin arcing	Replaced original single Deutsch connector with two connectors to separate high and low voltages
3	Cathode heater resistance changes	Continuing technology problem area
4	PC high-current fuse overheating	Potted fuses onto modules for heat sink
5	PC capacitor internal shorts due to high rms currents	Replaced capacitors with units having a higher current capability
6	PC arcing in vacuum due to interactions between the main and PC vacuum chambers	Isolated the PC chamber from the main chamber to eliminate ion-beam-induced pressure bursts
7	PC vacuum feed-through connector arcing (atmospheric side)	Relocated high-voltage pins within existing connectors

Table 22. Shutdowns and failures during 1500-h test

No.	Type	Corrective action
1	Reassemble computer program and debug	None
2	Power switch internal wire to case short due to poor assembly	Repaired wire
3	Thruster main vaporizer mercury leak	Replaced vaporizer
4a	Thruster 3 cathode heater failure	Replaced cathode
4b	Translator actuator (Y-axis) low torque after about 10^8 steps	Actuator main drive gear replaced because of wear by motor pinion
4c	Arc supply (PC-1) failed after high-arc-current reference command from the computer	Replaced arc inverter fuse, add Zener diode protection and modify computer program
5	"Flight" dummy load failed due to short screen supply upon command	Replaced relay drive transistor
6	PC-2 line regulator failed due to over-heating ($100°C$) by failed PC temperature controller	Replaced transistors and integrated circuits in line regulator. Repaired temperature controller
7	Same as failure No. 2 above	See No. 2 above
8	PC-2 screen inverter No. 6 failed, probably due to failure No. 6 above	Replaced fuse
9	Cathode heater on thruster 1 failed	Replaced cathodes in thrusters 1 and 3
10	JPL power failure	Restart vacuum systems and TSS test
11	Cathode heater on thruster 2 failed	Replace all cathodes

control program was modified to prevent this type of failure in the future.

The number of component failures was relatively small considering the breadboard nature of the system. Elements were not developed specifically for high reliability and screened electronic parts were not used. In addition, item No. 8 in Table 22 did not cause the PC to fail since the beam power can be supplied with six of the eight screen inverters operating.

4. Interactions. The scope of this section is limited to element-to-element interactions observed or measured for the first time in the SEPST III testing. "Interactions" related to the normal element-element operation (e.g., PC-thruster operating characteristics) are not included here.

a. PC-thruster-vacuum interaction. Initially, PC operation in vacuum was accompanied by failures, apparently due to corona or arcing on the PC panel. Aside from the fuse heat-sink problem (Table 21, item 4), all PC failures occurred only while operating a thruster and not with dummy loads. This fact was recognized only after noting that nearly all failures with thrusters had been preceded by 4- to 24-h runs at full power on dummy loads.

The final failure of this type occurred while the PC and main chamber pressures were monitored simultaneously. At this time, the PC chamber was pumped only by the main chamber through a large gate valve (Fig. 56). The thruster was observed to arc, causing a PC recycle. Both chamber pressures immediately increased, apparently due to the defocused ion-beam "washing" of the chamber walls. (The magnitude of the pressure rise is difficult to estimate because of the relatively slow response of the ion-gauge metering.) Immediately thereafter, the PC shut off due to a failure of the line regulator and 5-kHz inverter fuses.

In setting up the PC chamber initially, thruster-beam plasma-type interactions had been anticipated. The PC and main chambers were separated by an optically closed, LN_2 cooled, "chevron" baffle near the gate valve. In addition, a 100-mesh screen was placed across the PC side of the valve; however, these devices did not prevent ordinary gas pressure interactions.

After a separate diffusion pump system was installed on the PC chamber and the chambers were isolated, the only failures that occurred are noted in Table 22. No failures attributable to out-gassing, corona, or arcing were observed in the 1500-h test.

b. PC-thruster set-to-set interactions. The type of PC-thruster set-to-set interactions observed with the SEPST III setup is illustrated in Fig. 69. The figure shows the response of both PCs to a recycle (trip) on PC-1. The four channels per PC show the response of the beam-current main-vaporizer and the arc-voltage cathode-vaporizer control loops. This interaction is typical of a trip on either PC and is the most severe condition

Fig. 69. Power conditioner interactions

observed (i.e., about half of the trips caused no noticeable interaction).

Presently, this set-to-set interaction is being investigated. The probable sources are thruster ribbon-cable crosstalk and neutralizer/beam coupling. The perturbation of the nontripped PC is probably through the beam current. However, a perturbation of a few milliamperes in beam current would produce the observed reaction. The solution of this problem will require detailed cabling tests to isolate individual thruster harnesses passing across the TVC mechanism.

c. PC-thruster-computer interactions. The CCSS computer is required to monitor PC telemetry data for TSS control. Data signal returns are grounded at the computer input/output interface as well as on the PC signal return ring. However, during trips, the PC signal return can experience voltage spikes. Even though the telemetry signals are well grounded, these spikes apparently penetrated into the computer occasionally. It was observed that about a half or one percent of the trips would affect the computer operation by causing it to stop running or by sending an incorrect reference signal. After failure 4c, Table 22, the reference routine was redesigned to continually update the commanded references so that reference values could be in error for only a fraction of a second. A similar routine was programmed to automatically restart the computer if it were incorrectly told to stop. This nonstop routine was only partially successful. Other techniques for transient suppression such as buffering require investigation.

d. PC-solar array (simulator) interactions. When a high-voltage arc occurs in the thruster, the transistor-type PC is designed to supply a limited amount of energy into the arc and then shut off the beam and accelerator supplies for its own protection. To supply the energy before turning off, the internal PC turn-off signal is delayed a few milliseconds (i.e., "blanking time"). However, during the blanking time, the PC is transiently drawing a large overcurrent (50% to 100%) from the power source.

Investigation of methods for eliminating this input current transient began after the 1500-h test. Two basic approaches are being studied: (1) blanking time elimination, with burnoff energy delivered by beam-supply output capacitors, and (2) beam-supply current limiting. The first approach has been implemented to eliminate input overcurrents during a trip without input current overshoots during the turn-on after a trip. Capacitor energy of about 2.2 J is provided to duplicate the energy
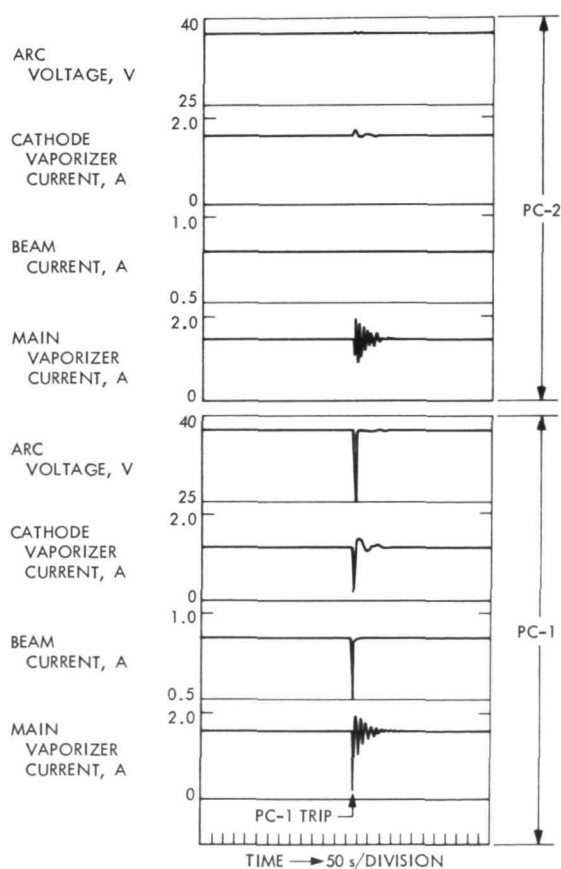
supplied originally with blanking (4000 V/A for about 550 μs). Circuit designs for the second approach are under way.

V. Conclusions

The completion of the 1500-h TSS functional demonstration test was the primary objective of the SEPST III program. However, in achieving this goal, substantially more than the basic functional demonstration was accomplished. The impact of each element on TSS integration, operation, and future development has been experienced. The primary conclusions drawn from this work are:

(1) Accurate and specific definition of interfaces is essential to a timely system integration program. In addition to normal operating requirements, this definition must include requirements for preflight checkout, self-protection at all interfaces, capability expansion, failure modes, maximum input power, interelement power losses, noise and transient sensitivity and production, packaging for vacuum, thermal control, electrical grounding, cabling, mounting, and handling.

(2) In any future design, each phase of the TSS operation (e.g., startup, throttling, and switching) must be considered in detail to anticipate and account for possible inflight variations in element characteristics and performance.

(3) Several problem areas require further investigation. These areas include electromagnetic interference (EMI), computer noise sensitivity, TVC noise sensitivity, PC input-power transients, and applicability of present spacecraft computers to TSS command and control requirements.

(4) This work provides a firm basis for building an engineering model TSS. No fundamental technical problems are apparent and the TSS efficiency and weight have been shown to fall within presently identified mission constraints.

References

1. Stearns, J. W., and Kerrisk, D. J., "Solar-Powered Electric Propulsion Systems —Engineering and Applications," Paper No. 66-576, presented at the AIAA Second Propulsion Joint Specialists Conference, Colorado Springs, Colo., June 1966.

2. Kerrisk, D. J., and Kaufman, H. R., "Electric Propulsion Systems for Primary Spacecraft Propulsion," Paper No. 67-424, presented at the AIAA Third Propulsion Joint Specialists Conference, Washington, D. C., July 1967.

3. Masek, T. D., and Pawlik, E. V., "Thrust System Technology for Solar Electric Propulsion," Paper No. 68-541, presented at the AIAA 4th Propulsion Joint Specialists Conference, Cleveland, Ohio, June 1968.

4. Kerrisk, D. J., and Bartz, D. R., "Primary Electric-Propulsion Systems Technology and Applications," *Astronaut. Aeronaut.*, Vol. 6, No. 6, June 1968.

5. Pawlik, E. V., et al., *Solar Electric Propulsion System Test*, TR 32-1480. Jet Propulsion Laboratory, Pasadena, Calif., August 1970.

6. Masek, T. D., and Macie, T. W., "Solar Electric Propulsion System Technology," Paper 70-1153, presented at the AIAA 8th Electric Propulsion Conference, Stanford, Calif., August 1970.

7. *Solar Electric Propulsion Asteroid Belt Mission Study*, Final Report on JPL Contract 952566, NAS 7-100, Document SD 70-21. North American Rockwell Corp., Downey, Calif., January 1970.

8. *Study of a Solar Electric Multi-Mission Spacecraft*, Final Report on JPL Contract 952394, NAS 7-100, Document 09451-6001-R0-02. TRW Inc., Redondo Beach, Calif., January 1970.

9. Bartz, D. R., and Horsewood, J. L., "Characteristics, Capabilities, and Costs of Solar-Electric Spacecraft for Planetary Missions," Paper No. 69-1103, presented at the AIAA Sixth Annual Meeting and Technical Display, Anaheim, Calif., October 1969.

10. Wrobel, J. R., and Kerrisk, D. J., "Early Exploration of the Asteroids Region by Solar Powered Electrically Propelled Spacecraft," Paper XA.4, Joint National Meeting of the AAS (15th Annual) and the ORS (35th National), Denver, Colo., June 1969.

11. Kerrisk, D. J., "Implications of Electric Propulsion Systems for Spacecraft Designs," paper presented at the ASME Space Technology and Heat Transfer Conference, Los Angeles, Calif., June 1970.

12. Kerrisk, D. J., and Masek, T. D., "Propulsion System Design for Solar Electric Spacecraft," in *Elektrische Antriebssysteme*, proceedings of the Berich uber das DGLR Symposium, held in Braunschweig, West Germany, June 22–23, 1971.

13. Masek, T. D., and Womack, J. R., "Experimental Studies with a Mercury Bombardment Ion Engine System," Paper No. 67-698, presented at the AIAA Electric Propulsion and Plasma Dynamics Conference, Colorado Springs, Colorado, September 1967. (Also TR 32-1280, Jet Propulsion Laboratory, Pasadena, Calif., July 15, 1968.)

References (contd)

14. Reader, P. D., and Kerslake, W. R., "Bombardment Thruster Investigations at the Lewis Research Center—1971," NASA TM X-67836, presented at the Sixth Symposium on Advanced Propulsion Concepts sponsored by the Air Force Office of Scientific Research, Niagara Falls, N. Y., May 1971.

15. Weigand, A. J., and Nakanishi, S., "A Survey of Kaufman Thruster Cathodes," NASA TM X-67918, presented at the Symposium on Ion Sources and Formation of Ion Beams, Upton, N. Y., October 1971.

16. Goldstein, R., and Pawlik, E. V., "Cathode Effects on Thrust Subsystem Performance Predictability," Paper 72-420, presented at the AIAA 9th Electric Propulsion Conference, Washington, D. C., April 1972.

17. Rawlin, V. K., and Kerslake, W. R., "Durability of the SERT II Hollow Cathode and Future Applications at Higher Emission Levels," Paper 69-304, presented at the AIAA Seventh Electric Propulsion Conference, March 1969.

18. Hyman, J., Bayless, J. R., Schnelker, D. E., and Ward, J. W., "Liquid Mercury Cathode Thruster Systems," Paper 70-646, presented at the AIAA Sixth Propulsion Joint Specialist Conference, June 1970.

19. Macie, T. W., and Masek, T. D., "Power Conditioner Evaluation-Circuit Problems and Cures SEPST III, BB-1," in *Supporting Research and Advanced Development*, Space Programs Summary 37-62, Vol. III, Jet Propulsion Laboratory, Pasadena, Calif., April 1970.

20. Latham, W. C., "Grid-Translation Beam Deflection Systems for 5-cm and 30-cm Diameter Kaufman Thrusters," Paper 72-485, presented at the AIAA 9th Electric Propulsion Conference, Washington, D.C., April 1972.

21. *Thrust Vectoring Systems for Mercury Ion Thrusters*, Final Report under NASA-LeRC Contract NAS 3-14058. Hughes Research Laboratories, Malibu, Calif.

22. Banks, B. A., and Bechtel, R. T., *1000-Hour Endurance Test of a Glass-Coated Accelerator Grid on a 15-cm-Diameter Kaufman Thruster*, NASA TN D-5891. National Aeronautics and Space Administration, Washington, D. C., July 1970.

23. King, H. G., and Poeschel, R. L., "A 30-cm-Diameter, Low-Specific Impulse, Hollow Cathode Mercury Thruster," Paper 70-1099, presented at the AIAA Eighth Electric Propulsion Conference, Stanford, Calif., August 1970.

24. Masek, T. D., "Evaluation of the SE-20C Thruster, Design," in *Supporting Research and Advanced Development*, Space Programs Summary 37-51, Vol. III, Jet Propulsion Laboratory, Pasadena, Calif., June 1968.

25. Pawlik, E. V., "Neutralization of a Movable Ion Thruster Exhaust Beam," in *Supporting Research and Advanced Development*, Space Programs Summary 37-58, Vol. III, Jet Propulsion Laboratory, Pasadena, Calif., August 1969.

26. Fitzgerald, D. J., "Parametric Study of Mercury Hollow Cathode Neutralizers," Paper 72-421, presented at the AIAA 9th Electric Propulsion Conference, Bethesda, Md., April 1972.

27. *Cesium Feed Systems Electrical Isolation*, Final Report on JPL Contract NAS 7-502. Electro-Optical Systems, Inc., Pasadena, Calif., March 1968.

References (contd)

28. Herron, B. G., "High-Voltage Solar Arrays with Integral Power Conditioning," Paper 70-1158, presented at the AIAA Eighth Electric Propulsion Conference, Stanford, Calif., August 1970.

29. Muldoon, W. J., Garth, D. R., and Benson, G. C., "Functional and Physical Design of a Flight Prototype Ion Engine Power Conditioner," Paper 70-AV/SPT-38, ASME Space Technology and Heat Transfer Conference, June 1970.

30. Cronin, D., Goldin, D., and Biess, J., "Power Conditioning Suitable for High-Performance Electric Spacecraft," Paper 69-240, presented at the AIAA Seventh Electric Propulsion Conference, Williamsburg, Va., March 1969.

31. Schwarz, F. C., "A Governing Electronic Mechanism for Ion Propulsion Engines," Paper 70-1157, presented at the AIAA Eighth Electric Propulsion Conference, Stanford, Calif., August 1970.

32. *Development and Test of an Ion Engine System Employing Modular Power Conditioning*, Final Report on JPL Contract 951144, NAS 7-100, Document SSD60374R. Hughes Aircraft Co., Malibu, Calif., September 1966.

33. Pawlik, E. G., Costogue, E. N., and Schaefer, W. C., "Operation of a Lightweight Power Conditioner with a Hollow Cathode Ion Thruster," Paper 70-648, AIAA Sixth Propulsion Joint Specialist Conference, San Diego, Calif., June 1970.

34. *Development and Test of a Flight Prototype Power Conditioner for 20-cm Mercury Bombardment Electric Thruster System*, Report on JPL Contract 952297, NAS 7-100. Hughes Aircraft Company, El Segundo, Calif., April 1971.

35. Masek, T. D., *Sizing a Solar Electric Thrust Subsystem*, Technical Report 32-1504, Jet Propulsion Laboratory, Pasadena, Calif., October 15, 1970.

36. Zerbel, D. W., and Decker, D. K., "AC Impedance of Silicon Solar Cells," IECEC Conference, Las Vegas, Nev., Sept. 1970.

37. Masek, T. D., et al., "Integration of a Breadboard Power Conditioner with a 20-cm Ion Thruster," *AIAA J. of Spacecraft and Rockets*, Vol. 9, No. 2, February 1972.

38. Womack, J. R., and Chen, J., "Structural Evaluations and Dynamic Testing of Solar Electric Propulsion Components," presented at the 9th Electric Propulsion Conference, Bethesda, Md., April 1972.

39. *Solar Electric Multimission Spacecraft*, Internal Report No. 72-442, Jet Propulsion Laboratory, Pasadena, Calif., July 30, 1971.

40. Powell, R. L., and Stetson, K. A., "Interferometric Vibration Analysis by Wavefront Reconstructions," *J. Opt, Soc. Am.*, Vol. 55, pp. 1593–1598, December 1965.

41. Chen, J. C., and Badin, R., "Holographic Interferometry Application to Shell Structures," in *Supporting Research and Advanced Development*, Space Programs Summary 37-64, Vol. III, Jet Propulsion Laboratory, Pasadena, Calif., August 1970.

References (contd)

42. Macie, T. W., *Solid State Switching for Solar Electric Propulsion,* Technical Memorandum 33-461. Jet Propulsion Laboratory, Pasadena, Calif., December 15, 1970.

43. Costogue, E. N., "Electric Propulsion Power Conditioning," in *Supporting Research and Advanced Development,* Space Programs Summary 37-61, Vol. III, Jet Propulsion Laboratory, Pasadena, Calif., February 1970.

44. *Common Solar-Electric Upper Stage for High-Energy Unmanned Missions,* Final Report on NASA Contract NAS-6040. TRW Systems Group, Redondo Beach, Calif., July 14, 1971.

45. Perkins, G. S., et al., "A Mechanism for Three-Axis Control of an Ion Thruster Array," Paper 70-1156, AIAA Eighth Electric Propulsion Conference, Stanford, Calif., August 1970.

46. *1975 Jupiter Flyby Mission using a Solar Electric Propulsion Spacecraft,* Internal Report ASD 760-18, Jet Propulsion Laboratory, Pasadena, Calif., March 1968.

47. Fleischer, G. E., "Results of Solar Electric TVC System Design, Hardware Development and Tests," Technical Report 32-1578, Jet Propulsion Laboratory, Pasadena, Calif., in process.

48. Crawford, W. E., "Solar Electric Propulsion System Technology Project Thrust Vector Control Electronics," in *Supporting Research and Advanced Development,* Space Programs Summary 37-64, Vol. III, Jet Propulsion Laboratory, Pasadena, Calif., August 1970.

49. Crawford, W. E., and Fleischer, G. E., "Solar Electric Spacecraft Thrust Vector Control Mechanization," in *Supporting Research and Advanced Development,* Space Programs Summary 37-62, Vol. III, Jet Propulsion Laboratory, Pasadena, Calif., April 1970.

50. Kopf, E. H., *A New Approach to Derived Rate,* Engineering Memorandum 344-317 (Internal Document), Jet Propulsion Laboratory, Pasadena, Calif., February 4, 1971.

51. Kerrisk, D. J., and Masek, T. D., "A Zero-Gravity Mercury Propellant Feed System," Paper 66-250, presented at the AIAA Fifth Electric Propulsion Specialist Conference, March 7-9, 1966.

52. Masek, T. D., and Womack, J. R., "Experimental Studies with a Mercury Bombardment Ion Engine System," Paper 67-698, presented at the AIAA Fifth Electric Propulsion and Plasmadynamics Conference, September 1967. (Also available as Technical Report 32-1280, Jet Propulsion Laboratory, Pasadena, Calif., July 15, 1968.)

53. Womack, J. R., "Design and Evaluation of Propellant Tankage for SEPST Program," in *Supporting Research and Advanced Development,* Space Programs Summary 37-58, Vol. III, Jet Propulsion Laboratory, Pasadena, Calif., August 1969.

References (contd)

54. Brown, W. F., Jr., and Shannon, J. L., Jr., "Fracture Mechanics Concepts Applied to Aerospace Structural Problems," NASA SP227, in *Proceedings of Aerospace Structure Materials Conference*, NASA-Lewis Research Center, Cleveland, Ohio, November 18–19, 1969.

55. Irwin, G. R., "Crack-Extension Force for a Part-Through Crack in a Plate," *J. Appl. Mech.*, Vol. 29, December 1962.

56. Campbell, J. E., *Current Methods of Fracture-Toughness Testing of High-Strength Alloys with Emphasis on Plane Strain*, DMIC Report 207. Defense Metals Information Center, Batelle Memorial Institute, Columbus, Ohio, August 31, 1964.

57. Hollowell, J. B., Dunleavy, J. G., and Boyd, W. K., *Liquid-Metal Embrittlement*, DMIC Technical Note. Defense Metal Information Center, Batelle Memorial Institute, Columbus, Ohio, April 9, 1965.

58. *Fracture Toughness Testing and Its Applications*, collection of preprints prepared for the Symposium on Fracture Toughness Testing and Its Applications by the American Society for Testing and Materials at the Annual Meeting in Chicago, Ill., June 21–24, 1964.

59. "The Hows and Whys of Metal Failures," in *Materials Protection*, summaries of papers presented at the Texas Chapter of the American Society of Metals 2nd Annual Failure Analysis Seminar, (November 9–10, 1965), pp. 43-47, January 1966.

60. Johnson, J. D., and Boyd, W. K., *Corrosion of Titanium*, DMIC Memorandum 218. Defense Metals Information Center, Battelle Memorial Institute, Columbus, Ohio, September 1966.

61. Brown, W. F., and Strawlwy, J. E., *Plane Strain Crack Toughness Testing of High Strength Metallic Materials*, ASTM Special Technical Publication No. 410. American Society for Testing and Materials, Philadelphia, Pa., 1967.

62. Brownfield, C. D., *The Stress Corrosion of Titanium in Nitrogen Tetroxide, Methyl Alcohol, and other Fluids*, Report SID 67-213. North American, Inc., Downey, Calif., March 1967.

63. Berry, W. E., "Corrosion and Compatibility," *DMIC Review*, Defense Metals Information Center, Batelle Memorial Institute, Columbus, Ohio, October 1967.

64. *Fracture: Volume 6*. Edited by H. Liebowitz, Academic Press Inc., New York, 1968.

65. Tiffany, C. F., Masters, J. N., and Bixler, W. D., *Flaw Growth of 6A1-4V Titanium in a Freon TF Environment*, NASA CR-99632. Boeing Corp., Seattle, Wash., April 1969.

66. Wilheim, D. P., *Fracture Mechanics Guidelines for Aircraft Structures Applications*, Report No. AFFDL TR-69-111. Prepared for AF Flight Dynamics Lab by Northrop Corp., Feb, 1970.

67. Tiffany, C. F., Masters, J. N., and Shoh, R. C., "Fracture Control of Metallic Pressure Vessels," NASA Space Vehicle Design Criteria (to be published).

References (contd)

68. Heer, et al., *Optiumum Pressure Vessel Design Based on Fracture Mechanics and Reliability Criteria*, Technical Memorandum 33-470. Jet Propulsion Laboratory, Pasadena, Calif., February 1, 1970.

69. Macie, T. W., and Doupe, H., "Automatic Control of an Electric Thrust Subsystem," Paper No. 72-506 presented at the AIAA 9th Electric Propulsion Conference, Bethesda, Md., April 1972.

70. Doupe, H., and Macie, T. W., "Master Controller for an Electric Thrust Subsystem," presented at the Fall Symposium of Digital Equipment Computer Users Society, San Francisco, Calif., November 11, 1971.

71. Masek, T. D., "Solar Electric Propulsion Breadboard Thrust Subsystem Test Results," presented at the 9th Electric Propulsion Conference, Bethesda, Md., April 17–19, 1972.